INVESTIGATION OF DIODE PUMPED ALKALI LASER ATMOSPHERIC TRANSMISSION USING TUNABLE DIODE LASER ABSORPTION SPECTROSCOPY

DISSERTATION

Christopher A. Rice, Civilian, USAF

AFIT-ENP-DS-12-D-07

DEPARTMENT OF THE AIR FORCE
AIR UNIVERSITY

AIR FORCE INSTITUTE OF TECHNOLOGY

Wright-Patterson Air Force Base, Ohio

INVESTIGATION OF DIODE PUMPED ALKALI LASER ATMOSPHERIC

TRANSMISSION USING TUNABLE DIODE LASER ABSORPTION

SPECTROSCOPY

DISSERTATION

Presented to the Faculty

Graduate School of Engineering and Management

Air Force Institute of Technology

Air University

Air Education and Training Command

in Partial Fulfillment of the Requirements for the

Degree of Doctor of Philosophy
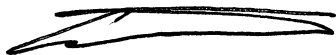

Christopher A. Rice, BS, MS

Civilian, USAF

September 2012

INVESTIGATION OF DIODE PUMPED ALKALI LASER ATMOSPHERIC

TRANSMISSION USING TUNABLE DIODE LASER ABSORPTION

SPECTROSCOPY

Christopher A. Rice, BS, MS
Civilian, USAF
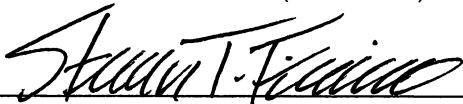
Approved:

_____
Glen P. Perram, PhD (Chairman)

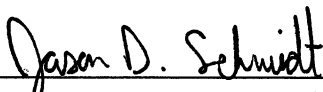_____
Steven Fiorino, PhD (Member)

_____
Jason D. Schmidt, PhD (Member)

_____
16 Nov 2012
Date

_____
19 Nov 12
Date

_____
20 Nov 12
Date

Accepted:

_____
M. U. Thomas
Dean, Graduate School of Engineering
and Management

_____
3 Dec 2012
Date

Abstract

A field deployable, tunable diode laser absorption spectroscopy (TDLAS) device fiber coupled to a pair of 12.5" Ritchey-Chretien telescopes was used to study atmospheric propagation for open path lengths of 100 m to 1,000 m to estimate atmospheric transmission at key High Energy Laser (HEL) wavelengths. The potassium (K) version of the Diode Pumped Alkali Laser (DPAL) operates in between two of the sharp oxygen rotational features in the ^{P}P and the ^{P}Q branches. Initial experiments were performed in the vicinity of molecular oxygen $X^3\Sigma_g^-$ to $b^1\Sigma_g^+$ electronic transition lines near the potassium emission line at 770 nm. More than 50 rotational lines in the molecular oxygen A-band $X^3\Sigma_g^-$ to $b^1\Sigma_g^+$ transition near 760 nm were observed. Temperatures were determined from the Boltzmann rotational distribution to within 1.3% (less than 2 K). Oxygen concentration was obtained from the integrated spectral area of the absorption features to within 1.6% (less than 0.04×10^{18} molecules / cm^3). Pressure was determined independently from the pressure-broadened Voigt lineshapes to within 10%.

The water vapor absorption lines close to the Cs DPAL emission near 895 nm were also investigated. Temperature, pressure, and water vapor concentration were determined for 150 m and 1 km open-paths with statistical errors of 0.2%. Comparison with meteorological instruments yields agreement for the 1 km path to within 0.6% for temperature, 3.7% for pressure and 2.4% for concentration.

A Fourier Transform Infrared (FTIR) spectrometer was also used to observe the absorption spectra at 1 cm^{-1} resolution. The TDLAS approach achieves a minimum observable absorbance of 0.2%, whereas the FTIR instrument is almost 20 times less sensitive. Applications include atmospheric characterization for HEL propagation

and validation of monocular passive raging.

The impact of atmospheric absorption of DPAL laser weapon performance was investigated using the Line-by-Line Radiative Transfer Model (LBLRTM) with the High Energy Laser End-to-End Simulation (HELEEOS). The TDLAS device was used to anchor simulations to outdoor atmospheric open-path collections. The implications of different laser gain cell configurations in DPAL systems are discussed, including spectral lineshape and atmospheric transmittance. The results are compared to existing HEL systems.

To my beloved

Acknowledgements

I give thanks to the Lord, who gives, sustains, and promises life to all things; to my wife who has been married to a man who has been going to school AND working for as long as we have been together; to my daughter, son, and new baby, I'm so glad your mother and I didn't wait until the degree was done to have you; to my brother who taught me how to ask the right questions, my mother who taught me how to ask nicely, and my father who taught me to take action when no an answer is given; to my advisor Dr. Perram who not once has turned me away when I needed council and gave me a chance when many others might not have; to my committee member Dr. Fiorino who gives tremendous enthusiasm and supports me in the riskiest of conquests; to my committee member Dr. Schmidt who reminds me of my engineering past and whose proofreading skills I covet; to Dr. Gross who is an invaluable faculty member and works very hard for all students under his care. To my friends, I don't see you, I miss you, and I would have gone off the deep end without our work lunches, MAN NIGHTs, MAN-LANs, and MAN-FIREs. Justin teaches me patience, Sam lends me joy, Tim gives me wisdom, Kevin shows me peace, Joel is altruistic, the Hand is always kind, Steve is ever faithful, and I strive to have Nat's wit. Thanks to Sue and Kelly for giving me my first real job and making me apply to the internship that led me to WPAFB, it was there Brett Hauber convinced me to work for the Air Force; to Marcia Hutcheson who gave me a shot at work; to Dr. Francis for helping my undergraduate degree get started and "Dr." Larimore who helped me finish it; to Greg Pitz for all our talks about science and life, for all the help he gave me, and for all I gained from helping him; to Jeremey Pitz, the only one who overnighted in the sub-zero weather to help me collect data and who is an asset to our institution; to Rick Bartell, who was always ready to hear about all my crazy plans; to Matt Krizo who was there when I finished my qualifier and has been left alone for too many workouts;

to Monte Anderson who taught me LaTeX and helped me with alkali simulations; to Kirk Brown who taught me you could finish a degree like this with many children; to Jeff Gallagher who keeps his lamp lit; to Tim Russel, man who exhibits excellence in optics; to Steve Massey who taught me how to run experiments in a lab; to all those who managed my contracts for all those years, Mark, Talyor, Amanda, Brittany, and Ashley - my family wouldn't have eaten without your work; to Emily for faithfully reading this document and helping me re-learn my first language; to Mike Ranft who was there when I saw my first diffraction pattern and helps me with all things supply and demand; to Greg Smith who was there when I coupled my first single mode fiber and submitted endless laser permits; to Kevin Pope, Jennifer Meier, and Jo Pollard who all put up with my IMPAC forms, DTS orders, sole-source letters, and safety documentation; and to those not mentioned here, had I included your name the acknowledgments would be longer than the remainder of this document.

"Though he slay me, I will hope in him..." -Job 13:15

Christopher A. Rice

Table of Contents

List of Figures

List of Tables

I. Introduction

High Energy Laser (HEL) systems for weapons applications have been investigated since the 1960's. For example, the 135 kilowatt Tri-Service Laser (TSL) and the Experimental Laser Device (XLD) were developed in the early 1970's. The megawatt class Navy-funded Mid-Infrared Advanced Chemical Laser (MIRACL) was operational by 1980. Most recently the Navy Laser Weapon System (LaWS) is designed to supplement and extend the Phalanx Close-In Weapons System (CIWS) operational range. [3]

The Airborne Laser (ABL) mounted a Chemical Oxygen-Iodine Laser (COIL) on a 747-400F, the Boeing YAL-1 (PrototYpe Attack Laser) to destroy ballistic missiles while in boost phase. The overall difficulty of the mission rivaled that of the task of putting man on the moon, with mission requirements that produced many technical challenges. The system successfully destroyed a liquid fuel boosting missile in early 2010. [1] Unfortunately the program was recently canceled. Attitudes of top-level officials towards the device were clearly summarized during a House Appropriations hearing on May 20th, 2010 where Robert Gates, then U.S. Secretary of Defense, said the following in answer to a question from Rep. Todd Tiahrt (R-Kan.):

> *"I don't know anybody at the Department of Defense, Mr. Tiahrt, who thinks that this program should, or would, ever be operationally deployed...The reality is that you would need a laser something like 20 to 30 times more powerful than the chemical laser in the plane right now to be able to get any distance from the launch site to fire...The ABL would have to orbit inside the borders of Iran in order to be able to try and use its laser to shoot down that missile in the boost phase...and if you were to operationalize this you would be looking at 10 to 20 747s, at a billion-and-a-half dollars apiece, and $100 million a year to operate."* [22]

Secretary Gates indicates several issues for why the program was cut. First, the ABL was originally designed to contain 14 gain modules and at the time only con-

tained six. Despite successful tests, the lower power output reduced the ABL effective range, making it less desirable. With a lower operational range, more units would be needed to fulfill mission requirements exacerbating the second issue, budget. If more devices are needed to complete the mission, initial costs to construct a larger fleet drive up the price, and also add to the yearly operational costs incurred thereafter. Even after great technological achievements, and overall program success, the ABL's funding was greatly reduced and renamed the Airborne Laser Test Bed (ALTB). The aircraft is stored at Davis-Monthan Air Force Base in Tucson and maintained by the 309th Aerospace Maintenance and Regeneration Group.

Atmospheric effects like molecular absorption and scattering, aerosol absorption and scattering, diffraction, atmospheric turbulence, and thermal blooming can all reduce the performance of a laser weapon system. For example, a hydrogen fluoride (HF) chemical laser operates near 2.7 μm - near deep atmospheric absorption lines. The deuterium fluoride (DF) chemical laser has an emission spectrum around 3.9 μm where an atmospheric transmission window exists. In space, over vacuum paths, an HF laser would suffice and would have superior diffraction limited performance compared to a DF laser system. However, as soon the mission included atmospheric slant paths, the HF laser becomes highly undesirable. All laser system parameters, and their respective affects on transmission, must be considered on a system-by-system and mission-by-mission basis, the focus of this work being the atmospheric transmission, particularly the molecular absorption component.

The Diode Pumped Alkali Laser (DPAL) attracted great interest from the HEL community since 2006 when Krupke patented the idea [44] of a three level laser system by pumping the D_2 ^{2}S$_{1/2}$ - ^{2}P$_{3/2}$ transition followed by collisional energy transfer to the spin-orbit split ^{2}P$_{1/2}$ state, and lasing on the D_1 ^{2}P$_{1/2}$ - ^{2}S$_{1/2}$ transition. By pumping the alkali laser gain cell with diode stacks, electrical sources can be used

as the laser source of power, removing the need for chemical safety and logistics chains. With a gas-phase gain medium, the overall beam quality of a DPAL has the opportunity to be excellent, and also gives the alternative of cycling the gas phase medium to manage thermal effects. [14] All three alkali variants, potassium (K), rubidium (Rb), and cesium (Cs), operate in the near-infrared regime. Good beam quality, attractive origin for power, appealing wavelength choices, options for thermal control, and excellent quantum efficiency make DPALs of great interest to the high energy laser community.

The atmospheric propagation characteristics of these emerging DPAL systems are largely unexplored. Modeling tools such as the HITRAN database, LBLRTM, and HELEEOS are available to predict line-by-line atmospheric transmission assuming the state of the atmosphere and aerosol content are specified. However, instruments capable of long path atmospheric transmission measurements for HEL applications are not available. In the presented work a field deployable Tunable Diode Laser Absorption Spectroscopy (TDLAS) apparatus has been designed, built, and tested. The system has been deployed to characterize atmospheric absorbance for potassium, rubidium, and cesium variants of the DPAL system. The input of atmospheric oxygen and water vapor on beam propagation has been investigated to benchmark atmospheric transmission and laser weapon performance models.

II.   Background

The study of atmospheric transmission is not a new one, and while laser spectroscopy could not exist before the invention of the laser by American physicist Theodore Maiman in 1960, [57] the study of spectroscopy began because of atmospheric absorbing species. The German optician Joseph Fraunhofer observed atmospheric absorption lines from a dispersed solar spectrum in 1814, now referred to as "Fraunhofer" lines, and he used the relative line spacings to compare different varieties of glass. He also extended Thomas Young's double slit experiemnt to many slits, leading to the diffraction grating, an optical element still in use today giving Fraunhofer the ability to measure wavelengths of spectral lines. Thirty-three years after Fraunhofer's discovery of spectral fingerprints, the German physicist Gustav Kirchhoff, whose topically broad work is still relevant to physicists and electrical engineers alike, made the connection between absorbing media and their unique spectra, noting differences in the dispersed spectra, and formed a relationship between the spectral fingerprint and the chemical being studied. In 1848 the French physicist Jean Bernard Lon Foucault observed the first laboratory-based absorption spectrum, a sodium flame absorbing yellow-orange light from a bright arc-lamp behind it. [91]

Tunable Diode Laser Absorption Spectroscopy

The study of atmospheric transmission can be achieved very effectively, not surprisingly, by using lasers as the interrogating source. Tunable Diode Laser Absorption Spectroscopy (TDLAS) relies on a narrowband tunable laser source that passes through the sample and is collected by a broadband detector. This is the opposite of conventional (and the original) method for absorption spectroscopy, where an incoherent broadband source passes through the sample and is collected with a spectrally

selective device, such as a spectrometer or interferometer. For spectrometers or interferometers, the spectral resolution is limited by the resolving power of the dispersive device used, the grating type of the spectrometer or the maximum path difference (MPD) of an interferometer. A tunable laser can investigate even beyond the Doppler limit with a relatively small physical setup, and compared to the other conventional systems listed above, has a very high spectral power density because tunable laser sources have all their emission power distributed over a small frequency band. Tunable laser sources are available from the ultraviolet (UV) to the infrared (IR) bands using a variety of pump sources, and there are many tunable lasers available that implement diodes as the pump source, adding further convenience and removing many of the problems associated with more cumbersome systems such as dye lasers. Thus, TDLAS devices have no need for large monochromators or long path interferometers at the detector, have a high spectral power density, and have a excellent detection sensitivity with spectral resolution as narrow as the laser emission lineshape. [20] Investigating atmospheric paths with TDLAS devices is ideally performed by interrogating the open-path to be investigated.

TDLAS Theory

TDLAS relies on Beer's Law, formally the Beer-Lambert-Bouger law, [58] which describes how light is absorbed in terms of the initial light I_0 entering a medium to the light that exits, I_1,

$$I_1(\tilde{\nu}) = I_0(\tilde{\nu}) \cdot e^{-\sigma(\tilde{\nu}) \cdot R \cdot N} \tag{1}$$

where I_0, in intensity or power, passes through absorber path length R at some wavenumber, $\tilde{\nu}$, with a frequency dependent absorber species cross-section, $\sigma(\tilde{\nu})$, and the state species number concentration, N. Species cross-section is related to the

degeneracies, g_1 and g_2 and the absorption lineshape, $g(\tilde{\nu})$,

$$\sigma_{12}(\tilde{\nu}) = \frac{g_2}{g_1} \frac{\lambda^2}{8\pi} A_{21} g(\tilde{\nu}) \tag{2}$$

The absorption cross-section and the number concentration can be combined to define the absorption coefficient, $\alpha(\tilde{\nu})$, [13] that yields another form of Beer's law,

$$I_1(\tilde{\nu}) = I_0(\tilde{\nu}) \cdot e^{-\alpha(\tilde{\nu}) \cdot R} \tag{3}$$

where the absorption coefficient, $\alpha(\tilde{\nu})$ is the product of the number concentration and the absorption cross-section. With the appropriate a priori knowledge, each of the different variables can be estimated for data collection. For example, if the absorption cross-section and concentration are known the path length can be calculated [38]; if the absorption cross-section and path length are known, the concentration can be estimated; and even estimates for cross-section can be made this way.

For atmospheric paths, absorbing species are broadened by approximately 760 Torr (1 atm) of pressure making spectral features much wider than commercially available tunable lasers. Using a pressure broadening rule of thumb of 3-10 MHz per Torr, [13] a sea level experiment at 760 Torr gives a pressure broadened lineshape of roughly 2.3 GHz, thousands of times larger than most commercially available tunable diode lasers with line widths 500 kHz or less.

The lineshape function, $g(\nu - \nu_0)$, is a convolution of the Lorentzian-shaped homogeneous pressure broadening and Gaussian-shaped inhomogeneous Doppler broadening effects. The Lorentzian-shaped pressure broadening [13] is represented by,

$$g_L(\tilde{\nu} - \tilde{\nu}_0) = \frac{\Delta\tilde{\nu}_L/(2\pi)}{(\Delta\tilde{\nu}_L/2)^2 + (\tilde{\nu} - \tilde{\nu}_0)^2} \tag{4}$$

where $\Delta\nu_L$ is the Full Width Half Maximum (FWHM) of the Lorentzian and values can be calculated from parameters in the HITRAN database on a line-by-line basis. [73] Using the HITRAN parameters γ_{air} and γ_{self}, the air-broadened and self-broadened half-widths, respectively, both at reference temperature 296 K, are corrected for the simulated temperature using n_{air}, the temperature-dependence correction factor, all used to find the pressure-broadened width,

$$\Delta\tilde{\nu}_L = 2 \cdot P_{atm} \left(\frac{296}{T}\right)^{n_{air}} \cdot [\gamma_{air} \cdot 0.8 + \gamma_{self} \cdot 0.2] \tag{5}$$

The Gaussian-shaped Doppler component can be represented as,

$$g_D(\tilde{\nu} - \tilde{\nu}_0) = \frac{2}{\Delta\tilde{\nu}_D} \sqrt{\frac{\ln(2)}{\pi}} \exp\left[-4\ln(2)\left(\frac{\tilde{\nu} - \tilde{\nu}_0}{\Delta\tilde{\nu}_D}\right)^2\right] \tag{6}$$

where the Doppler width can be calculated from species mass and temperature described in [13] as,

$$\Delta\nu_D = 2 \cdot v_0 \sqrt{\frac{2kT\ln(2)}{mc^2}} \tag{7}$$

and can be represented to give a wavenumber result as,

$$\Delta\tilde{\nu}_D = 7.2x10^{-7}\tilde{\nu}_0 \sqrt{\frac{T}{M}} \tag{8}$$

where T is in K, M is in atomic mass units, and $\tilde{\nu}_0$ is in cm^{-1}.

The Doppler broadening results from the Doppler shift caused by the velocity distribution of the absorbing (or emitting) atoms. This distribution gives the overall width of the Doppler broadening component. The convolution of a Lorentzian and Gaussian produce the Voigt distribution, the overall lineshapes seen in molecular absorption features at typical atmospheric pressures. Depending on the case, a Voigt distribution can be purely homogeneous or inhomogeneous. The higher the temper-

ature or the higher the pressure the species experiences, the wider the Doppler or Lorentzian components, giving a wider overall lineshape.

Use of Tunable Diode Lasers

Of the published articles describing applied TDLAS in the field, nearly all these make the use of White or Herriott cells with vacuums and pumps moving samples of the atmosphere into the cell for investigation. [43, 84, 83] Some specifically use White cells [10, 41, 90] while others specifically use Herriott cells [31, 32, 40, 49, 50, 85, 88, 89]. These absorption cells are small chambers filled with the gas sample under investigation with opposing mirrors where the tunable laser is propagated back and forth to give a long path length. Sometimes the absorption cell is simply a set distance with a retro reflector opposite the laser source. [104] After a measurement is complete, the cell is then evacuated and filled with the next sample. One of the primary advantages of absorption cells is that the pressure inside the cell can be lowered to reduce pressure broadening, thus making line shapes narrower and removing ambiguity for spectral features that may otherwise not be spectrally isolated. Absorption cells also offer advantages such as a known path length, known mirror losses, compact size, and temperature and pressure control. Again, these advantages do not represent atmospheric transmission of a HEL, and an experiment characterizing HEL atmospheric propagation using an absorption cell would not be complete.

The few published articles that demonstrate open-path TDLAS are concerned with very short path lengths, usually over a few meters. None of these are concerned with HEL propagation. For example, in [11] an open-path TDLAS system is used to monitor CO_2 around 1.58 μm (6329 cm^{-1}) and could scan nearly a 3 cm^{-1} bandwidth including at minimum two absorption lines with the laser diode at a single temperature. This paper used wavelength modulation spectroscopy (WMS) at 70 kHz along

with the absorption feature's second harmonic. The emission wavelength was controlled using a modulation of laser diode current. This is by far the most common form of TDLAS performed in recent papers and represents a significant shift from changing cavity length to control the output wavelength of a laser source. In reference [11] the laser power was split into three beams where one served as a power reference detector, a second was propagated through an absorption cell with a known concentration of the species being investigated for spectral calibration, and a third was propagated through the atmosphere and returned to a third detector for the absorption signal. This setup is typical of current open-path TDLAS systems. Another open-path TDLAS system described in [11] gives, at the time, the longest open-path of any TDLAS system with a path length of 88 m. Although the paper stated that SNR decreased with a longer path length, the authors did not state why. With longer path lengths, SNR should increase according to Beer's Law because there is more absorbing species in the cell, but here the reduced SNR could be due to effects from turbulence, lower power collected by the receiver because of beam spread, etc. The general system setup can be seen in [55] and is very similar to the open-path TDLAS system described above.

Another interesting paper concerning open-path TDLAS is [12] where the authors demonstrate a system that is very similar to the systems described above, but the application is for the detection of CO_2 over volcanically active areas through paths of nearly 100 m, although the authors claim that with the retroreflector used, a 500 m path is possible under certain atmospheric conditions. A 500 m path was not demonstrated. This paper uses an off-the-shelf system to monitor CO_2 absorption lines near 1.58 μm (6,329 cm^{-1}).

Another paper, [35] describes a hand-held, open-path TDLAS device that uses the signal reflected from background objects to find concentration. This device was

limited to an operating distance of roughly 20 meters depending on the reflectivity of the background. This device can be configured to detect hydrogen fluoride, hydrogen sulfide, or methane. Other related papers with the same authorship include [33] where standoff systems for trace gas detection are described, and a similar paper, [34] demonstrates a combination of the two papers above. The last paper gives more details about a finished handheld device for remote gas detection including ideas for oxygen sensors at 762 nm. Remote vehicle emission monitoring has been attributed to the individuals of the next interesting paper. [16] This group started remote emission monitoring in the late 1980s with the first remote-sensing instrument monitoring CO and CO_2 using broadband infrared spectroscopy and then moving on to NO by including UV sources. In [16] several narrowband open-path experiments concerning vehicle emissions are summarized, including experiments concerned with light and heavy duty trucks, locomotives, snowmobiles, and airplanes. These papers are usually concerned with CO and CO_2 found at their well known fundamental absorptions at 4.651 μm (2,150 cm^{-1}) and 4.255 μm (2,350 cm^{-1}) respectively. The articles reviewed with open-paths consist of 5-10 meter paths, usually orthogonal to the direction of travel so that the constituents from the vehicles are detected as the vehicle passes the testing site. This broadband spectroscopy suffers with a path-length limitation of 8 m and suffers from water interference around the hydrocarbon channel, but [16] does briefly mention an interesting problem for open-path devices. The paper refers to the failure of early open-path devices due to a "shimmering effect", most likely turbulence. This is a problem often ignored by most remote sensing and open-path TDLAS papers. In summary, of the papers referenced and searched, none consider HEL propagation, very few papers describe problems associated with turbulence - though some have symptoms that point toward turbulence - and none identify or describe solutions for turbulence or describe how to quantify turbulence parameters.

None of the open-path TDLAS devices demonstrate propagation over more than a few hundred meters.

Simulation Tools

For the studies outlined in this document, two tools were used extensively, the Line-By-Line Radiative Transfer Model (LBLRTM) and the High Energy Laser End-to-End Operational Simulation (HELEEOS). AFIT-specific codes were used to estimate alkali absorption, and therefore gain profiles.

LBLRTM

The Line-By-Line Radiative Transfer Model (LBLRTM) was originally derived from FASCODE. LBLRTM is developed and maintained by Atmospheric and Environmental Research, Inc. (AER). [19] Radiative transfer models are used to accurately predict atmospheric effects on the propagation of radiation from the ultraviolet to microwave region of the spectrum. LBLRTM examines extinction mechanisms like molecular scattering and absorption and aerosol scattering and absorption in order to characterize the ambient atmosphere and determine path transmission. LBLRTM is so heavily based in FASCODE that its inputs still use the legacy "TAPEx" formatting very similar to the input formatting originally used in FASCODE, a legacy format based on the magnetic tape inputs originally used for input. AER validates LBLRTM using atmospheric radiance spectra from the ultraviolet to the sub-millimeter. Inputs from the HITRAN database provide line parameters used by LBLRTM to carry out simulations for path optical depth and transmission. LBLRTM is used for calculation of infrared atmospheric radiance and its derivatives, used to compare data from sounding profiles, as the starting point for many retrieval algorithms, to calculate absorption coefficients for use in radiative transfer models in climate applications, to

train systems for Numerical Weather Prediction (NWP), and used as a comparison to satellite data. [19] In this work it is used to fit to spectral data collected by the TDLAS apparatus.

HELEEOS

The High Energy Laser End-to-End Operational Simulation (HELEEOS) was originally funded by High Energy Laser Joint Technology Office (HEL-JTO) and developed by Air Force Institute of Technology (AFIT). [29] Written in MATLAB® and distributed as an executable, the simulation models nearly every aspect of a HEL engagement scenario. Emerging technologies are generally supported, and a variety of different engagements can be simulated. Air-to-surface, surface-to-air, air-to-air, air-to-space, relay-to-relay, and side observations are supported in engagement geometries. Inputs are highly configurable, including a variety of laser types, geographic locations, C_n^2 profiles, aerosol properties, and probabilistic atmospheric parameters. At the time of this study, HELEEOS shares many calculation roots with the Scaling for High Energy Laser and Relay Engagement (SHaRE) toolbox, currently sponsored by Air Force Research Laboratory (AFRL) and developed by MZA Associates. Using SHaRE and internal calculations, HELEEOS considers atmospheric effects, diffraction effects, platform disturbances, thermal blooming, beam control, and turbulence effects on beam propagation using a beam-spread strehl ratio approach resulting in rapid calculation times. The Laser Environmental Effects Definition and Reference (LEEDR) [71] is used in HELEEOS to create vertical profiles for meteorological data and the associated environmental effects related to molecular and aerosol absorption like scattering, optical turbulence, and cloud free line of sight. This is is computed from databases and extrapolated for use in any global location. This engagement level simulation has inputs related to engagement geometry and atmospheric pa-

rameters, laser source and platform inputs, target lethality and platform inputs to allow HELEEOS to calculate output metrics related to the slant path like temperature, pressure, species and concentration, wind speed, and turbulence to compute final engagement metrics like molecular absorption and scattering, aerosol absorption and scattering, thermal blooming, beam strehl ratios, dwell time, and probability of kill. Ultimately HELEEOS development is centered around the goal of accurately predicting total energy on a target for a broad range of engagement scenarios. [29] HELEEOS and its internal components are currently maintained and upgraded by the AFIT Center for Directed Energy (CDE).

The DPAL systems have received considerable attention and systems having slope efficiencies exceeding 80% have been demonstrated [96], while others have shown exciplex assisted pumping schemes [63], and while most DPAL demonstrators use stable resonators, some have used transverse excitation with unstable resonators [102]. The larger spin-orbit splitting in cesium generally requires a molecular collision partner to accelerate the fine structure mixing, [100] but rare gases are also usually employed at pressures of 1-10 atmospheres to broaden the absorption profile and better match the diode laser spectral distribution for all DPAL variants. [60, 61] DPAL systems offer excellent thermal control, good beam quality, and can achieve quantum efficiencies of 95-99%. A high power, >1 kW, system with 48% optical-to-optical efficiency has also been reported. [14]

Scope of Research

This work sought to develop an open-path TDLAS system that operates at key HEL wavelengths, be easily configured to operate at different wavelengths in the field, and can collect data over long distances. The equipment was hardened to work in outdoor environments, including enclosing the laser system and support equipment,

installing hardware to reduce shock and vibration during deployment, and implementing methods for preventing damage during periods of inclement weather and transport. The complete device performance was characterized using molecular oxygen, a simple diatomic molecule that is both abundant and relevant to DPAL studies, in an indoor and an outdoor laser test range. Additional validation was achieved using alternative spectroscopic devices simultaneously, like a Fourier Transform Infrared (FTIR) spectrometer. Software has been written to control all hardware used during experiments, including the laser source, the modulator, the lock-in detectors, the wavemeter, the calibration laser, the data acquisition system, and any additional hardware that may be required.

Once a reliable device was constructed, collections of atmospheric data over DPAL emission wavelengths were attempted over open-paths. With successful data collections, the atmospheric constituents most important to DPAL atmospheric transmission was investigated, and temperature, pressure, and concentration of the associated atmospheric species was determined using spectroscopic methods and post-processing routines, all written from scratch. Results from open-path TDLAS collections were compared to the atmospheric transmission models for validation.

Simulations for DPAL gain cells were written, and used with an atmospheric transmission model to estimate DPAL atmospheric transmission as a function of DPAL gain cell pressure. Spectral absorption profiles were integrated into an end-to-end high energy laser simulation to draw conclusions about how DPAL gain cell configurations affect a variety of simulated operational scenarios.

Modeling of spectral gain of alkali cells in DPAL devices has previously been investigated for cesium. [5] Using the cesium code as a model, similar codes were developed for for potassium and rubidium. Each alkali transition is made up of several hyperfine lines, and each line is broadened by thermal and collisional effects. The

gain cell profiles from these do not incorporate asymmetry, which has been found experimentally. [52] These asymmetries could result in a DPAL laser emission profile that is wider than expected based on the simulations shown with extremely high gain cell pressures. When considering spectral DPAL emission, additional complexity is produced by the resonator used. Given that the resonator will likely narrow the spectral emission, the spectral absorption is used to estimate, and perhaps overestimate, the width of DPAL spectral gain.

III. A Tunable Diode Laser Absorption System for Long Path Atmospheric Transmission and High Energy Laser Applications

An open-path Tunable Diode Laser Absorption Spectroscopy (TDLAS) system composed of narrow band (300 kHz) diodes fiber coupled to a 12" Ritchey-Chretien transmit telescope has been developed to study atmospheric transmission of key High Energy Laser wavelengths. The ruggedized system has been field deployed and tested for propagation distances of greater than 1 km. Initial experiments were performed in the vicinity of molecular oxygen $X^3\Sigma_g^-$ to $b^1\Sigma_g^+$ electronic transition lines near 760 nm. The potassium version of the Diode Pumped Alkali Laser (DPAL) operates in between two of the sharp oxygen rotational features in the PP and the PQ branches. By scanning across many laser free spectral ranges and monitoring the laser frequency with a very precise wavemeter, the full structure of the oxygen molecular feature is observed. The device can also be used to observe rotational temperatures, oxygen concentrations, and total atmospheric pressure.

Introduction

Tunable Diode Laser Absorption Spectroscopy (TDLAS) is an active field of research with an international conference [2] and a very broad range of research areas including performance analysis [51], combustion [15], in-situ analysis [25], materials manufacturing [56], and much more. The background of TDLAS in field use is outlined well by Werle, [86] who has also authored a review article on post-processing of TDLAS data [87]. There is also a review article of tunable lasers with some example uses in the infrared region [93]. A majority of TDLAS articles are generally focused on using absorption cells, such as White or Herriot cells, to contain the sample gas with a folded optical path while also controlling parameters like temperature and

pressure. A small subsection of TDLAS research is concerned with open paths in place of absorption cells. For example, research areas include topics such as sensing greenhouse gas emissions from agricultural sites [68], sensing effluents from military cargo aircraft co-requisitely with other instruments [18], performing TDLAS experiments along the leading edge of an aircraft [30], over 5 and 15 m open paths with retro reflectors [81], and sensing NO_2 using a telescope over a 160 m path [75]. There is even an article that focuses on the use of TDLAS with O_2 [6]. In this chapter, a diode laser is used to perform multi-mode laser absorption spectroscopy (MUMAS) in the spectral region of molecular O_2 $X^3\Sigma_g^-$ to $b^1\Sigma_g^+$ electronic transition lines near 760 nm over a 10 m absorption cell. Temperatures over the range of 300 to 500 K were found with a precision of $\pm$ 2% are found, pressures varying from 200 to 760 torr with an experiment uncertainty of $\pm$ 2%, and concentration measurements that agree with estimated pressure using the ideal gas law and pressure sensors in the absorption cell. While the operation of MUMAS is slightly different from the technique described in this paper, many of the fundamental principles are the same. The device described here is an open-path TDLAS system that can be used to investigate the overall atmospheric transmission within the tunable area of the laser.

TDLAS Apparatus

Hardware

A complete system diagram illustrating optical and electrical paths is provided in Fig. 1. A New Focus Velocity model 6312 laser diode with a tunable range of approximately 759-770 nm was used as the source. This laser typically achieves an output power of 7 to 15 mW and has a spectral width of less than 300 kHz. This spectral width is small compared to the pressure-broadened widths of atmospheric absorption features. An Optics for Research IO-5 optical diode is placed in the beam
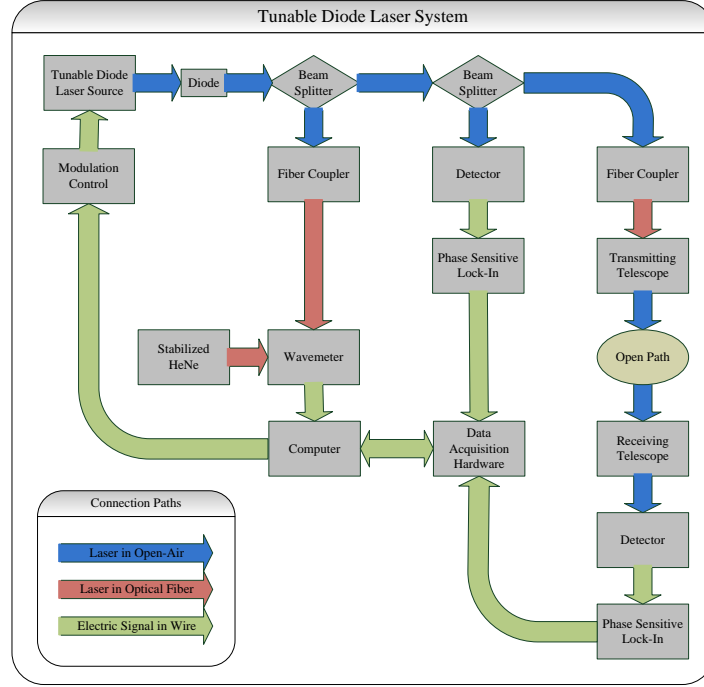
Figure 1. **Diagram of TDLAS system demonstrating overall layout.**

path to prevent back reflections from entering the laser cavity.

The source is split by Thor Labs PB108/PB145B1 2 m thick pellicle beamsplitters, first using a coated beamsplitter to a High Finesse WSU-2 wavemeter. The free spectral range that results from a very thin etalon, $\Delta\nu_{fsr} = c/(2nd)$, is on the order of tens to hundreds of GHz for typical pellicle thicknesses. This is wider than the tunable area under investigation, and is easily removed with the reference detector signal. The Fizeau-type wavemeter is fiber-coupled to fiber switch that is in turn coupled to the laser source and a SIOS SL-03 stabilized HeNe laser used for calibration to achieve $\pm$ 10 MHz ($\approx$ 0.00002 nm) accuracy in the spectral region being investigated. It should be noted that most TDLAS experiments use Fabry-Perot or similar devices for spectral calibration in post processing, and can offer a variety of free spectral ranges. Generally, Fabry-Perot etalons require calibration themselves.

The wavemeter requires little post processing of the wavenumber axis.

The remaining power of the source laser is then amplitude modulated by a Stanford Research Systems SR540 mechanical chopper at frequencies around 2 kHz and then coupled via a single mode fiber to a RC Optical Systems 12 military grade Ritchey-Chretien telescope. A Ritchey-Chretien telescope is similar in design to a Cassegrain telescope, but has hyperbolic mirror surfaces. Before expansion, another pellicle beamsplitter is used with a Thor Labs PDA 100A silicon detector/preamplifier as the laser power reference. The beam is expanded to nearly fill the primary mirror of the telescope. Fine focusing of the collimated laser can be achieved with movement of the secondary mirror of the telescope. The New Focus laser, now with 5 mW of power, is expanded to fill the telescope aperture and can be seen plainly by the naked eye hundreds of meters away. It should be noted that once the laser is expanded, the expanded beam falls well within eye-safe limits without viewing optics. Collimation is verified by direct viewing at the end of the path with a calibration target board and an infrared camera. The camera is moved across the center of the expanded beam and the expanded width is measured. Adjustments are made at the transmitting telescope until the expanded beam at target is nearly the same width at the exit aperture. A 6 inch mirror is placed some distance away from the telescopes and used to reflect a portion of the collimated light back to a receive telescope of the same make and model. A Thor Labs PDA 100A silicon detector/preamplifier is coupled to the receive telescope, and the receive telescope is carefully focused so that all received collimated light falls on the detector. To aid in alignment, an eye safe HeNe laser expanded to approximately 3 cm is attached to the transmission telescope is co-aligned with the expanded laser beam and used as a reference for the mirror alignment process to redirect the tunable laser back to the receive telescope. With experienced personnel and hardware in place, collimation and alignment of the system

takes about 10 minutes over typical paths.

The detector signals are analyzed by Stanford Research Systems SR-850 dual-phase lock-in amplifiers. The reference output of the chopper is used by the lock-in to automatically detect the chopper frequency and the phase of the chopped signal. The time constant of the lock-in is adjusted to be much shorter than the spectral scan speed of the laser, and the phase and gain of each lock-in are adjusted to give the best signal over the dynamic range expected. For the experiments shown, lock-in time constants were typically 100 ms with a filter drop off of about 6 dB/octave and a scan speed of about 0.003 nm/sec. An iris located at the entrance aperture of the reference detector is adjusted so that the relative signals reported by the lock-ins for the absorption signal, I, and the reference signal, I_0, are of similar magnitude. The dominant noise sources from (largest to smallest) during a collection are wind buffeting of telescopes and mirror, turbulence effects over the path being investigated, error in tunable laser frequency measurement, and response variations between detectors. The lock-in magnitude and phase along with laser control system output, and the chopper response are recorded by a computer using a National Instruments USB-6251 data acquisition device. This DAQ is also capable of synchronous analog and digital outputs, and can be used to drive other systems in the experiment from laser warning lights to laser wavelength. All hardware is secured in a frame with vibration shock mounts. The optical board is secured on the top for easy adjustments to optics in the field, as shown in Fig. 2.

Software

Instruments are controlled via MATLAB® with the Instrument Control Toolbox and a GPIB interface with an Agilent 82357A USB-to-GPIB converter. The National Instruments USB-6251 DAQ is controlled via MATLAB® with the Data Acquisition
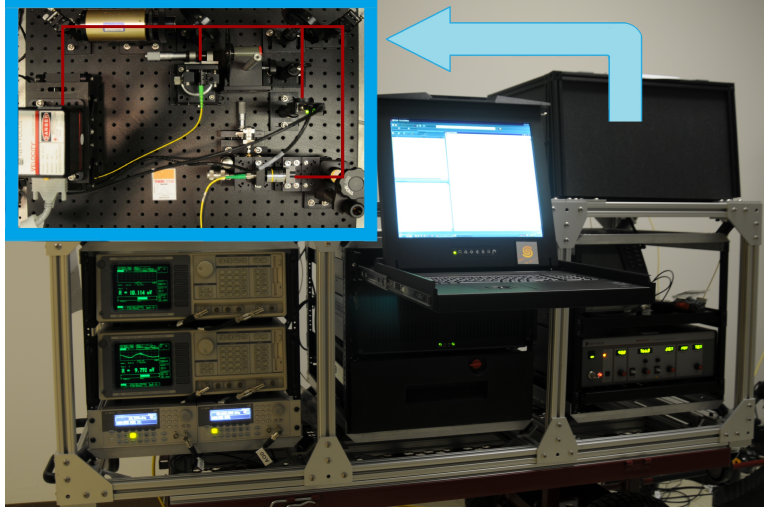
Figure 2. **Photo of TDLAS system with optical board.**

Toolbox through a USB interface. The NI USB-6251 DAQ also can produce analog
and digital control outputs, and drives the piezo in the New Focus laser cavity for
fine wavelength tuning. The laser power is monitored with a reference detector (I_0)
just before the open-path to be investigated. The precise wavemeter used in this
system is accessed through a custom MATLAB® interface using dynamically linked
libraries provided by the manufacturer. Tuning of the laser is achieved with a rough
motor adjustment via the GPIB interface and has a repeatable accuracy of about 0.1
nm. Fine tuning with a piezo flexing mechanism scans over a 0.2 nm window via
the digital to analog interface on the DAQ. The full spectrum is scanned by coarsely
tuning to a point in the spectrum, finely tuning through a 0.2 nm window, then
coarsely moving to the next region in the spectrum until the full tunable range of the
diode has been explored. The wavemeter is calibrated with a wavelength stabilized
SIOS SL-03 HeNe laser where calibration takes place before each scan. The output
of the wavemeter is collected in sync with the DAQ sampling of the lock-in outputs.
The wavemeter checks the course tuning of the laser so that spectral areas will not be
missed and optimizes scans to prevent too much spectral overlap. After each piezo

scan, the MATLAB® interface backs up data to the hard disk, and stores individual device statistics, all in an effort to diagnose potential problems discovered from post processing or in the event of power loss during an experiment. Uninterruptible power supplies are used prevent damage to equipment from unreliable power sources and prevent loss of data during collection.

Joining FSR scans

Because a full data collection is achieved using many overlapping finely tuned piezo scans, these scans must be joined together to form a full spectrum. Initially, the spectrum itself formed a complete spectrum using a crosscorrelation between adjoining scans in conjunction with known line positions of O_2 absorption features. Spectral absorption features gave a clear indication of how a set of piezo scans could fit together. However, nonlinearity in each piezo scan combined with spectral areas with no absorption features made the merging of piezo scans a difficult task to carry out accurately. Even when piezo scans were merged together, each piezo scans nonlinear spacing in wavenumber resulted in poor information about the lineshape of spectral features and the integrated area for each spectral feature. A piezo scan that was assumed to be linear in wavenumber could be in error by as much as half a wavenumber. A precise and quickly sampled wavemeter was used as the reference throughout each piezo scan. Typically the wavemeter sampled wavelength on the order of hundreds of Hz for a scan over many seconds. For each piezo scan, wavemeter output was used to find the spectral area where two scans overlapped with reliable laser output. An example of the overlapping spectral area of two adjacent piezo scans is shown in Fig. 3.

Here, the reliable overlap between spectral scans is nearly 0.5 cm^{-1}. The overall nonlinearly from sample to sample can also be seen in the gentle curvature of each
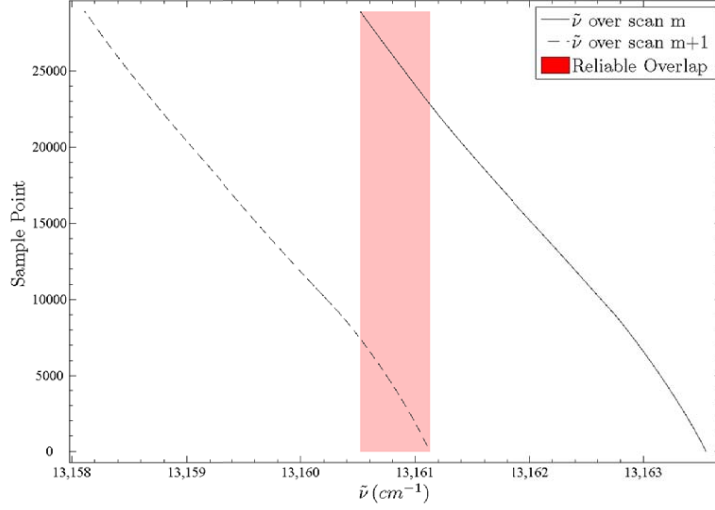
Figure 3. **Overlapping spectral region for two adjoining FSR piezo scans.**

scan, and the similar nonlinear structure is observed between different piezo scans. Once the reliable spectral overlap is determined, the best point that scans can be joined is determined by finding the overlapping point where the difference between raw signal data from each scan is the smallest. This reduces the chance for anomalous jumps in data and preserves the lineshape of spectral features caught between scans. The overlapping area of two scans can be seen in Fig. 4 with boundaries where the overlapping area is considered unreliable, and where the particular switch off point between adjacent scans lies. The residuals shown are the difference between the final signals of each scan over the reliable overlapping area.

This process is performed between each piezo scan to form the full spectrum. The resulting data has a nonlinear spacing between data points and is interpolated to form a linearly spaced spectral axis with the number of points required by the final application. Typically a full scan over 10 nm is generally over one million data points after piezo scans are stitched together. Once completed, the data set contains stitched data for wavenumber, voltage applied to the piezo, the rough output wavelength from
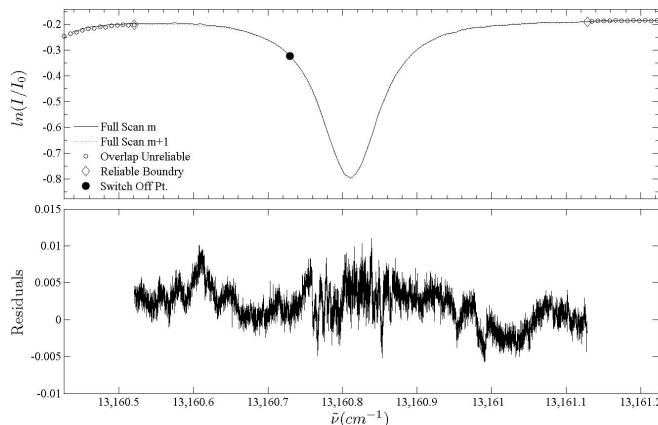
Figure 4. Demonstration of the choice for spectral area overlap of adjoining piezo scans.

the laser as a function of voltage, x and y outputs for each lock-in amplifier, and a synchronized absolute time-of-sample channel. In order to simulate the spectrum, have expectations about transmission, or fit to collected data, parameters about the molecule(s) of interest must be known. Generally, these parameters are contained in the HITRAN database in the forms of molecule, isotope, abundance, Einstein coefficient, broadening rate, temperature shift, and the like. In order to access these parameters in MATLAB® an interface was created to perform searches for atmospheric absorption lines over particular regions of the spectrum. This interface is similar to JavaHAWKS, but has its interface in MATLAB®.

Baseline considerations

The usable data from an experiment consists of the signal from the receive telescope detector (I) and the signal from the laser power reference detector (I_0) both referenced to the same linearly spaced wavenumber axis. This data has some baseline, a likely result of nonlinearity in detectors resulting from temperature changes over time of the detection and inherent in their manufactured nature (the preamplifiers of

24
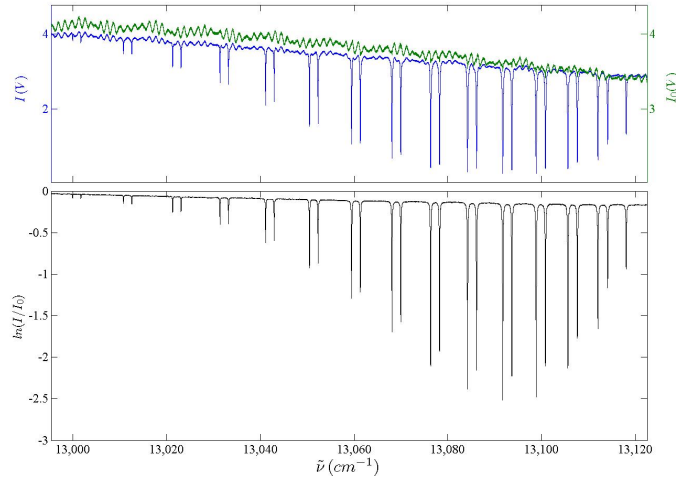
Figure 5. I, I_0, and $\ln(I/I_0)$ **with an instrument baseline visible over a 102 m path.**

PDA100As are especially sensitive to temperature). This baseline must be factored out before fitting to the data, or must be considered during fits. An example of the reference signal from each detector and the result of the using I and I_0 in concert is shown in Fig. 5.

Typically, the baseline is mostly linear, with some minor curvature if the environment where testing takes place stays at a relatively constant temperature. For the data shown above, fits to the baseline with a simple quadratic generally produce a squared term 4 orders of magnitude smaller than the slope term. For a higher order fit, a cubic term is 8 orders of magnitude smaller than the slope term with little change in the resulting standard error of the fit, thus demonstrating that there is little dependence on a cubic term for a baseline fit. Etelon effects from optics before the reference detector can also be seen, predominantly in green curve (I_0) but also visible in the blue (I), in Fig. 5, but are then removed when the two signals are used together. One critical point of discussion is that removing this baseline also removes effects from broadband aerosol scattering, an effect that can be significant depend-

25
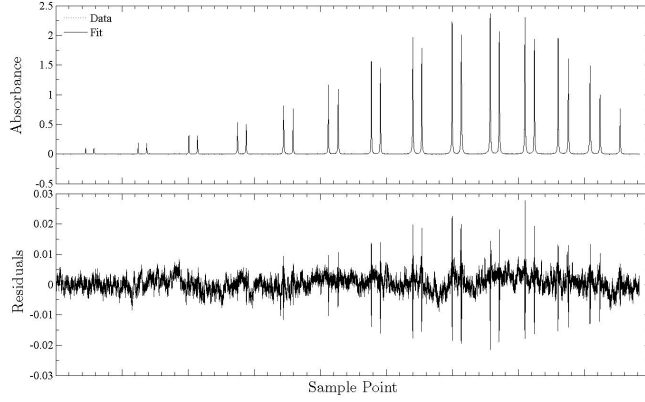
Figure 6. The $\ln(I/I_0)$ compared to a multiple profiles and fit residuals.

ing on the atmospheric aerosols present. The capability to retrieve this information cannot currently be obtained.

Spectral Lineshapes

Each isolated spectral line is fit with an individual Voigt lineshape, defining the line center, line amplitude (or spectral area of the line), the Doppler (Gaussian) temperature-broadened width, and the pressure-broadened (Lorentzian) width. All four parameters are allowed to vary during the fitting process. The least-squares fitting routine in PEAKFIT® was iterated until the fitting process converged to a solution giving the final result of the fit to the data is illustrated in Fig. 6 where each individual line is shown to be well isolated, and signal to noise is on the order of 200 for the larger absorption features.

The residuals have structure for each absorption feature although the residuals are very small and are typically less than 1% of the absorption feature. The least-squares fit to all lines shown resulted in an r² of 0.999 and a fit standard error of 0.0028. The structured residual shown in Fig. 7 is a close-up view of a single absorption feature from Fig. 6.
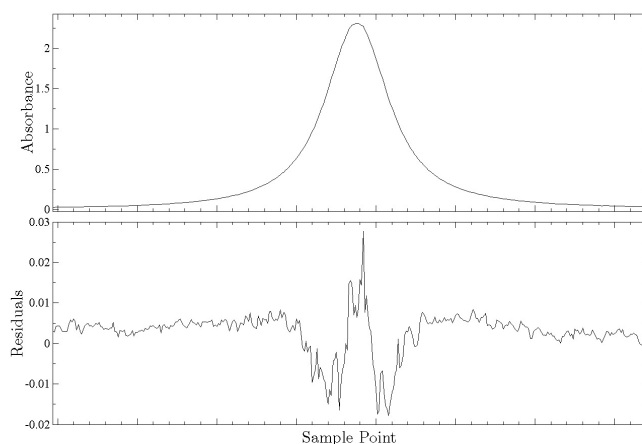
Figure 7. Example of structure in residuals.

The direct cause of this residual is unknown but has been observed in other literature [67]. Ritter experienced strikingly similar residuals in Voigt fits to oxygen A-band data. The W-shaped residuals Ritter demonstrates were experienced at several different pressures ranging from 76 torr to 600 torr and carry the same structure throughout pressure variations. It should be noted that these residuals have minimal effect on the quality of data obtained and speak more to the methods used for fitting and post processing. The residual depicted in Fig. 7 were a result of not finding the global minimum in PEAKFIT®. After extensive work, the structure in these residuals were eliminated using both PEAKFIT® and non-linear least squares methods in MATLAB®, the results of which are demonstrated in Chap. IV.

Conclusions

The TDLAS system is described in terms of hardware and software, and shown to collect information for molecular absorption over atmospheric paths from hundreds to potentially thousands of meters. Full spectra can be collected for the tunable range of the laser source used, and the laser source itself can easily be changed to produce

27

spectra over many different tunable ranges. Accuracy in wavenumber is limited to the spectral reference used and is approximately $\pm$ 10 MHz. Noise is primarily dominated from effects of telescope and mirror buffeting. Spectra from a 102 m path have been presented with signal to noise of over 200. The high-quality spectral scans from the system can be used for a variety of tasks, including investigation of multi-species molecular absorption, estimation of temperature, pressure, and concentration of atmospheric species with spectroscopic methods, high energy laser (HEL) atmospheric transmission, and validation of Monocular Passive Ranging (MPR) techniques.

IV. Investigation of atmospheric O_2 $X^3\Sigma_g^-$ to $b^1\Sigma_g^+$ using open-path tunable diode laser absorption spectroscopy

Applied A tunable diode laser absorption spectroscopy (TDLAS) device fiber coupled to a pair of 12.5" telescopes was used to study atmospheric propagation for open-path lengths of 100 to 1,000 meters. More than 50 rotational lines in the molecular oxygen A-band $X^3\Sigma_g^-$ to $b^1\Sigma_g^+$ transition near 760 nm were observed. Temperatures were determined from the Boltzmann rotational distribution to within 1.3% (less than 2 K). Oxygen concentration was obtained from the integrated spectral area of the absorption features to within 1.6% (less than $\pm$ 0.04 x 1018 molecules / cm3). Pressure was determined independently from the pressure-broadened Voigt lineshapes to within 10%. A Fourier Transform Interferometer (FTIR) was also used to observe the absorption spectra at 1 cm-1 resolution. The TDLAS approach achieves a minimum observable absorbance of 0.2%, whereas the FTIR instrument is almost 20 times less sensitive. Applications include atmospheric characterization for high energy laser propagation and validation of monocular passive ranging.

Introduction

Atmospheric transmission in the vicinity of the O_2 $X^3\Sigma_g^-$ to $b^1\Sigma_g^+$ absorption feature is important for remote sensing [25] and military applications [15]. Environmental applications often require the simultaneous monitoring of multiple atmospheric and pollutant concentration, which has stimulated the development of multiplexing and frequency modulation techniques. [51] In contrast, atmospheric propagation for high energy lasers requires high spectral resolution and low detection limits over long paths. The tunable diode laser absorption spectroscopy (TDLAS) technique is well developed and desirable for such applications. [86]

The majority of TDLAS experiments are performed in multi-path, White, or

Herriot cells where the temperature and pressure are readily controlled. A few applications for open-path instruments include monitoring greenhouse gas concentrations from agricultural sites with 10% uncertainties [69], sensing effluents from military cargo aircraft with path lengths of up to 15 m [18], determining atmospheric constituents onboard commercial aircraft [30], investigating methane and ethane over 5 and 15 m open paths [81], and sensing NO_2 with telescopic instruments over path lengths exceeding 160 m [75]. The challenges of developing TDLAS instruments for paths of 1 km or greater where jitter control, turbulence effects, and field operations become important, are largely unaddressed.

Recently Arita, et al. [7] examined the O_2 $X^3\Sigma_g^-$ to $b^1\Sigma_g^+$ transition using multimode laser absorption spectroscopy (MUMAS) for a 10 m absorption cell. Spectra were recorded at temperatures of 300-500 K, and pressures of 200-760 Torr. Fitting simulated spectra to the observations yields uncertainties in extracted temperatures of 8 K and pressures of less than 14 Torr. Concentration was reported with 2% confidence limits. [7] The current TDLAS results will be compared to this previous MUMAS work.

The oxygen $O_2 X^3\Sigma_g^-$ to $b^1\Sigma_g^+$ transition is of particular interest for passive ranging. Techniques estimating range using the depth of spectral absorption features when viewing a distant bright broadband spectral source is often referred to as monocular passive ranging (MPR). [53] The O_2 (X-b) transition is desirable for passive ranging for several reasons: 1) it has a reasonably constant atmospheric concentration ratio for dry air, 2) is characterized well as a function of altitude and meteorological conditions, and 3) is spectrally isolated from other absorbing species.

A demonstration of the MPR technique for a static rocket motor test using a Bomem MR-254 Fourier transform spectrometer at a range of 2.8 km yielded range estimates with an accuracy of about 0.5% (14 m). [39] More recently, an intensified

30
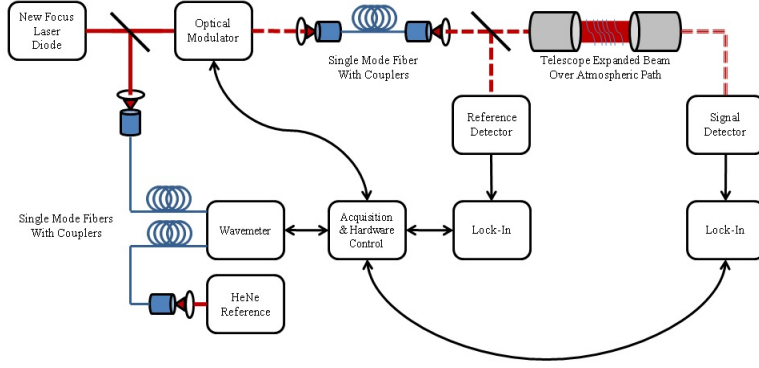
Figure 8. Diagram of the TDLAS of system.

CCD array coupled to variable band liquid crystal filter was deployed for a ground test of a static jet engine in afterburner at ranges of 0.35 - 4.8 km, establishing a range error of 15%. [4] The current work validates the MPR FTIR approach with the TDLAS active instrument. A second application for the TDLAS instrument involves characterizing molecular and aerosol, absorption, and scattering for high energy lasers. [57] In particular, the potassium variant of the Diode Pumped Alkali Laser (DPAL) operates near 770.1 nm, in the high rotational limit of the O_2 (X-b) ^PQ and ^PP branches. [105] Studying the atmospheric effects of high irradiance (kW/cm^2) laser propagation to distant targets will be greatly aided by the development of this rugged TDLAS instrument.

The TDLAS Device

The tunable diode laser absorption spectroscopy instrument is shown schematically in Fig. 8.

A detailed description of the device configuration and method for collecting spectra have previously been discussed. [66] The tunable diode is a New Focus Velocity laser model 6312 with a 100 mW maximum output, a 10 nm tunable range, and less than a 300 kHz linewidth. The laser source near 760 nm can easily be changed

to investigate other spectral regions of interest with minimal changes to the overall system. After amplitude modulation at a frequency of 2 kHz, the laser is fiber coupled and expanded to nearly fill a military grade 12.5 inch RC Optical RitcheyChretien transmit telescope. The laser beam is directed across an open-path and then received by a second identical telescope. Two Thor Labs PDA100As are used for the reference and signal detectors and are analyzed by Stanford Research Systems SR850 dual-phase lock-ins and recorded by a National Instruments USB-6251. Pellicle beam splitters are used to minimize etalon effects. The reference intensity is measured late in the optical train (immediately prior to the telescope beam expansion) and attenuated to balance sent and received signals. A High Finesse WSU-2 wavemeter is used to determine the frequency axis and is calibrated with a fiber-coupled SIOS SL-03 frequency-stabilized HeNe laser to achieve at better than 10 MHz accuracy. All hardware is connected to and controlled by a PC using MATLAB®. During an experiment, the laser is finely tuned by driving a piezo to tune over an approximately 0.1 nm range, and then coarsely tuned to the next spectral region. The process is repeated for 95 free spectral ranges to cover a 10 nm spectral region. Calibration of the frequency axis, baseline removal, and further spectral processing have recently been reported. [66]

System noise is generally dominated by telescope jitter and atmospheric turbulence over the path, although for paths of 100 meters, these effects are usually small. Spectra have been recorded over 100 m to 1 km open-paths, and the maximum open-path distance is expected to be approximately 5 km, a limitation of the tip and tilt pointing accuracy of the QuickSet QPT-130 ruggedized pan and tilt mounts used. Collection geometries consist of the transmit and receive telescopes next to each other separated by 1 meter, each viewing a 6 inch mirror placed at a variety of distances giving total path lengths from 100-1,000 meters. 1 km collections took place outdoors

after several inches of snowfall with an average temperature of -8 C, a 48% relative humidity, and a pressure of 989 hPa during the collection time.

The performance of the active TDLAS system was compared to a passive Fourier Transform Spectrometer. An ABB Bomem MR-304 FTIR spectrometer coupled to a reflective telescope with a 4.9 mrad field of view and 12 inch aperture was placed in between the TDLAS transmit and receive telescopes and viewed a 700 Watt halogen broadband source placed above the FTIR viewed through the same mirror described above. The path viewed by the TDLAS and FTIR are nearly the same. This FTIR uses a silicon (Si) detector with a spectral range of 8,000-15,000 cm^{-1} and an indium gallium arsenide (InGaAs) detector with a spectral range of 6,000-12,000 cm^{-1} and spectral resolution of 1 cm^{-1}. The Si detector provided superior signal-to-noise in the 760 nm spectral region. The FTIR device collected interferograms at 10 Hz resulting in spectra with 1 cm^{-1} resolution. Calibration and post processing techniques have previously been described. [39]

Two NIST-certified Davis Vantage Pro2 weather sensors were placed near the telescope and mirror. Temperature, pressure, and relative humidity measurements were recorded with instrument variations of 1 C, 2 hPa, and 6% respectively.

Results

A typical TDLAS spectrum in the vicinity of the molecular oxygen $O_2 X^3\Sigma_g^-$ to $b^1\Sigma_g^+$ (v'=0, v"=0) band is shown in Fig. 9a with approximately 95 free spectral ranges and over a million data points in the full collected spectrum with only every 25th data point plotted in the figure.

The rotational spectrum of the O_2 (X-b) absorption is assigned as $^{\Delta K}\Delta J(K'')$ where K is the total angular momentum without electron spin, and J represents the total angular momentum (spin + rotation). Fig. 10 shows the energy levels involved
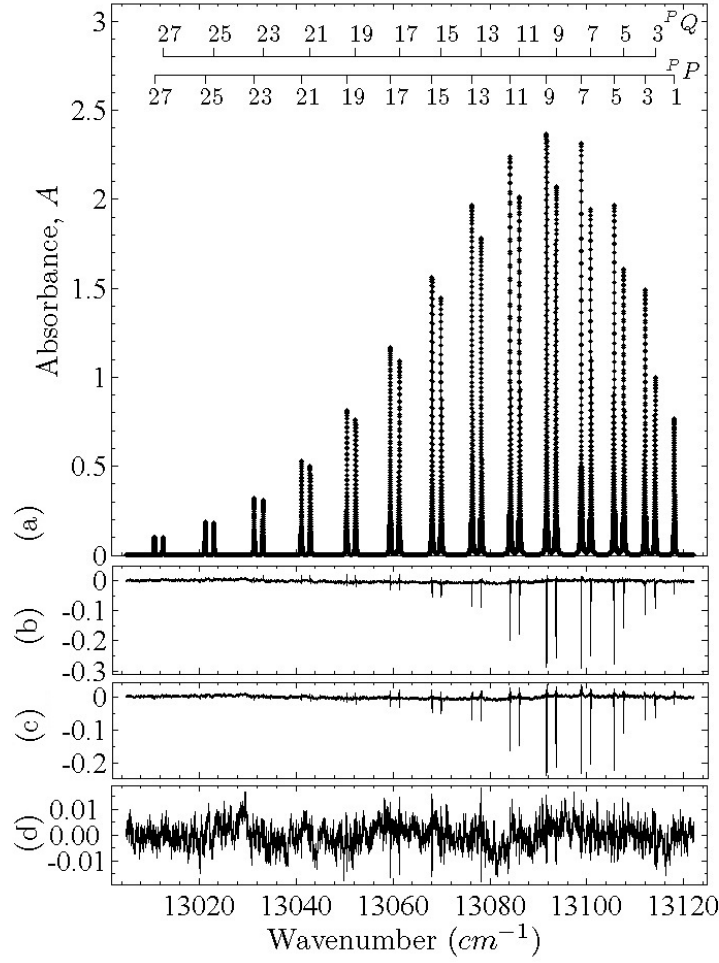
Figure 9. (a) Undersampled TDLAS spectrum of O_2 (X-b) (0,0) band with rotational assignments, (b) fit of Equation (9) using a series of Voigt lineshapes, (c) differences between observed spectra and simulation using weather instrument data, and (d) difference between simulation and data using TDLAS derived atmospheric parameters.
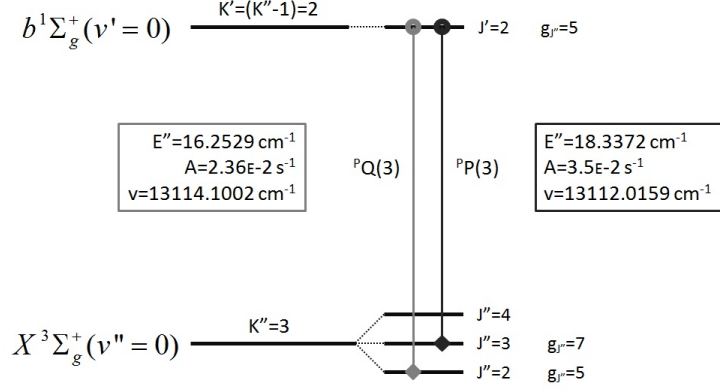
Figure 10. Example energy level diagram of O$_2$ (X-b) for the $^P P(3)$ and $^P Q(3)$ lines.

for the $^P P(3)$ and $^P Q(3)$ transitions.

The spectrum of Fig. 9 exhibits two of the four rotational branches, $^{\Delta K}\Delta J =^P P,^P Q,^R R,^R Q$, described by Hund's case (b) coupling for the magnetic dipole transition. [8] The R-branch lines up to $K'' = 27$ are observable with the current apparatus. However, the current analysis is limited to the P-branch where the rotational spacing is larger. Only the odd values of K are present due to nuclear spin statistics. The rotational distribution in the ground state peaks at $K'' = 9$, consistent with a temperature near 300 K. The long path length of 100 m and lack of instrumental broadening leads to a large peak absorbance of $A = 2.36 \pm 0.002$, despite the long radiative lifetime of ≈ 11.4 seconds. [73] The spectral resolution is limited by the pressure broadened lineshapes and complete spectral isolation is achieved.

The absorbance, A, for each rotational feature is described by the Beer-Lambert law:

$$A_{\Delta K,\Delta J,K''}(v) = -\ln\left(\frac{I_t(v)}{I_0(v)}\right) = \sigma_{\Delta K,\Delta J,K''}(v)N(K'',J'')L \tag{9}$$

where the natural logarithm of the send, I_0, and received, I_t, signals is equal to the product of the frequency dependent absorption cross-section of the specific rational

feature, $\sigma_{\Delta K, \Delta J, K''}$, the number density of molecular oxygen in the specific rotational level, $N(K'', J'')$ and the optical path length, L. I_0 and I_t are initially balanced using an iris on the I_0 detector to allow similar gain settings between both detectors and their respective lock-ins. The absorption cross-sections are specified as,

$$\sigma_{\Delta K, \Delta J, K''}(v) = \frac{g_{J'}}{g_{J''}} \frac{\mathbf{A}_{\Delta K, \Delta J, K''} \lambda_{\Delta K, \Delta J, K''}^2 g_V(v - v_0(\Delta K, \Delta J, K''), \Delta v_L, \Delta v_D)}{8\pi} \quad (10)$$

where the degeneracies for the ground and exited states are, $g_{J''} = (2J''+1)$ and $g_{J'} = (2J'+1)$, and $\Delta \nu_L$ and $\Delta \nu_D$ are the Lorentzian and Doppler linewidths (FWHM),

$$\begin{aligned}
\Delta v_L &= \left(\tfrac{296}{T}\right)^n \left(\gamma_{air}(p - p_s) + \gamma_{self} p_s\right) \\
\Delta v_D &\approx 7.2\text{x}10^{-7} v_0(\Delta K, \Delta J, K'') \sqrt{\tfrac{T}{M}}
\end{aligned} \quad (11)$$

where γ_{air} and γ_{self} are the air and self-broadening coefficients, p and p_s are the total pressure and partial pressure, and n is the coefficient of temperature dependence on the air-broadened linewidth, all defined by the 2008 HITRAN database. [73] M is the species mass in AMU; T is the temperature of the atmosphere in Kelvin. The state specific spontaneous emission coefficients, $\mathbf{A}_{\Delta K, \Delta J, K''}$, and line positions $\nu_0(\Delta K, \Delta J, K'')$ are also referenced from HITRAN. The Voigt lineshape g_V is area normalized so that the frequency integrated absorption is,

$$\sigma_{\Delta K, \Delta J, K''}^0 = \int_0^\infty \sigma_{\Delta K, \Delta J, K''}(\nu) d\nu = \frac{g_{J'}}{g_{J''}} \frac{\mathbf{A}_{\Delta K, \Delta J, K''} \lambda_{\Delta K, \Delta J, K''}^2}{8\pi} \quad (12)$$

The Boltzmann distribution specifies the rotational dependent number density,

$$N(K'', J'') = \frac{(2J+1)Nf}{Q(T)} e^{\frac{-E_{K'', J''}}{kT}} \quad (13)$$

where N is the total concentration of oxygen, $Q(T)$ is the HITRAN rotational parti-
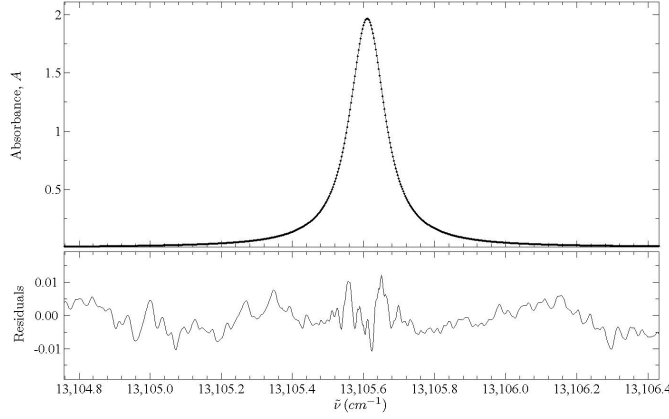
Figure 11. A fit of Equation (9) to the $^P P(5)$ rotational line.

tion function that is approximately equal to hcB/kT using rotational constant B, f is the isotopic abundance of $^{16}O_2$, and $E_{k'',J''}$ is the rotational energy for the ground state.

Fig. 9a shows a fit of Eq. (9) to each line in the observed spectrum. All lines in the spectra were fit simultaneously with Voigt lineshapes using a nonlinear least squares method. Each absorption feature was described using four parameters: line center, ν_0, integrated absorbance, $A^0 = \int A(\nu)d\nu$, Doppler width, $\Delta\nu_D$, and the Lorentzian width, $\Delta\nu_L$. Additionally, a small baseline ($A \approx 0.0019$) was observed and a cubic background was included. The RMS fit residual, 0.0022, is less than 0.1% of the peak absorbance, as shown in Fig. 9b. This detection limit is comparable to that achieved for controlled environment multi-path cells without multiplexed detection. The fit residuals are unstructured and the spectra exhibit a signal-to-noise ratio of about 150. Fig. 11 demonstrates a Voigt fit to a single line, the $^P P(5)$, in the non-physical log-absorbance to demonstrate the quality of signal.

Fig. 9c shows the difference between the data and a simulation using the Line-by-line Radiative Transfer Model (LBLRTM) with average atmospheric conditions reported by the meteorological instruments ($T = 25.1 \pm 1$ C, $P = 0.977 \pm 0.002$

atm, $N = 4.911 \pm 0.16 \times 10^{18}$ cm^{-3}) while Fig. 9d is an LBLRTM simulation using the fitted results ($T = 30.2$ C, $P = 1.035 \pm 0.053$ atm, $N = 4.825 \pm 0.04 \times 10^{18}$ cm^{-3}). Modest improvements resulted from using the temperature, pressure, and concentration derived from the spectra rather than the meteorological instruments, but very small errors in wavelength prevent smaller residuals unless line centers were included as a fit parameters. The fit line positions differ from the HITRAN data base by 0.00077 ± 0.00093 cm^{-1}, which compares favorably with the wavemeter best accuracy of 0.00033 cm^{-1}.

Rotational Temperature

Temperature is readily determined from the rotational intensity distribution. The integrated absorbance for each feature,

$$A^0_{\Delta K, \Delta J, K''} = \frac{g_{J'}}{g_{J''}} \frac{\mathbf{A}_{\Delta K, \Delta J, K''} \lambda^2_{\Delta K, \Delta J, K''}}{8\pi} \frac{(2J'' + 1)}{Q(T)} e^{\frac{-E_{K'', J''}}{kT}} NLf \tag{14}$$

can be evaluated to achieve a linear dependence on rotational energy,

$$\ln \left(\frac{A^0_{\Delta K, \Delta J, K''}}{(2J'' + 1) \lambda^2_{\Delta K, \Delta J, K''} \mathbf{A}_{\Delta K, \Delta J, K''}} \right) = \ln \left(\frac{NLf}{8\pi Q(T)} \right) - \frac{E_{K'', J''}}{kT} \tag{15}$$

Independent weighted linear fits of the observed absorbance for both the $^P P$ and $^P Q$ branches are are illustrated in Fig. 12.

The variance in fit absorbance, A_0 , as defined by the 95% confidence bound for the Voigt fit of each absorption feature, were employed for the weights. The $^P P$ and the $^P Q$ branches resulted in temperatures of 303.5 ± 2.0 K and 303.1 ± 1.8 K, respectively. The uncertainty in temperature is defined by the 95% confidence bounds in the slope parameter. The meteorological instruments used during the collection recorded temperature every minute, and the average temperature over the
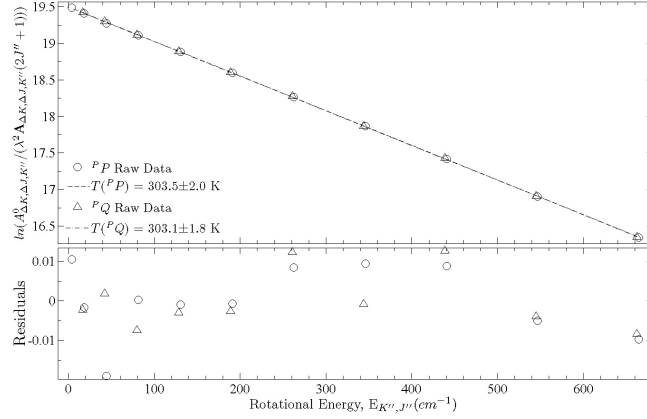
Figure 12. Estimations of temperature using the intensity distributions of the ^{P}P and ^{P}Q branches.

duration of collection was 299.5 ± 1 K with confidence derived from the instrument performance and varied by 3.6 K during the experiment. It should also be noted that the temperature sensors were not in-path, but were located near exterior doors of the building within 5 meters of each end of the path. The average outdoor temperature was about 290 ± 2 K, and may have contributed to the lower measured meteorological temperature.

Concentration

Concentration can be determined from the intercept of Eq. (15) and the data in Fig. 12 or by the depth of any rotational feature. Because each line is resolvable, concentration will be calculated for each line, with the average result giving the final estimate for concentration using Eq. (13). The resulting concentrations for each transition in the ^{P}P and ^{P}Q branches are shown in Fig. 13.

The uncertainty in concentration for a specific line is 0.1%. The standard deviation from line to line is greater than 0.8%. The best estimate for oxygen concentration is $4.82 \pm 0.04 \times 10^{18}$ molecules / cm^3. The weather station provides a somewhat
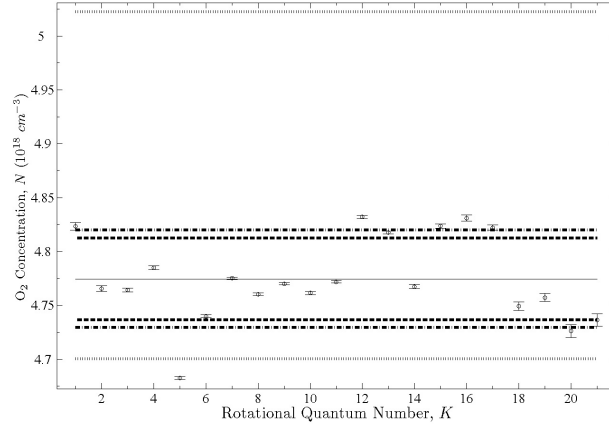
Figure 13. Estimation of concentration from each rotational line. The lightly dashed line gives the confidence bounds from the meteorological equipment, the heavily dashed-dotted line gives the confidence bounds from the concentration estimate using the y-intercept method, and the heavily dashed line gives the confidence 95 percent bounds for concentration using the fitted areas method.

larger estimate, $4.91 \pm 0.16 \times 10^{18}$ molecules / cm^3, with a larger uncertainty. Calculating concentration using Eq. (15) yielded results that agree with the line by line method giving $4.82 \pm 0.05 \times 10^{18}$ molecules / cm^3.

Pressure

Determining atmospheric pressure from the spectral data is less precise than concentration and temperature. The high resolution spectra exists with sufficient signal-to-noise to distinguish the Lorentzian component of the Voigt lineshape. Fitting a Voigt lineshape to each spectrally isolated line provides estimates of the Lorentzian, $\Delta\nu_L$, and the Doppler, $\Delta\nu_D$, full-width half maxima. The results of the pressure broadened lineshape, with fixed and unfixed Doppler widths, along with the expected linewidth using meteorological data and the HITRAN database are all illustrated in Fig. 14.

There is a strong rotational dependence to the pressure broadening rates due to
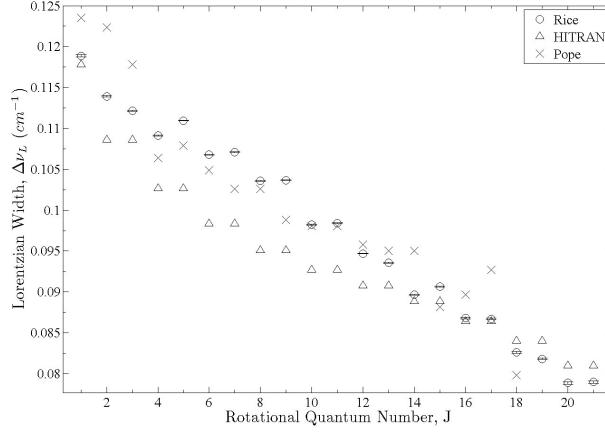
Figure 14. Estimation of pressure from meteorological data and the HITRAN database (triangles), from the fitted Voigt decomposition by fixing the Doppler width (circles), and by fitting to the Doppler and Lorentian width simultaneously (diamonds).

the inelastic energy transfer. [62] Voigt fits to individual lines, as shown in Fig. 12, resulted in Lorentzian widths with an average fit uncertainty of $\pm 0.2\%$ for each line. Using the distribution of pressures for individual features, pressure was determined as 0.975 ± 0.04 atm while the meteorological instruments reported 0.977 ± 0.001 atm. When temperature is unconstrained, the Doppler widths are reasonable and vary by $\pm 5.1\%$. This variation is demonstrated in Fig. 15.

By not assuming a fixed Doppler width, a small reduction of performance in spectral fitting results for pressure broadening, and decreased fitted temperature confidence boundaries by about 0.2 K. For additional comparison, pressure broadening widths calculated from data collected using a Bomem DA-8 Fourier Transform Spectromieter (FTS) [62] is included in the figure. Spectra in Pope's data was collected at 0.032 cm^{-1} resolution and had a signal-to-noise ratio of about 10 near the deepest rotational lines. The results compare favorably with the data collected here.

Extending collections to 1 km outdoor open paths is achieved by keeping the same general geometry but moving the turning mirror farther away from the transmit
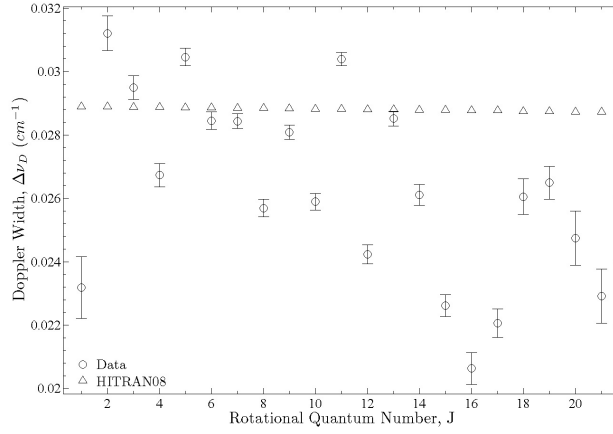
Figure 15. **Estimation of Doppler widths derived from NLLS fitting (circles) and from assuming T = 298.3 K (triangles).**

and receive telescopes and realigning until the best signal is obtained. 1 km paths produced deeper absorption features as demonstrated by the comparison of a 100 m path to a 1 km path in Fig. 16.

Implementation of longer path collections make the system more sensitive to telescope jitter and turbulence shown by the larger standard deviation about the baseline of $\Delta A \approx 0.012$, more than seven times larger than for the 100 meter path spectrum with the equivalent system settings. The absorbance between rotational pairs is clearly nonzero over longer paths and these spectral areas must be excluded from the baseline fitting process. Some of the deeper absorption features become nearly opaque over the 200 kHz width of the tuning laser, and the measurement of absorbance becomes limited by the system detection noise in the peak of a long path absorbance feature.

Monocular Passive Ranging

The process of viewing bright distant sources and using the depth of absorption bands to give an estimate of range to the source is referred to as monocular passive
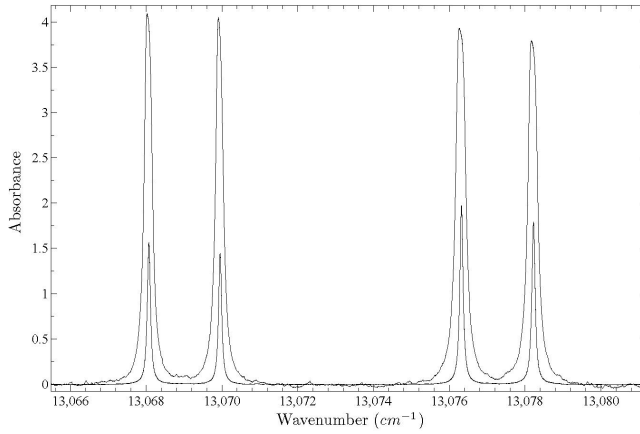
Figure 16. A comparison of spectra collected at 100 m and 1 km.

ranging (MPR) and can be used with a variety of atmospheric species. Oxygen is an excellent candidate for MPR, being spectrally isolated and having a stable atmospheric concentration. [38] The TDLAS instrument was deployed simultaneously with a non-imaging FTIR spectrometer to validate the MPR technique.

An example FTIR spectrum of the oxygen $X^3\Sigma_g^-$ to $b^1\Sigma_g^+$ transition at 1 cm^{-1} resolution with 4,000 coadded interferograms is demonstrated in Fig. 17a.

The FTIR instrument is fast framing with the ability to produce 10 interferograms per second at its maximum resolution of 1 cm^{-1}. The spectral region with no absorption features was used to fit a cubic baseline through the X-b transition in order to give the spectrum in absorbance as shown in Fig. 17b. The lower spectral resolution of the FTIR spectra is apparent in the R-branch, and even P-branch rotational lines are not fully resolved. Baseline noise is also significantly higher than TDLAS spectra.

In order to compare performance metrics between the two instruments, statistics concerning the accuracy of integrated absorbance are compared as a function of collection time. The uncertainty in absorbance from the fully integrated spectra as a function of the number of scans is shown in Fig. 18a along with a single TDLAS scan
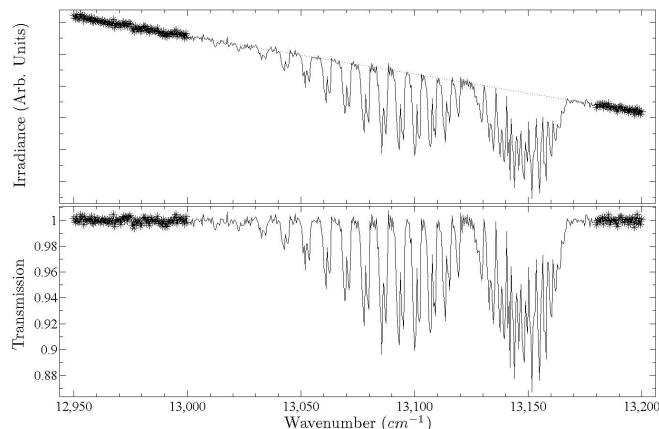
Figure 17. An example spectrum produced from 4,000 co-added FTIR scans, before (a) and after (b) the baseline correction. The points used for fitting a baseline to raw FTIR data are shown by asterisks.

having an absorbance converges to 5.915 with a standard deviation of 0.046.

The FTIR spectra exhibit an integrated absorbance of 5.2-6.2, converging to 5.784 with a standard deviation of 0.252. The smaller variance in TDLAS absorbance is shown by dashed horizontal lines in Fig. 18a. The standard deviation of integrated absorbance as a function the number of co-adds in Fig. 18b give the confidence bounds found in Fig. 18a for FTIR data points while overall confidence for statistical performance of FITR integrated absorbance are shown by curved dotted lines. It should be noted that the data shown here uses both the P and R branches, but the final TDLAS implementation can allow for a single branch to be used for integrated absorbance with similar performance outcomes.

The time required to obtain a single FTIR spectrum (0.1 s) is shorter than a TDLAS scan (16 s). The standard deviation of integrated absorption is characterized in terms of signal-to-noise versus collection time in Fig. 19.

The raw collected baseline defines the signal and the noise is defined by the RMS variation about that baseline. The signal-to-noise from each instrument using this definition results in similar performance. Collection times given can be greatly reduced
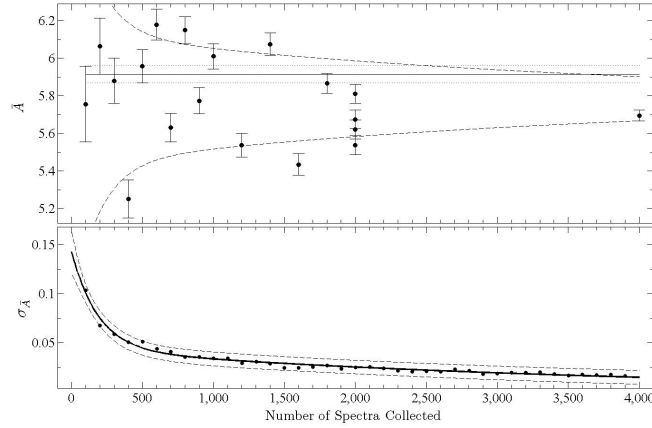
Figure 18. Demonstration of the statistical standard deviation of integrated absorption (a) as a function of the number collected spectra. Statistics from the FTIR data were used to assign confidence bounds for integrated absorption for FTIR collections (b) and expected performance of FTIR collections as a function of scan time. Results for integrated absorption are shown with the horizontal line with one standard deviation of confidence lines for a consecutively long-running TDLAS collection are also shown in (a).
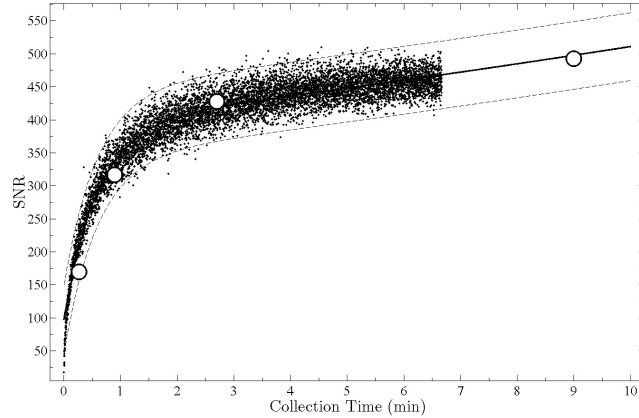
Figure 19. Demonstration of (dots) FTIR and (open circles) TDLAS signal-to-noise as a function of collection time.
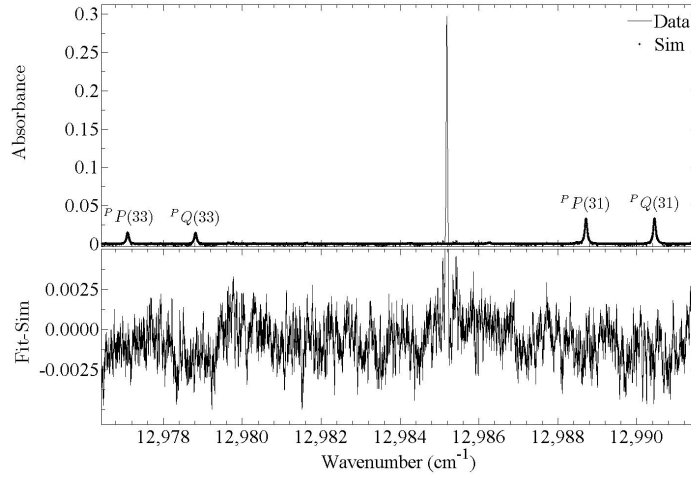
Figure 20. The location of the potassium D_1 line between the $K"=31$ and 33 lines in the molecular oxygen P-branch.

for the TDLAS instrument if the lineshape of absorption features is not desired, at the expense of lost information regarding pressure and possibly temperature. The TDLAS instrument achieves the same performance in determining the total absorbance for the same acquisition time, while adding detailed information regarding lineshape and rotational distribution.

DPAL Atmospheric Transmission

A final experiment was performed to demonstrate the application of this TDLAS device for field studies of laser transmission. The potassium variant of the Diode Pumped Alkali Laser (DPAL) operates on the D_1 line near 12985.185 cm^{-1}, [82] in the high rotational limit of the O$_2$ (X-b) (0,0) P branch, as shown in Fig. 20.

The spectra were acquired over a 150 meter outdoor path during nighttime conditions during weather periods with low wind. During the data collection, a Triad Technologies potassium vapor cell with zero pressure (no buffer gas) was placed in the optical path just before the detector on the receive telescope. With the cell in

place, collections were conducted with cell temperatures of 65 C giving an approximate vapor pressure of 2×10^{-5} mbar. Temperatures were controlled with a Watlow temperature controller and the cell was encased in a custom aluminum heat block with thermocouples placed in bored holes in the aluminum block within 4 mm of the vapor cell. Fig. 20 demonstrates that the potassium D_1 absorption line lies nearly midway between the P branch $K"=31$ and $K"=33$ ($v"=0$, $v'=0$) oxygen lines.

The LBLRTM simulation using the TDLAS extracted atmospheric conditions is also shown. The K DPAL system operates at high pressure, 1-20 atm, depending on the spectral width of the diode pump lasers. The collision induced broadening and lineshifts can shift the K D_1 line by up to 0.5 cm^{-1}. Also note, at longer path lengths the O_2 (X-b) hot bands have rotational lines closer to the K D_1 line and could degrade laser transmission. Further characterization of atmospheric transmission for the K, Rb, and Cs variants of the DPAL is currently in progress using the current TDLAS apparatus.

Typical spectra collected using the TDLAS technique compares favorably compared to the MUMAS technique outlined in Arita, et al. [7]. While TDLAS collection times are longer, the resulting raw spectrum is detailed enough to easily extrapolate concentration, temperature, and pressure of observed atmospheric species without extensive post-processing. Sensitivity of MUMAS is reported to be 0.01% for 128 averaged spectra, while the TDLAS technique can detect 0.2% over a single scan. Measured values for concentration, temperature, and pressure for MUMAS collections of the O2(X-b) is reported as $\pm$ 2% for each measurement, while TDLAS measurements are $\pm$ 0.7%, $\pm$ 0.8%, and $\pm$ 4% respectively.

Conclusions

A system to conduct open-path TDLAS measurements has been developed to investigate the molecular oxygen A-band $X^3\Sigma_g^-$ to $b^1\Sigma_g^+$ transition lines near 760 nm. The resolution of the system was limited to laser linewidth of less than 300 kHz and was sufficient to separate Voigt lineshapes into their Lorentzian and Doppler components. Analysis of the data has shown that accurate estimates for temperature, concentration, and pressure can be found. Temperature was determined to within 1.3%, concentration to 1.6%, and atmospheric pressure to less than 10%. System noise is dominated by some combination of turbulence in the atmospheric path and telescope jitter. The laser source can easily be changed to investigate other spectral regions. When compared to collection times using FTIR instruments, signal-to-noise is similar however the TDLAS instrument can record spectral lineshapes of absorption features. The TDLAS instrument has been deployed to laser test ranges, operated at temperatures as low as -10 C for several days without performance degradation. Path lengths have been extended to 1 km with minimum detectable changes in absorbance of $\Delta A = 0.06$.

V. Open-path atmospheric transmission for the diode pumped cesium laser.

A tunable diode laser absorption spectroscopy (TDLAS) device was used to propagate a laser over outdoor atmospheric open-paths. Water vapor absorption lines near the Cs Diode Pumped Alkali Laser (DPAL) wavelength of 895 nm were investigated. Temperature, pressure, and water vapor concentration were determined for 150 meter and 1 km open-paths with statistical errors of $\approx 0.2\%$. Comparison with meteorological instruments yields agreement for the 1 km path to within 0.6% for temperature, 3.7% for pressure and 2.4% for concentration.

Introduction

The diode pumped alkali laser (DPAL) was first proposed in 2001 as an alternative to high power, diode pumped solid-state lasers [44][47]. Diode laser excitation on the D_2 $^2S_{1/2}$ - $^2P_{3/2}$ transition and collisional energy transfer to the spin-orbit split $^2P_{1/2}$ state, yields lasing on the D_1 $^2P_{1/2}$ - $^2S_{1/2}$ transition in potassium, rubidium, or cesium vapor. The DPAL system offers excellent thermal control, good beam quality, and a quantum efficiency of 95-99%. A high power, >1 kW, system with 48% optical-to-optical efficiency has recently been reported. [14]

The cesium version of the DPAL system has received considerable attention. [28, 45, 63, 94, 96, 97, 98, 99, 100, 101, 102] Slope efficiencies exceeding 80% have been demonstrated [96], exciplex assisted pumping schemes [63], and transverse excitation with an unstable resonator have been explored [102]. The larger spin-orbit splitting in cesium generally requires a molecular collision partner to accelerate the fine structure mixing. [100] Rare gases are also usually employed at pressures of 1-10 atmospheres to broaden the absorption profile and better match the diode laser spectral distribution. [60, 61]

Interest in the atmospheric transmission characteristics of these alkali lasers has led us to develop of a tunable diode laser absorption spectroscopy (TDLAS) device for long open-path, >1 km, field deployment. [65] The system was originally designed to study the potassium DPAL that operates in a narrow window between the rotational features of the O_2 X-b (0,0) transition near 760 nm. In the current work, we extend the TDLAS system's functionality to the Cs DPAL at wavelengths near 894 nm. There are several moderate strength water lines and very weak CO_2 and OH lines in the vicinity of the Cs DPAL wavelength. [74]

TDLAS has previously been used to explore atmospheric water vapor absorption features for a number of applications. Water vapor detection in the Martian atmosphere has been demonstrated for a 120 cm open-path and a 10^{-4} minimum detectable absorption during a single scan. [9, 25] The measurement of water vapor with an uncertainty of about 1.14%, was demonstrated with Voigt fits having residuals only 1 - 3 times larger than the noise. Other groups use diode lasers to investigate open-path water vapor on airborne UAVs [76] and manned [21] platforms. For example, a 1.39 m diode laser over an open folded 50 cm absorption path placed in the free-stream air using an external probe with a signal-to-noise ratio of 3 and a minimum measureable absorbance of 10^{-5} $Hz^{-1/2}$ was demonstrated on a NASA P3B aircraft. [76] A system with a diode operating near 1.4 m was deployed on a DC-8-72 between a quartz fuselage window and a retro-reflector mounted on the plane's outboard engine nacelle. [21]

Several balloon-borne instruments have measured water vapor concentrations to within 10% over the upper troposphere and lower stratosphere. [27, 26, 24, 23, 37] One device employs a 56 meter Herriott cell. [23] Atmospheric sampling for altitudes of 1 - 31 km yields mixing ratio with errors of less than 10%. [26] Absorbance detection limits of 10^{-5} have been demonstrated. [23] A more recent article outlines a very

Figure 21. Diagram of TDLAS system.

similar device with an updated Herriott absorption cell having with different paths for water vapor (36 meter path) and methane (74 meter path). [37]

Finally, diode lasers operating near 1.37 m are used to determine transpiration rates of plant leaves giving water vapor concentrations to within 5%. [42] A more recent article employs similar methods investigating stronger vibrational bands near 2.7 m and also resolves water vapor spatially by moving the absorption path using a mechanical scanning platform. [92] Using diode lasers over open-paths is a relatively low risk method that can investigate more than a single spatial location and can have detection limits in the neighborhood of 10^{-5} in absorbance.

TDLAS Device

The tunable diode laser absorption spectroscopy instrument is shown schematically in Fig. 21.

A detailed description of the device configuration and method for collecting spectra have previously been discussed. [65, 64] The tunable diode is a New Focus Velocity

laser model 6318 with a 10 mWatt maximum output, a 890-910 nm tunable range, and less than a 300 kHz linewidth. The laser source near 900 nm can easily be changed to investigate other spectral regions of interest with minimal changes to the overall system. After amplitude modulation by a Thor Labs EO-AM-NR-C1 free space modulator at 102 kHz (lock-in maximum useable modulation rate), the laser is fiber coupled and expanded to nearly fill a military grade 12.5 inch RC Optical Ritchey-Chrtien transmit telescope. The laser beam is directed across an open-path and then received by a second identical telescope. Two Thor Labs PDA100A Si detectors are used to measure the reference (or sent) and transmitted (or received) signals, and are analyzed by Stanford Research Systems SR850 dual-phase lock-ins and recorded by a National Instruments USB-6251 DAQ. Pellicle beam splitters of 2 m thickness are used to minimize etalon effects. The reference intensity is measured late in the optical train (immediately prior to the telescope beam expansion) and can be attenuated to balance transmitted and received signals. A High Finesse WSU-2 wavemeter is used to determine the frequency axis and is calibrated with a 2 MHz fiber-coupled SIOS SL-03 frequency-stabilized HeNe laser to achieve a better than 10 MHz accuracy. All hardware is connected to and controlled by a PC using MATLAB®. During an experiment, the laser is finely tuned over an approximately 0.1 nm range by driving a piezo to change cavity length, and then coarsely tuned to the next spectral region. The process is repeated for nearly 200 free spectral ranges to cover the available 20 nm spectral scan. Calibration of the frequency axis, baseline removal, and further spectral processing have also been reported. [65, 64] Noise when the system is deployed outdoors is generally dominated by telescope jitter and atmospheric turbulence over the path. For shorter paths near 100 meters, these effects are usually small and less than 1% of the signal. The maximum open-path distance is about 2 km, a limitation imposed by the Quickset QPT-130 ruggedized pan and tilt mounts.
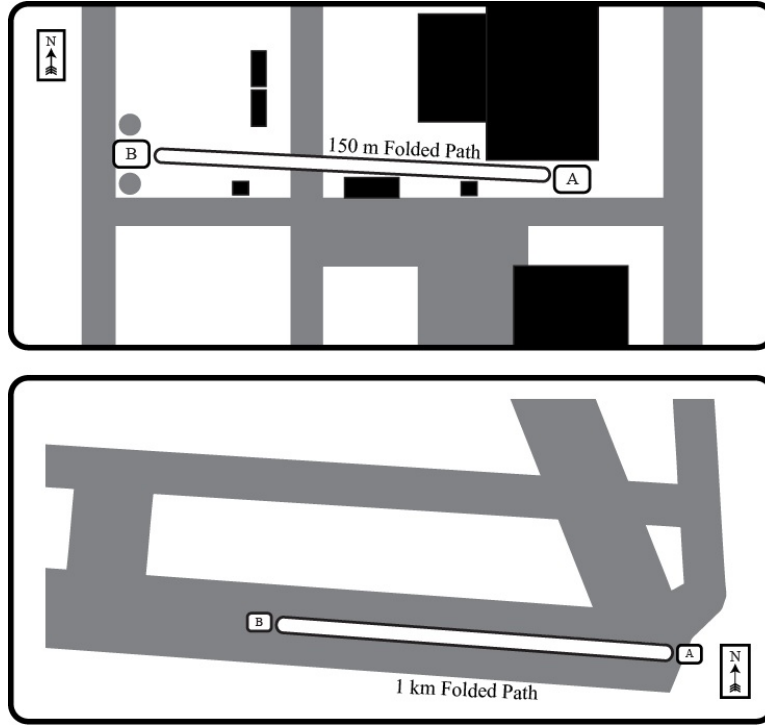
Figure 22. Data collection geometry for the 150 m (top) and 1 km (bottom) paths showing the position of the TDLAS transmit and receive telescopes to the east (A) and the turning mirror west side of the open-path (B). Buildings are depicted in black while pavement is depicted in grey. Wind prevailed in the northerly direction for both cases.

Collections were performed over a short 150 meter and a longer 1 km open path during fair weather conditions with site geometries shown in Fig. 22.

The send and receive telescopes were separated by 1 meter, each viewing a 6 inch flat mirror at 1 meter above the ground. All collections were performed at night to operate with minimal turbulence. Two NIST-certified Davis Vantage Pro2 weather sensors were placed near the telescope and mirror for the 150 m path. Temperature, pressure, and relative humidity were recorded at 15 minute intervals with 95% confidence bounds of 1 C, 2 hPa, and 6%, respectively. The 150 m total path length spectra were recorded on September 8th, 2011 over cut grass with average meteorological conditions of 12.3 C, 996.7 hPa, and 87.2% relative humidity. The 1 km path length spectra were collected on November 24th, 2011 over a paved runway surface
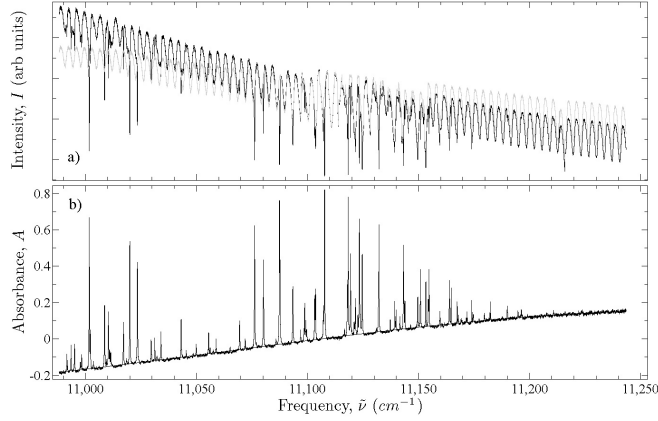
Figure 23. An example spectrum demonstrating a) the I and I_0 detector response and b) the A= -log(I_t/I_0) for water vapor over tunable laser range and the typical baseline curvature.

with average conditions of 4.5 C, 994.3 hPa, and 90.7% relative humidity recorded by a single Davis Vantage Pro2 sensor in the center of the folded path.

Results

A typical absorption spectrum from 11,000 to 11,250 cm^{-1} for an atmospheric path length of 100 m is shown in Fig. 23a.

The periodic modulation in the send reference intensity, I_0, occurs throughout the 171 free spectral range scans of the diode laser and comes from etalon effects from the instrument. The laser scan rate is 0.002 nm/s and signal is sampled at 512 Hz. While the figure demonstrates a single sweep, sweeps can be averaged to improve the signal-to-noise ratio. The received signal, I_t, has a slightly different response, so that the observed spectral absorbance,

$$A(\tilde{v}) = -\ln\left(\frac{I_t(\tilde{v})}{I_0(\tilde{v})}\right) b(\tilde{v}) = b(\tilde{v})\sum_i \sigma_i(\tilde{v})N_i L \tag{16}$$

includes a frequency dependent cubic baseline, b, in addition to the absorption cross-
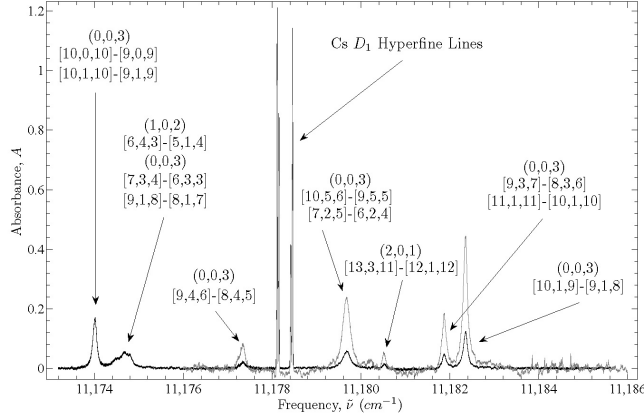
Figure 24. Example absorption spectra for: 150 m (black) and 1 km (grey) open-path outdoor collections with low pressure Cs D_1 hyperfine lines located in path.

section, $\sigma_i(\tilde{\nu})$, for each atmospheric constituent, i, with concentration, N_i. All of the spectral features in Fig. 23b are assigned to water vapor and exhibit lineshapes limited only by the atmospheric pressure broadening. Fig. 24 demonstrates the spectra from the 150 meter and 1 km collections in the vicinity of the Cs D_1 $^2S_{1/2}$ -$^2P_{1/2}$ line, with the baseline removed.

All atmospheric absorption lines in the spectrum are a result of water vapor, and are assigned using the vibration quantum numbers of the upper level $(v1', v2', v3')$ and the ground vibrational $(0, 0, 0)$ level is common for all the features. Rotational states are labeled with the quantum numbers $[J', K'A, K'C] - [J", K"A, K"C]$ for the upper and lower states, respectively. A blended pair of lines $(0, 0, 3)$ $[10, 0, 10] - [9, 0, 9]$ and $(0, 0, 3)$ $[10, 1, 10] - [9, 1, 9]$ make up the first feature near 11,174 cm^{-1} while another three lines near 11,175 cm^{-1} create a broader shape just to the right. The two features on either side of the Cs D_1 emission line are the $(0, 0, 3)$ $[9, 4, 6] - [8, 4, 5]$ on the left and the $(0, 0, 3)$ $[7, 2, 5] - [6, 2, 4]$ blended with the $(0, 0, 3)$ $[10, 5, 6] - [9, 5, 5]$ on the right. There are additional smaller water vapor lines in this spectral area, but they are not immediately visible over these shorter path lengths. The 150

55

m collection has a baseline signal RMS from 11,184 to 11,185 cm^{-1} of 0.00169 in absorbance with a peak signal located on the blended pair of water lines at 11,182.36 cm^{-1} of 0.1238 giving a signal-to-noise ratio of about 73.2. The 1 km collection exhibited a baseline signal RMS of 0.0080 in absorbance with the same water vapor peak absorbance of 0.4437 giving a signal-to-noise ratio of 54.9. As path lengths increase noise from path turbulence and system pointing jitter increase at a rate greater than the absorption signal increases. During the 1 km collection a Scintec BLS900 turbulence measurement device was setup beside the TDLAS device with the transmitter placed by the turning mirror and the receiver between the transmit and receive telescopes giving a 500 m path. The BLS900 device is limited to C_n^2 measurements between 3×10^{-14} and 3×10^{-10} for 500 m path collections. During the experiment values for C_n^2 were below the lower threshold. Even assuming a high value of 1×10^{-14} for turbulence, RMS beam wander from turbulence over a 1 km path is less than 12 mm. During the same experiment the alignment laser was seen to move on a target board by over 4 cm with movements that correlated in time with wind gusts. While both turbulence and platform jitter both contribute to noise, at 1 km paths with turbulence under 1×10^{-14} platform jitter is likely to be the primary cause of baseline noise.

A low pressure (no buffer gas) Cs vapor cell inside a heater block at 30 C was placed in the path between the receive telescope and the detector to provide a reference for the Cs DPAL wavelength. The strong, narrow absorption features near 11,178 cm^{-1} in Fig. 24 are due to the D_1 $^2S_{1/2}$ -$^2P_{1/2}$ transition in cesium. The hyperfine structure of this transition is easily resolved. The hyperfine splittings are approximately 9.192 and 1.168 GHz for the ground and excited states, respectively, as shown in Fig. 25.

A best estimate for the atmospheric temperature, pressure, and water vapor concentration were obtained using the Line-by-Line Radiative Transfer Model (LBLRTM)
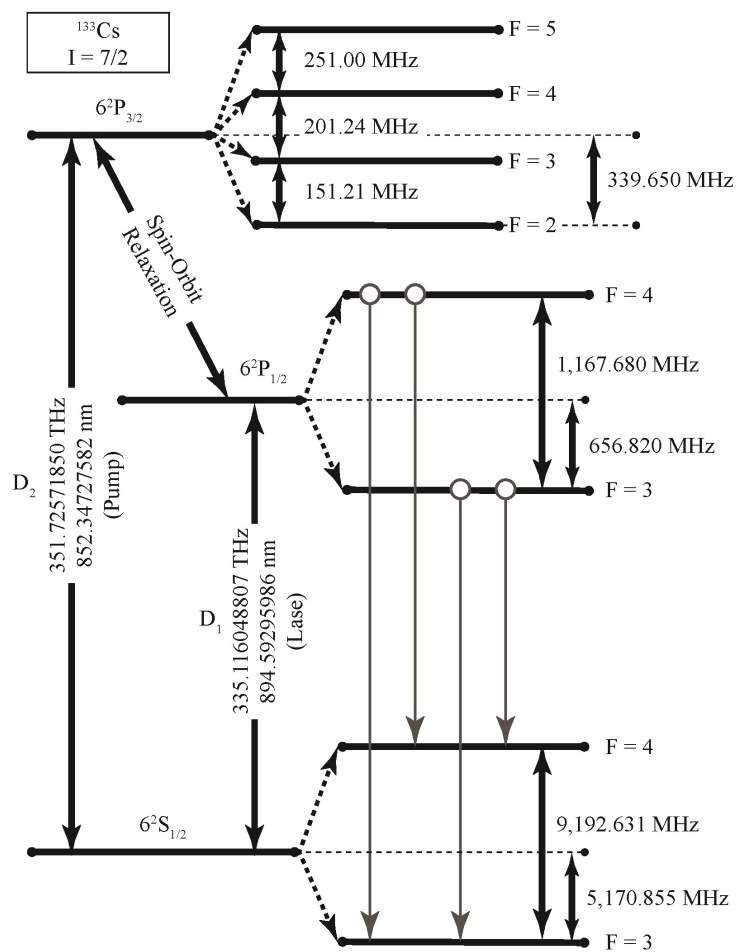
Figure 25. Structure of Cs including 4 hyperfine lines that make up the lasing emission on the D_1 line.

[19] in conjunction with the HITRAN database [74] and knowing the overall path length, a non-linear least squares fitting process was used by simulating an atmospheric spectra defined for a homogenous atmosphere with a single temperature, pressure, and water vapor concentration as fit parameters. The cubic baseline was removed before the fitting process using only data points that lie outside of the Cs hyperfine lines and the water vapor lines present in the spectrum. The iterative fitting process also includes the 95% confidence interval for each fitted parameter based on results from each of the iterative fits, giving the final estimates for the average path temperature, pressure, and water vapor concentration. Fig. 26a illustrates the fit quality for the 150 m path with residuals in 6b resulting in an estimated temperature of 15.5 C (288.6±0.15 K), a pressure of 993.8±0.9 hPa, and a water vapor concentration of $3.096 \pm 0.004 \times 10^{17}$ molecules per cm^3. For comparison, the meteorological conditions during the test are reported in Figs. 27a, 27b, and 27c.

The agreement is poorer than the statistical error from the spectral fitting and agree within 2.4%. However, the weather station data indicates variations within test of up to 5%. The fit results for the 1 km path yield a temperature of 6.1 C (279.2±0.20 K), a pressure of 958.3±1.5 hPa, and a water vapor concentration of $1.940 \pm 0.004 \times 10^{17}$ molecules per cm^3, all agreeing with the meteorological instruments to within 3.7% or less with the fit shown in Fig. 26c with residuals in Fig. 26d. The meteorological data collected during the 1 km experiment is shown in Figs. 27d, 27e and 27f. The particularly poor estimate for pressure for the long path is easy to understand considering the fit to pressure is especially sensitive to the Lorentzian (wing) portion of the Voigt, making it a parameter especially sensitive to the overall signal-to-noise ratio. Structured residuals are evident resulting from minor wavemeter errors expected because of the ridged line center constraints used in the fit. Including linecenters in the fit removes structure in the residuals leaving only noise and
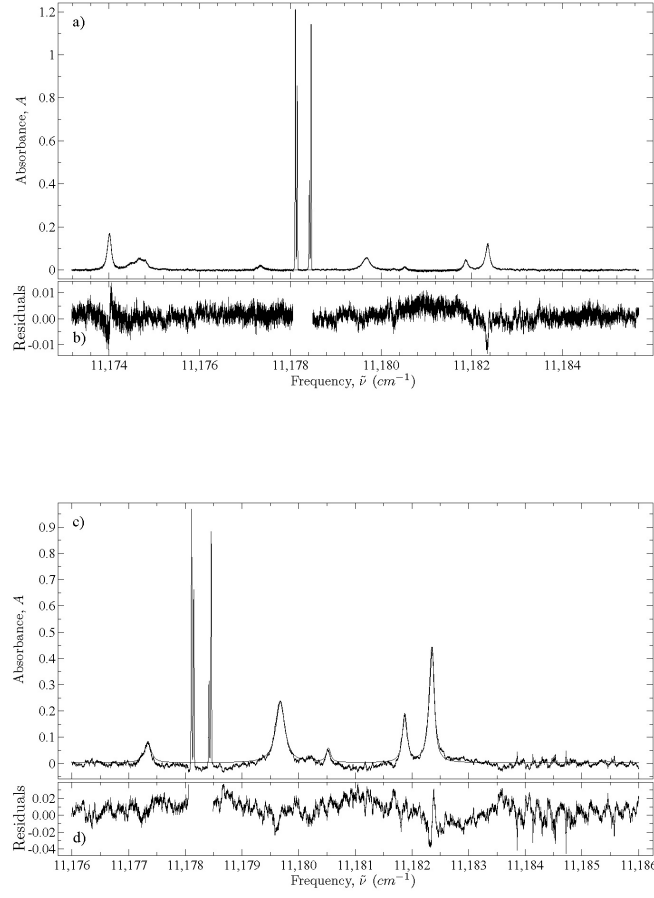
Figure 26. Demonstration of a) 150 m spectrum with NLLS fit and b) residuals, c) 1 km spectrum with NLLS fit and d) residuals.
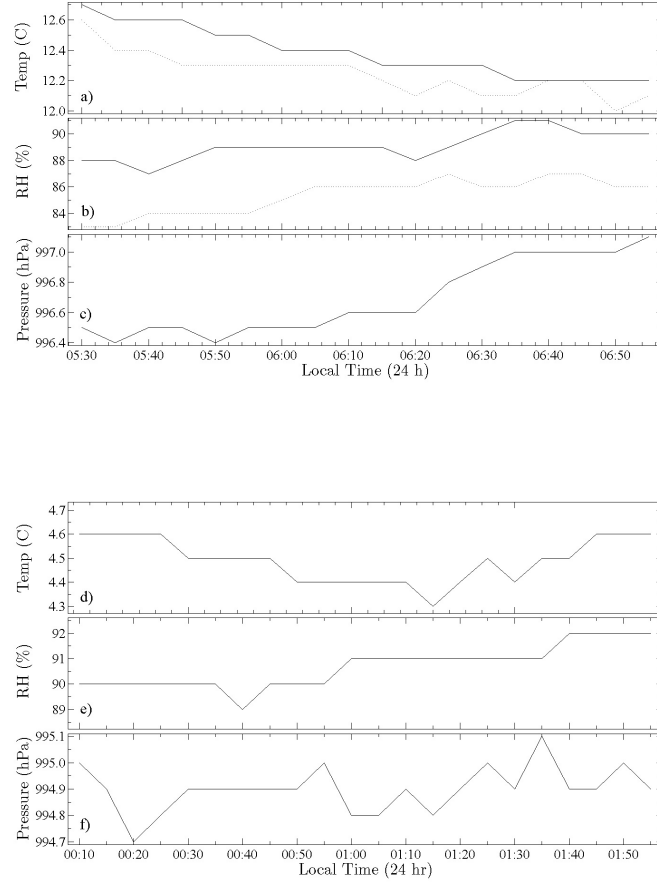
Figure 27. Variations in temperature, relative humidity, and pressure during experimental collections for the 150 m path (a,b,c) with a sensor located near the transmit telescope (black) and another near the turning mirror (grey) and 1 km path lengths (d,e,f) with a single sensor placed in the center of the path.

reducing the residual RMS by about 20%. Adding linecenters as a fitting parameter increases fitting complexity without improving overall fitting results, and results from this fitting method are not used.

Discussion

Having anchored LBLRTM simulations to observed TDLAS spectra over example paths, atmospheric simulations can be compared to Cs laser lineshapes. DPAL systems require 1-10 atmospheres of added buffer gases for efficient operation. High power diode bars and stacks exhibit broad spectral lineshapes relative to atomic, gas phase absorption features. Pressure broadening of the alkali D_1 and D_2 lines occur at rates of ≈ 20 MHz/Torr. For example, argon broadens the Cs D_1 line at 18.31 MHz/Torr. [60] Furthermore, a buffer gas is required to induce transitions from the pumped $^2P_{3/2}$ level to the $^2P_{1/2}$ level. The fine structure splitting in Cs is relatively large (10.4 GHz), as shown in Fig. 25. Molecular collision partners such as methane or ethane are typically employed to increase the rate of collisional energy transfer. [14] Several Cs lasers have been demonstrated with powers of up to 49 W [99] with either helium or argon and ethane buffer gases at total pressures of about 1 atmosphere. Fig. 28 shows a demonstration of a 1 km homogenous atmosphere at 0 C (273.15 K), 1 atm (1013.25 hPa), and 50% RH (8.10×10^{17} molecules per cm^3) at ground level alongside three examples of Cs gain profles, one with only 100 Torr C_2H_6 and 0 Torr He, one with 100 Torr C_2H_6 and 760 Torr He, and one with 100 Torr C_2H_6 and 7,600 Torr He. [61, 59]

The simulation with only 100 Torr C_2H_6 shows some hyperfine structure. Not all four hyperfine lines are resolvable, but each pair of hyperfine lines are distinguishable and only the far wings of the gain profile lie over any water vapor absorption lines. The Voigt lineshape has a Doppler component of width 0.032 cm^{-1} and a Lorentzian
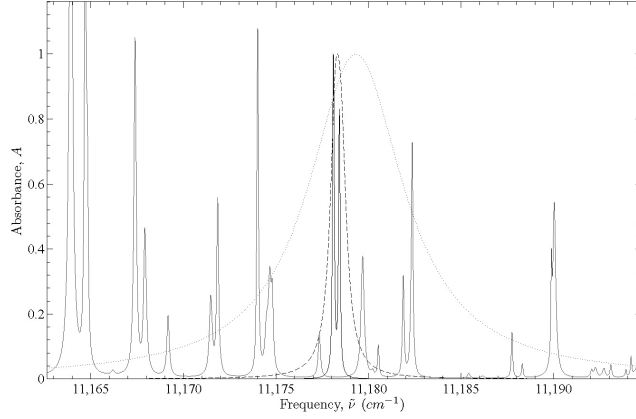
Figure 28. Simulation of 1 km horizontal atmospheric path (grey) with the simulated gain profiles of a Cs vapor gain cell with 0 atm He (solid black), 1 atm He (dashed black) and 10 atm He (short dash back), each with a buffer gas mixture including 100 Torr C_2H_6. Gain profiles are normalized to one.

width of 0.194 cm^{-1} for this low pressure simulation. With 1 atm of He, the hyperfine lines are completely washed out and the Cs absorption profile begins to encompass the $(0, 0, 3)$ $[9, 4, 6] - [8, 4, 5]$, $(0, 0, 3)$ $[7, 2, 5] - [6, 2, 4]$, and $(0, 0, 3)$ $[10, 5, 6] - [9, 5, 5]$ water vapor lines. With 10 atm of added to the 100 Torr C_2H_6, the gain profile completely surrounds many major water lines and is visibly blue shifted. If the same amount of laser power is distributed across each Cs absorption profile, the emission line from a high pressure Cs gain cell would encounter significant water vapor absorption features. This absorption would also contribute to higher thermal blooming for high energy lasers. While a lower pressure (1 atmosphere) variant of the Cs DPAL would be preferable for atmospheric propagation, the demand for narrow banding the pump diode bars requires emerging technologies such as external cavity volume Bragg gratings (VBG). Narrow banding of high power diode bars to pump the Rb DPAL system have recently been developed with linewidths of 18 GHz, enabling the 1 atmosphere variant of the DPAL laser. [36]

It should also be noted that observed spectra of highly pressure broadened Cs
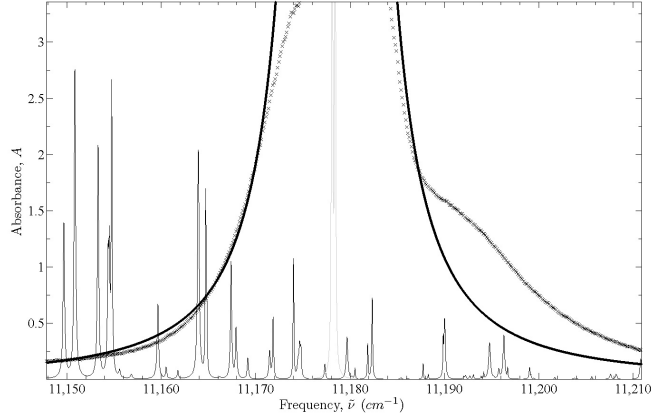
Figure 29. Simulation of 1 km horizontal atmospheric path (thin black) to simulated Cs cell with 100 Torr C_2H_6 (grey), with 3 atm of Ar (thick black) and a laboratory Cs cell with 3 atm of Ar (x).

exhibit asymmetric line shapes are not modeled here. The theoretical D_1 lineshape for a Cs gain cell with 3 atm of argon is depicted in Fig. 29 alongside a symmetric Cs absorption spectrum [52]. On the blue side a bump in the absorption profile is seen experimentally but not modeled here.

It should be noted that this spectral asymmetry could result in Cs DPAL with a spectrally wider emission line than indicated in the figures above. The DPAL gain is high with a low cavity Q, unstable resonators are likely required for high power operation. Rather than consider line narrowing associated with the laser resonator, we use the small signal gain lineshape as a conservative estimate of the laser linewidth.

A scenario was created with a slant range of 100 km with both starting and ending points at 10 km altitudes, a geometry having a low point altitude in the center of about 9.8 km due to earth curvature. LBLRTM was used to compute optical depth and configured to calculate Voigt lineshapes to within 25 cm^{-1} of their respective line centers, to include all continuum, and using an atmospheric profile created by LBLRTM with the 1976 US Standard model. No aerosol effects were included in the simulation. Fig. 30 shows a close-up highlighting the 100 km high altitude path
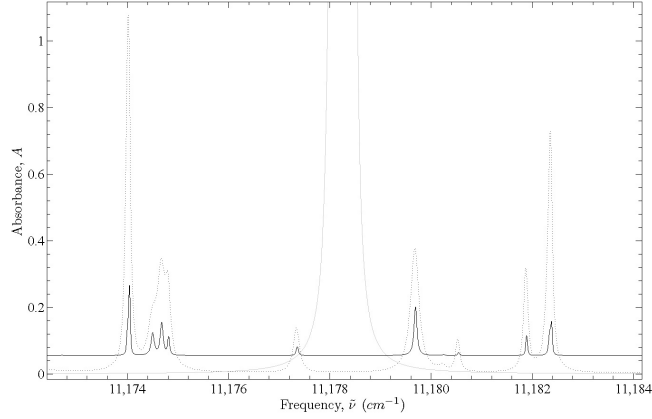
Figure 30. Simulations of a 10 km altitude atmospheric path with a 100 km slant range (black line), a 1 km horizontal atmospheric path (dotted line), and a 100 Torr C_2H_6 gain cell (grey).

compared to the 1 km low altitude atmospheric path and low pressure Cs gain profile - both shown also in Fig. 29.

Molecular scattering over the long path is obvious in the baseline, and with a low pressure of 268.5 hPa ($\approx$ 0.26 ATM) the lines are visibly narrower than the low altitude case.

Conclusion

The TDLAS system is shown to collect information for molecular absorption over atmospheric paths from hundreds to thousands of meters. Accuracy in the wavenumber axis is limited to the spectral reference used and is approximately +/- 10 MHz. Noise is primarily dominated from effects of telescope and mirror jitter with RMS jitter for 150 m and 1 km paths of 0.00169 and 0.0080 giving a signal-to-noise ratio of 73.2 and 54.9, respectively, in absorbance. The high-quality spectral scans from the system can be used for a variety of tasks, including investigation of multi-species molecular absorption, estimation of temperature, pressure, and concentration for water vapor with results to within 2.4% or less from 150 m paths and 3.7% for 1 km

64

paths of meteorological data, all using a nonlinear least squares fit with LBLRTM. Overall Cs DPAL atmospheric transmission will be excellent over atmospheres with very little water vapor. Cs DPALs with lower pressure gain cell configurations will have the best atmospheric transmission over well-hydrated atmospheric paths while Cs DPALs with spectral broad emission lines will suffer from water vapor absorption which may in turn cause molecular absorption induced thermal blooming. Asymmetry of highly pressure broadened Cs absorption features may result in spectrally broader Cs DPALs.

VI. Molecular absorption of diode pumped alkali lasers

Molecular oxygen absorption lines near the potassium (K), and water vapor absorption lines near the rubidium (Rb), and cesium (Cs) Diode Pumped Alkali Lasers (DPAL) at wavelengths near 770 nm, 795 nm, and 895 nm, respectively, were investigated using the Line-by-Line Radiative Transfer Model (LBLRTM) with the High Energy Laser End-to-End Simulation (HELEEOS). A tunable diode laser absorption spectroscopy (TDLAS) device was used to anchor simulations to outdoor 150 m atmospheric open-path collections. The Cs DPAL operates in the wing of water vapor lines and exhibits absorbances similar to the Chemical Oxygen Iodine Laser (COIL). The Rb DPAL absorbance is lower for many engagement scenarios with A = 0.002 - 0.2. The K DPAL operates between the rotational lines of O_2 $X^3\Sigma_g^-$ to $b^1\Sigma_g^+$ with absorbances as high as 0.07 for tactical air-to-ground missions.

Introduction

The diode pumped alkali laser (DPAL) was first proposed in 2001 as an alternative to high power, diode pumped solid-state lasers. [44] Laser excitation on the D_2 $^2S_{1/2}$ - $^2P_{3/2}$ (pump) transition and collisional energy transfer to the spin-orbit split $^2P_{1/2}$ state, yields lasing on the D_1 $^2P_{1/2}$ - $^2S_{1/2}$ (emission) transition in potassium (K), rubidium (Rb), or cesium (Cs) vapor. The energy level structure used in DPAL operation for K, Rb, and Cs are similar in nature, shown in Figs. 31, 32, and 25, respectively, giving pump and laser emission locations along with emission hyperfine lines.

The three level structure they each share results in high efficiency with losses mostly incurred from the spin-orbit relaxation from the $^2P_{3/2}$ - $^2P_{1/2}$. The spectral width of the pump and emission lines are primarily dependent on pressure and buffer
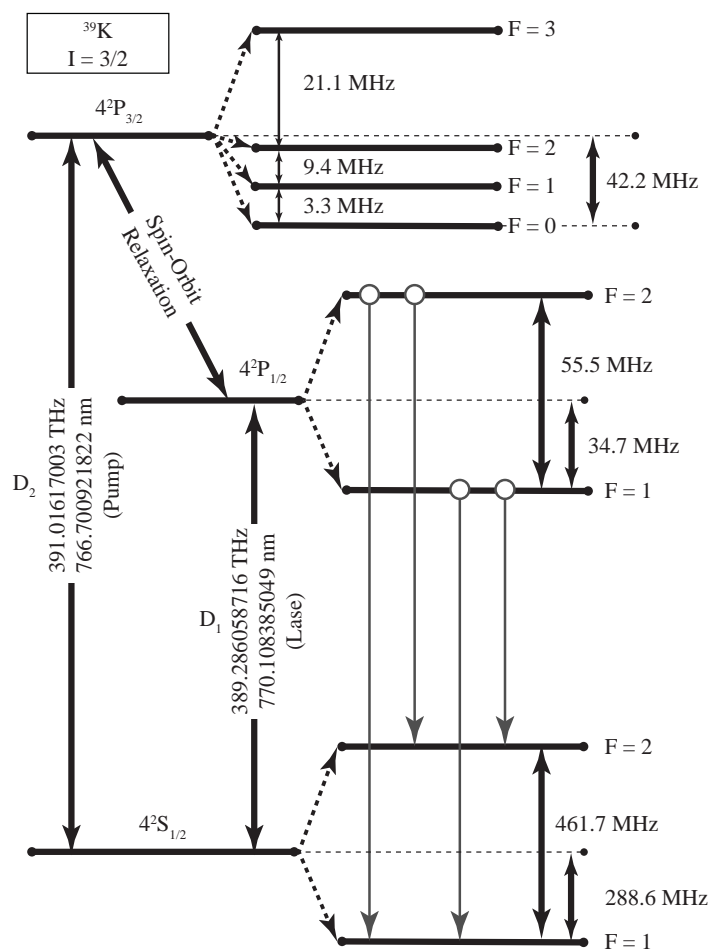
Figure 31. Structure of potassium (K) DPAL operation from pumping the D_2 line near 766.7 nm, with spin-orbit relaxation from the $4^2\mathbf{P}_{3/2}$ to the $4^2\mathbf{P}_{1/2}$ levels resulting in lasing emission from the D_1 line near 770.1 nm made up of 4 hyperfine lines closely spaced.
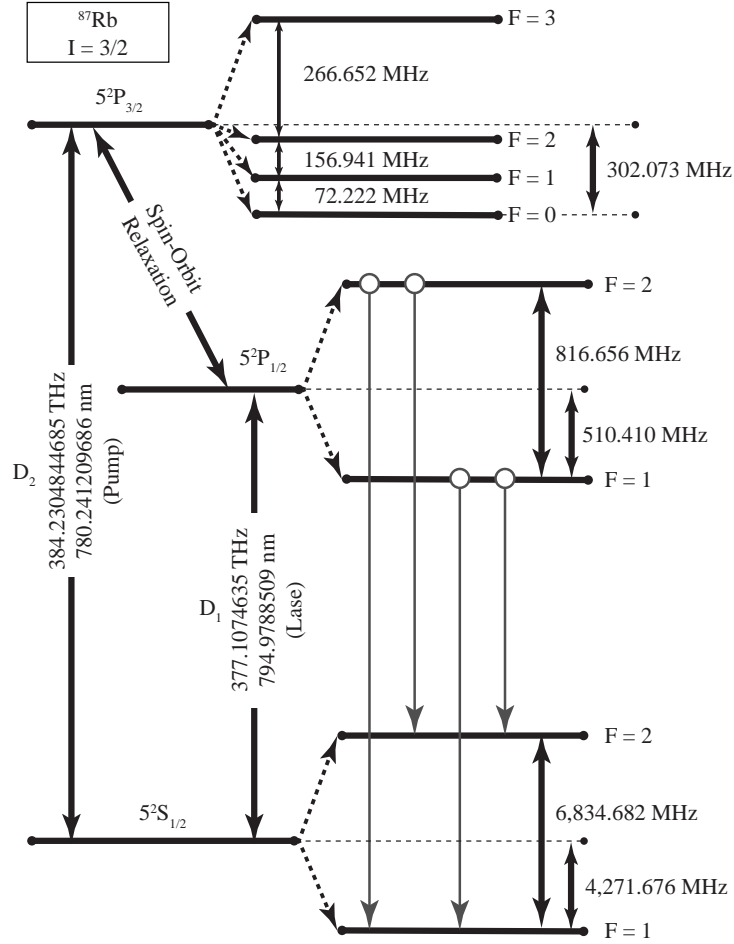
Figure 32. Structure of rubidium (Rb) DPAL operation from pumping the D_2 line near 780.2 nm, with spin-orbit relaxation from the $5^2P_{3/2}$ to the $5^2P_{1/2}$ levels resulting in lasing emission from the D_1 line near 795.0 nm made up of 4 hyperfine lines with moderate spacing.

68

gas. First demonstrated with Rubidium (Rb) [47], DPAL systems offer excellent thermal control, good beam quality, and a quantum efficiency of 95-99%, generating considerable interest within the laser community. [107]

The potassium DPAL lases at the shortest wavelength at 770.1 nm near the O_2 (X-b) transition. [95] The rubidium DPAL has also shown successful implementation [46, 80, 106, 103] and the limitations imposed by atom cycle rates of rubidium have been discussed. [54] The cesium version of the DPAL system has received considerable attention. [28, 96, 94, 98, 63, 99, 100, 102] Recently, a high power flowing system greater than 1 kW with a 48% optical-to-optical efficiency has been reported. [14] Lithium and sodium have a much smaller separation between the D_1 and D_2 lines, making them less feasible to pump by the broad spectral emission of diode stacks.

Interest in the atmospheric transmission characteristics of these alkali lasers led to the development of a tunable diode laser absorption spectroscopy (TDLAS) device for long open-path, >1 km, field deployment. The system was originally designed to study the potassium DPAL that operates in a narrow window between the rotational features of the O_2 X-b (0,0) transition near 760 nm. In the current work we extend the TDLAS systems functionality to the Rb DPAL at wavelengths near 795 nm and review previous work for K [65] and Cs [17]. There are several moderate strength water lines in the vicinity of the Rb and Cs DPAL emission lines and molecular oxygen transition near the K DPAL emission line. [73]

Performance differences in molecular absorption for each DPAL variant for a variety of weapons engagement scenarios are considered. Simulations are validated with open-path TDLAS spectra. The High Energy Laser End-to-End Operational Simulation (HELEEOS) is used to compare the K, Rb, and Cs DPAL systems to the Chemical Oxygen Iodine Laser (COIL). Path integrated absorbance, total system Strehl ratio, and required dwell time are evaluated for long range "air-to-air",

"air-to-ground", "ground-to-air", "low altitude" ocean, and "low power" jamming scenarios.

Simulation of DPAL Transmission

High energy laser simulations like HELEEOS [29], High Energy Laser COnsolidated Modeling and Engagement Simulation (HELCOMES) [48], and HELSEEM (High-Energy Laser System End-to-End Model) [70], treat laser emission using a monochromatic model. The wings of atmospheric lineshapes are usually considered, but only for the final laser wavelength in question. For the present work, the spectral overlap of the absorption lineshapes with the laser small signal gain is used to evaluate the path integrated absorbance. The Line-by-Line Radiative Transfer Model (LBLRTM) [19] was implemented within HELEEOS 3.0 BETA to estimate molecular absorption for a variety of scenarios. LBLRTM can also compute a variety of other effects, like continuum, molecular scattering, aerosol effects, and the like, but for these simulations LBLRTM was compiled and driven with inputs to only consider molecular absorption. Aerosol absorption, aerosol scattering, molecular scattering, and continuum were all computed using HELEEOS routines while LBLRTM was passed inputs on molecular concentration, temperature, and pressure and returned molecular absorption with very high resolution back to HELEEOS. The high resolution molecular absorption profile was then used with the DPAL laser gain profile to determine overall molecular absorption:

$$\mathbf{A} = \frac{\int\limits_0^\infty A(\tilde{\nu})G(\tilde{\nu})d\tilde{\nu}}{\int\limits_0^\infty G(\tilde{\nu})d\tilde{\nu}} \tag{17}$$

where the laser lineshape, $G(\tilde{\nu})$, is integrated over the spectral area where the laser gain profile, typically 10 times the FWHM. The atmospheric path in length ab-

sorbance is defined as,

$$A(\tilde{\nu}) = \sum_i \int \sigma_i(\tilde{v}, P(z), T(z)) \cdot N_i(z)dR \tag{18}$$

where $z(R)$ is the altitude as a fraction of slant range, R. The absorption cross-section, σ_i, for each atmospheric constituent, i, is dependent on frequency, $\tilde{\nu}$, and pressure, P, and temperature, T. The absorption depends on the species specific concentration, N_i, as a function of altitude, z, and path length, R. Overall molecular absorbance, $\mathbf{A}$, is used in HELEEOS as an input to compute thermal blooming. Predicted atmospheric absorbance, and DPAL small signal gain lineshapes with buffer gas pressures of 1 atm, 10 atm, and 20 atm for each DPAL variant are provided in Figs. 33, 34, and 35. A similar spectra for a COIL device is provided in Fig. 36. When calculating molecular absorption, HELEEOS breaks up the slant path into many segments, typically 1,000, where section averages for temperature, pressure, and atmospheric concentration are passed to LBLRTM, which in turn calculates spectral molecular absorbance. Figs. 33, 34, 35, and 36 each represent a single section from the 1,000 segments using the "ground-to-air" scenario described in Table 1. The laser lineshapes are used in conjunction with the LBLRTM $(km)^{-1}$ spectral absorbance for each slant path segment. HELEEOS uses volume absorption coefficient, $\alpha = \Sigma \alpha_i n_i$, at each altitude, z, along the slant path, R.

The K DPAL emission line is hemmed in by the molecular oxygen $X^3\Sigma_g^-$ to $b^1\Sigma_g^+$ (v"=0, v'=0) $^PP(33)$ and $^PQ(33)$ lines on the left and the $^PP(31)$ and $^PQ(31)$ lines on the right in Fig. 33. The four closest lines are assigned with absorbances of 0.04 or greater.

For a narrow line K DPAL, most of the molecular absorption occurs from the hot bands (v"=1, v'=1) of molecular oxygen, each nearly a magnitude less in absorbance than the (v"=0, v'=0) lines.
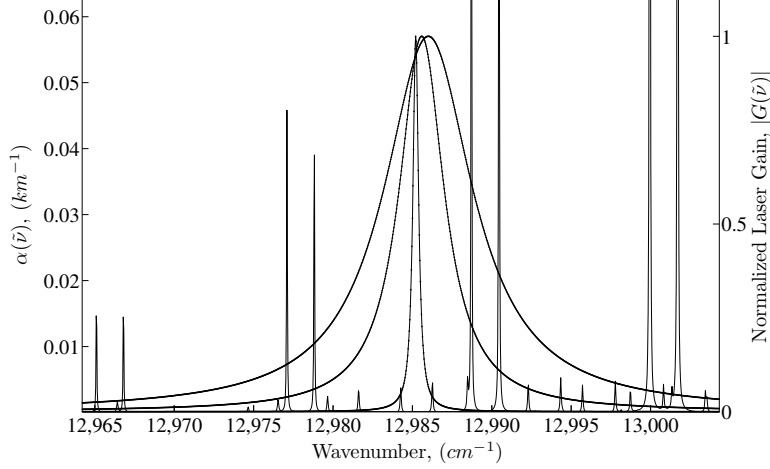
Figure 33. Structure of atmospheric absorption by molecular oxygen near the potassium (K) DPAL D_1 line near 770.1 nm. Also shown is the small signal gain lineshape with buffer gas pressures of 1, 10 and 20 atm.

The Rb DPAL is very different from both the K and Cs variant - different from the K because of water vapor instead of molecular oxygen - and different from the Cs because the Rb has a water vapor line nearly on resonance of its laser emission. All atmospheric absorption lines seen in the spectrum are a result of water vapor, and are assigned using the vibration quantum numbers of the upper level (v_1', v_2', v_3') with the ground vibrational (0,0,0) level common for all the features. Rotational states are labeled with the quantum numbers [J', K'$_A$, K'$_C$]-[J", K"$_A$, K"$_C$] for the upper and lower states, respectively. The water vapor line on resonance of the Rb DPAL is the (0,1,3) [2,1,1]-[2,1,2] seen in Fig. 34.

CO_2 transitions are defined in HITRAN as a linear triatomic with large Fermi resonance using the definition, [v_1', v_2', l_2', v_3',r']- [v_1", v_2", l_2", v_3",r"] ($Branch$, J", $Symmetry$", F"), where v is the quantum number associated with the normal mode of vibration j, and l_j is the vibrational angular momentum quantum number associated with the degenerate bending mode j, and r is the level in the Fermi resonating group. A P-branch of CO_2 runs through the Rb emission line and the CO_2 [1,1,1,5,2]-[0,1,1,0,1] (P,1,4,f) and (P,1,3,e) are on each side of the emission line, which also has

72
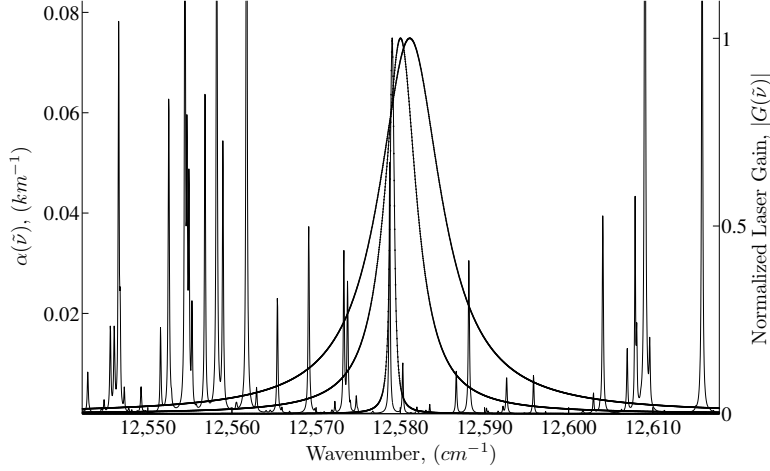
Figure 34. Structure of atmospheric absorption by water vapor near the rubidium (Rb) DPAL D_1 line near 795.0 nm. Also shown is the small signal gain lineshape with buffer gas pressures of 1, 10 and 20 atm.

some OH lines nearby. OH, a diatomic with a doublet-π electronic state, is defined in HITRAN as $[X', i', v_1']$-$[X'', i'', v_1'']$ $(Branch, J'', Symmetry'', F'')$, X being the electronic state, and specifically for OH, the branch definition for the lower-state quanta also accommodates the total orbital angular momentum N as well as J. The OH lines [X,3/2,4]-[X,1/2,0] (OP,7.5,f,f) and (PP,11.5,f,f) also lie on each side of the emission line. The line strengths associated with these CO_2 and OH transitions along with their relatively low natural concentrations result in absorption lines that are very small compared to the water vapor lines nearby.

The atmospheric structure around the Cs is very similar to Rb, dominated by water vapor with only a few OH and CO_2 lines of low line strength and low relative concentration to be seen in Fig. 35.

It is also clearly seen that the water vapor absorbance near the Cs DPAL is higher for the same relative path conditions, but the Cs water vapor lines are on each side, surrounded in even more closely than the K DPAL is by molecular oxygen.

The COIL line seen in Fig. 36 demonstrates the narrowness of the emission line, a result of cooler temperatures and significantly lower operating gain cell pressures
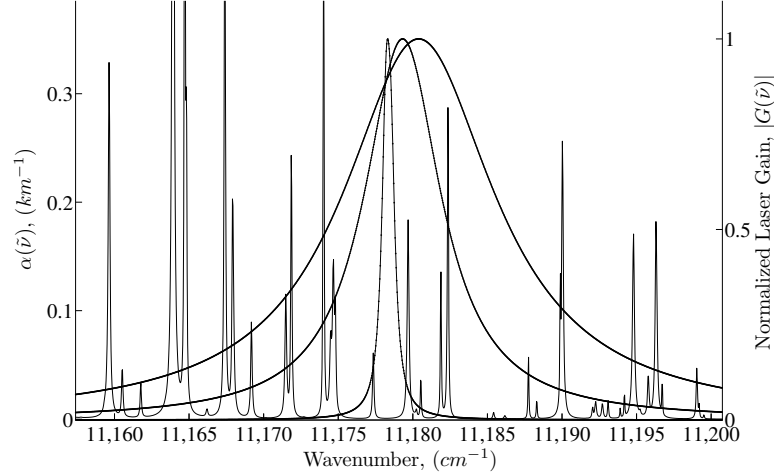
Figure 35. Structure of atmospheric absorption by water vapor near the cesium (Cs) DPAL D_1 line near 894.6 nm. Also shown is the small signal gain lineshape with buffer gas pressures of 1, 10, and 20 atm.

because of the fundamental difference in laser design between a DPAL and COIL. Again, only water vapor lines are seen in the spectrum, but lines do exist in the neighborhood of the COIL emission line from NO, CO_2, and CH_4. The lines do not have the abundance or line strength to contribute to absorption, and are also relatively far away from the narrow emission line with the exception of the CO_2 [4,1,1,1,3]-[0,1,1,0,1] (R,3,3,e) that sits nearly at the center of COIL emission.

Five scenarios were designed to represent typical laser engagements shown in Fig. 37. The Airborne Laser (ABL) was megawatt class chemical oxygen-iodine laser (COIL) on a Boeing 747-400F platform designed for defense against intercontinental ballistic missile (ICBM) attacks by destroying the missile in boost phase. An "air-to-air" scenario to represent a typical ABL engagement has a high overall altitude, very long slant path, and low water content. The Advanced Tactical Laser (ATL) was a COIL device installed on board a C-130 to support special operations. The "air-to-ground" scenario designed to represent it has a moderate slant range propagating from the aircraft at lower altitude to a ground level target. The Tactical High Energy Laser (THEL) was a ground-based laser designed through a joint effort between the United

74
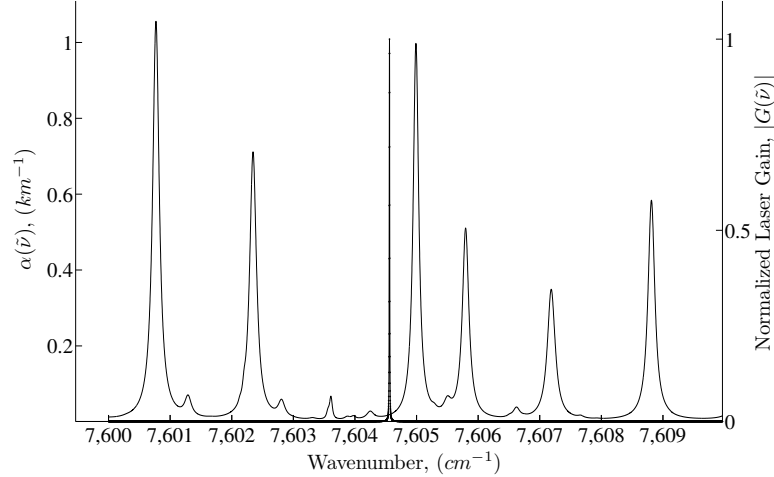
Figure 36. Structure of atmospheric absorption by water vapor near the COIL iodine line near 1.315 μm is shown with a typical emission linewidth, significantly narrower than DPAL emission lines.

States and Israel to defend ground battle spaces against incoming artillery. The "ground-to-air" scenario depicting its use has a slant range propagating from ground level to an airborne target. The Navy has been interested in using lasers for ship defense, and while the higher powers for ship defense have focused on Free Electron Lasers (FEL), there has also been interest in smaller high energy laser to compliment the Phalanx close-in weapon system (CIWS). A "low altitude" scenario having a short path length with very high overall water vapor content was designed to represent this case. Large Aircraft Infrared Countermeasures (LAIRCM) systems such as the AN/AAQ-24(V) are also considered with a low-power laser "jamming" scenario with low aircraft lasing a low-altitude incoming missile. Multiple scenarios share many of the same input parameters and settings to simplify the analysis. Only the "air-to-air" scenario uses adaptive optics. All scenarios are set to use the nearest Extreme and Percentile Environmental Reference Tables (ExPERT) location. [71, 77] The ExPERT database is a compilation of data from 573 ground sites that have collected specific atmospheric information for each location. The final implementation of the database contains information that describes the localized and upper air weather. Generally,

75

the database was designed to describe the weather extremes experienced by each ground site, thus information is stored as a function of percentile humidity, time of day, etc. [77] Critical differences from scenario to scenario are atmospheric constituent content, overall engagement geometry, laser wavelength, laser power, laser spectral lineshape. Table 1 provides the primary differences for each scenario, including the ratio of laser power (LP) to target damage threshold (TDT), if the aero-optic model includes a conformal aperture, and other general scenario settings. A visual overview is included in Fig. 37.

Table 1. HEL Engagement Scenarios

Scenario Name	"air-to-air"	"air-to-ground"	"ground-to-air"	"low altitude"	"jamming"
Start Alt (km)	12	1.5	0.01	0.02	1
End Alt (km)	15	0.001	2.5	0.005	1
Slant Range (km)	100	10	5	5	5
Aerosol Model	Continental Avg.	Urban	Desert	ANAM	Desert
Turbulence Model	HV 5/7	HV 5/7	Climatological	NSLOT	HV 5/7
Approx. Lat	39.03	29.33	31.87	22.95	34.55
Approx. Lon	125.75	47.52	35.22	120.2	69.22
ExPERT Climate Type	Maritime	Desert	Desert	Maritime	Desert
Aero-Optic Model	Conf. Ap.	Conf. Ap.	None	None	Conf. Ap.
Exit Beam Dia. (m)	1.5	0.5	0.7	0.5	0.02
Circular Target Diameter (m)	0.5	0.25	0.25	0.25	0.05
LP/TDT ($cm^2 \cdot s^{-1}$)	200	10	50	50	1

TDLAS Device

The tunable diode laser absorption spectroscopy instrument has been used to validate simulations of atmospheric paths and detailed descriptions of the device configuration and methods for collecting spectra have previously been discussed. [17, 65, 64] The tunable diode lasers compatible are the New Focus Velocity laser series, here models 6312, 6314, and 6318 represent the K, Rb, and Cs, respectively. Model 6324 can be used to represent a COIL laser. Typical output powers are about 10 mW, and each has a 10 - 20 nm tunable range depending on the model, all with less than a 300 kHz linewidth. The laser source can easily be changed to investigate other spectral regions of interest with minimal changes to the overall system. The laser
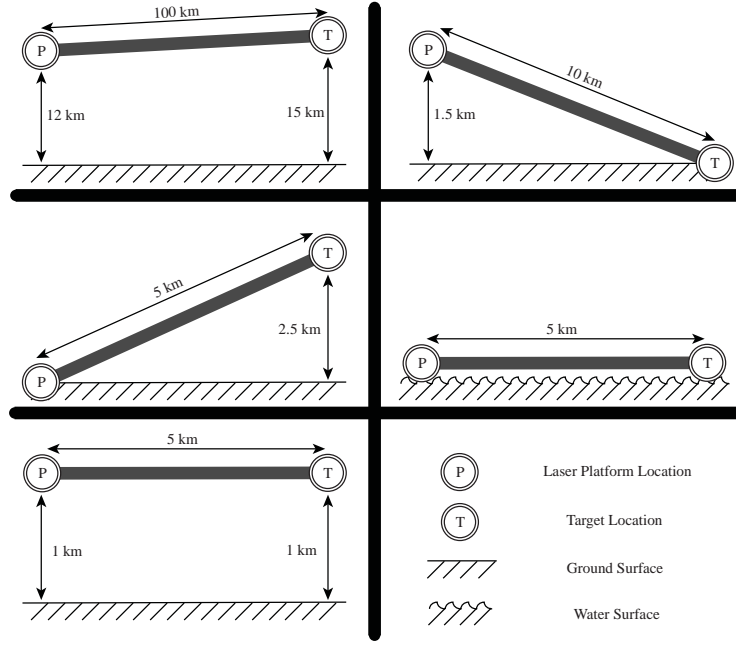
Figure 37. Engagement geometry for a) "air-to-air" b) "air-to-ground" c) "ground-to-air" d) "low altitude" e) "jamming" scenarios.

output is amplitude modulated by a Thor Labs EO-AM-NR-C1 free space modulator at 102 kHz (lock-in maximum useable modulation rate), and the laser is fiber coupled and expanded to nearly fill a military grade 12.5 inch RC Optical RitcheyChretien transmit telescope. The laser can also be split before the fiber in order to include a reference cell, White cell, etc. for more detailed investigations. The expanded laser beam is directed across an open-path and then received by a second identical telescope. Thor Labs PDA100A Si detectors are used to measure the initial and attenuated signals, and are filtered by Stanford Research Systems SR850 dual-phase lock-ins. The dual-phase lock-in signal is recorded by a National Instruments USB-6251 DAQ. 2 m thick Thor Labs pellicle beam splitters are used in the optical chain to minimize etalon effects. The intensity of the reference signal is measured late in the optical train immediately prior to the telescope beam expansion. A High Finesse WSU-2 wavemeter records the frequency axis. The wavemeter is calibrated with a

2 MHz fiber-coupled SIOS SL-03 frequency-stabilized HeNe laser to achieve a better than 10 MHz accuracy. All hardware in the TDLAS device is controlled by a PC using MATLAB®. Calibration of the frequency axis, baseline removal, and further spectral processing have also been reported. [17, 65, 64] Baseline curvatures have a typical 0.2 magnitude in absorbance and are removed with quadratic fits. The baseline removal process obfuscates any wavelength dependent scattering, which simulations suggest change by 0.003 in absorbance over the tunable range of these lasers for a 1 km boundary layer path. In this configuration, the maximum open-path distance is limited by the Quickset QPT-130 ruggedized pan and tilt mounts used and is about 2 km.

Collections were performed over a short 150 m open-path during fair weather conditions. The send and receive telescopes were placed 1 meter above the ground and separated by 1 meter, each viewing a 6 inch flat mirror at the far end of the path being investigated. All collections were performed at night reducing the effects of turbulence during collection. Weather data was collected by a NIST-certified Davis Vantage Pro2 weather sensor placed near the turning mirror.

Results

A best estimate for the atmospheric temperature, pressure, and molecular oxygen (K) or water vapor (Rb and Cs) concentration were obtained using the Line-by-Line Radiative Transfer Model (LBLRTM) [19], which in turn uses the HITRAN database [72]. By knowing the open-path distance, a non-linear least squares fitting process was used by simulating an atmospheric spectra defined for a homogenous atmosphere with a single temperature, pressure, and water vapor concentration as fit parameters. This process has been described in more detail. [17] For each collection, a low pressure (no buffer gas) alkali vapor cell inside a heater block was placed in the path between the

receive telescope and signal detector to provide a reference for the DPAL wavelength being investigated. The spectra are illustrated in Figs. 38 - 40. The strong, narrow absorption features near from the D_1 $^2P_{1/2}$ - $^2S_{1/2}$ transition in potassium, rubidium, and cesium are clearly seen near 12,985.19 cm^{-1}, 12,578.95 cm^{-1}, 11,178.27 cm^{-1}, respectively, and are excluded from the NLLS fitting model. The hyperfine structure of the D_1 transition is easily resolved at low pressures for rubidium and cesium, but the potassium hyperfine lines are spaced more closely than their Doppler widths. For each spectrum, a cubic baseline was removed before the fitting process using only data points that lie outside of the hyperfine lines and the molecular oxygen or water vapor lines present in the spectrum. The iterative fitting process includes a 95% confidence interval for each fitted parameter (temperature, pressure, and concentration) based on results from each of the iterative fits, giving the final estimates for the average path temperature, pressure, and constituent concentration.

Fig. 38a shows the fit quality for a 150 m path with residuals in Fig. 38b in the neighborhood of potassium, resulting in an estimated temperature of 15.5 C (272.5 ± 3 K), a pressure of 829.1 ± 1 hPa, and a molecular oxygen concentration of 7.011 ± 0.05 × 10^{18} molecules per cm^3. During the experiment, the weather station data indicates variations during the test of 3.5 K in temperature, 10 percentage points in relative humidity, and 0.6 hPa in station pressure. The agreement between the fit and meteorology data is poorer than the statistical error from the spectral fitting. Considering the variation of weather parameters during the experiment combined with the relatively low signal-to-noise ratio over the higher rotational lines, the large confidence bounds from fit parameters is not surprising. Fitting to the entire P-branch would yield more accurate results, as would including the R-branch, but would require significantly longer collection times. [19] During the collection, an object passed through the open path collection and is seen near 12,995.67 cm^{-1} and should not be
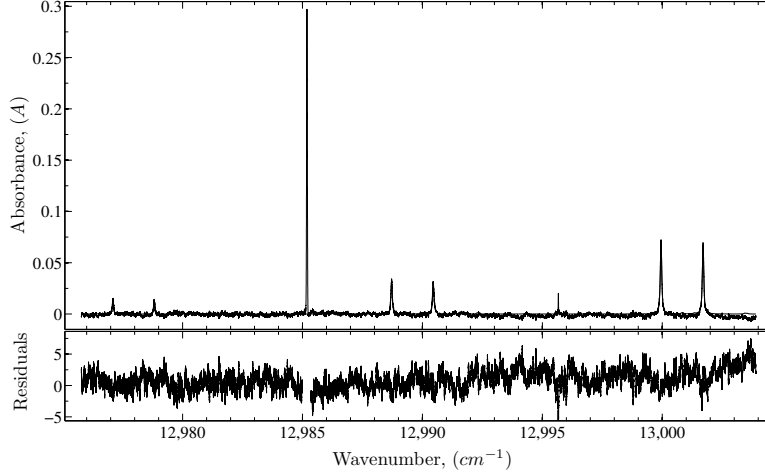
Figure 38. TDLAS data collected near the K DPAL emission line a) over a 150 m path with NLLS fit and b) residuals.

attributed to a spectroscopic function.

Fig. 39a similarly demonstrates the NLLS fit for the 150 meter path with residuals in Fig. 39b near the rubidium emission line resulting in an estimated temperature of 27.8 C (301.0 ± 10.8 K), a pressure of 815.5 ± 33.4 hPa, and a water vapor concentration of 4.2141 ± 0.013 × 10^{17} molecules per cm^3. This 150 m outdoor path was collected at night using two weather stations at the east side of the path, and using the temporal average of data from both instruments for the time of collection the temperature was 21.5 C (294.65 K), 78.3 % relative humidity, and 985.6 hPa. The agreement between the fit and meteorology data is poorer than the statistical error from the spectral fitting, just as with the potassium case. However, absorbance of the water lines nearby rubidium are nearly an order of magnitude smaller than those near the cesium DPAL emission lines, as can be seen in the fit. As expected fitting to smaller absorption lines result in poorer fitting statistics, and demonstrate the lower overall molecular absorbance near the Rb DPAL.

Fig. 40a illustrates the fit quality for the 150 meter path with residuals in Fig. 40b resulting in an estimated temperature of 15.5 C (288.6 ± 0.15 K), a pressure of
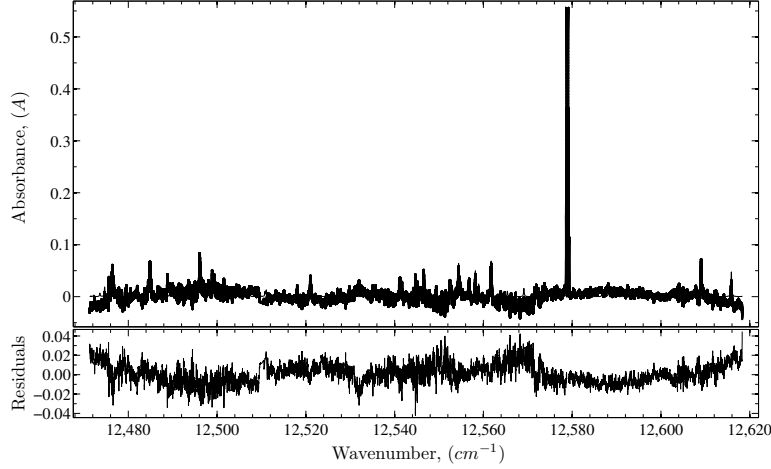
Figure 39. TDLAS data collected near the Rb DPAL emission line a) over a 150 m path with NLLS fit and b) residuals.

993.8 $\pm$ 0.9 hPa, and a water vapor concentration of 3.096 $\pm$ 0.004 x 10^{17} molecules per cm^3. Weather conditions during the experiment collection were fairly constant, varying less than 1 degree K, less than 4 percentage points in relative humidity, and less than 0.4 hPa in pressure. The agreement between the measurement and the meteorology data is poorer than the statistical error from the spectral fitting and but fitted temperature still agrees with meteorological temperature to within 2.1%, excellent agreement.

A typical simulated absorption spectrum for a 1 km atmospheric path used to calculate integrated absorption coefficient for a Cs DPAL is shown in Fig. 41a along with the product of the small signal gain and absorption coefficient before integration in Fig. 41b.

Using Eq. (17) the final integrated absorption of each laser type for each scenario is summarized in Fig. 42.

The "air-to-air" scenario of in Fig. 42a demonstrates the disadvantage a K DPAL for over extreme path lengths. Only by making a K DPAL with a narrow emission line results in molecular absorbance that rivals the Rb variant with similar gain cell

81
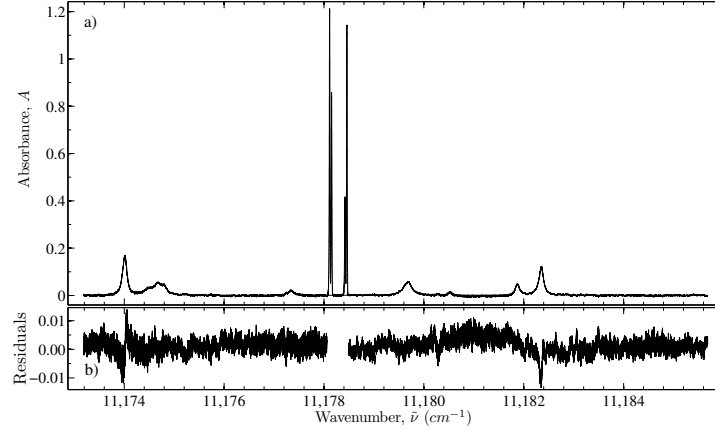
Figure 40. **TDLAS data collected near the Cs DPAL emission line a) over a 150 m path with NLLS fit and b) residuals.**
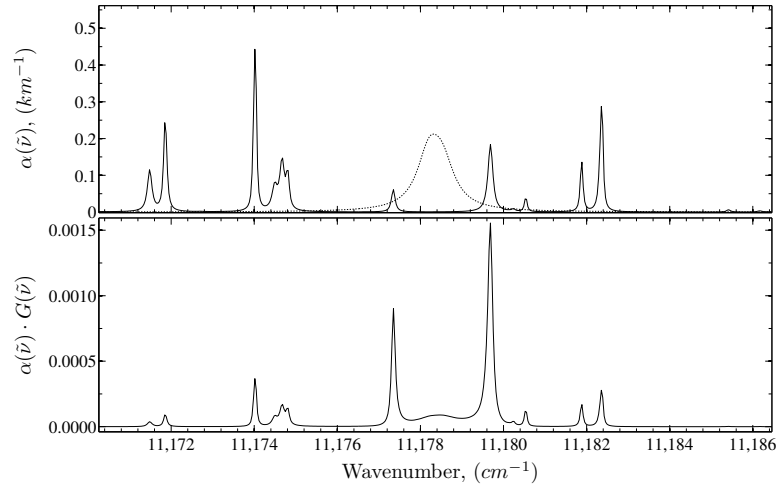
Figure 41. Product of laser line shape with atmospheric absorbance.
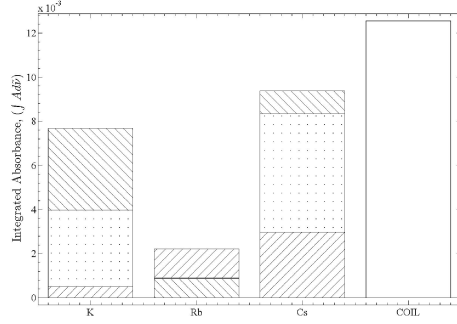
(a)
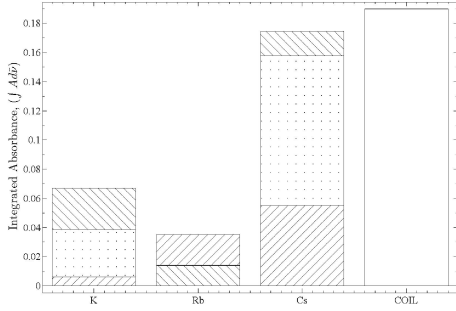
(b)
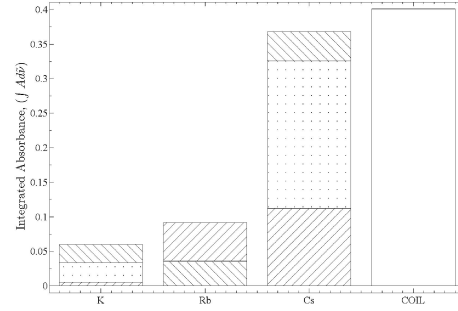
(c)
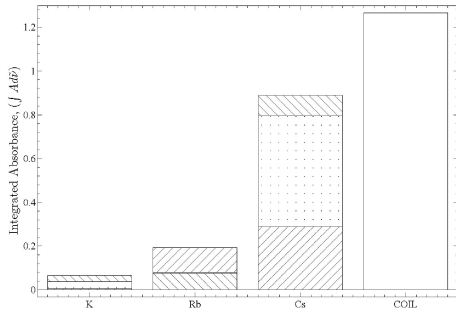
(d)
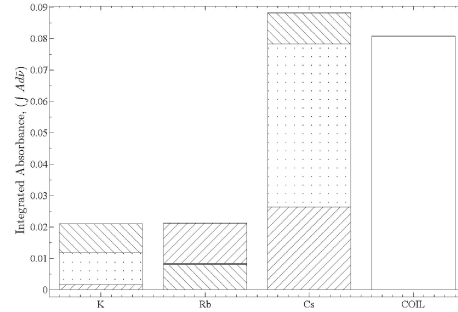
(e)

Figure 42. Integrated absorbance for a) "air-to-air" b) "air-to-ground" c) "ground-to-air" d) "low altitude" e) "jamming" scenarios for DPAL lasers with gain cells containing buffer gasses at 1 atm (slant right), 10 atm (dotted), and 20 atm (slant left) of pressure, all compared to a COIL laser (white).

pressure. Each flavor of DPAL performs better than COIL in regards to molecular absorption, with the exception of a 20 atm K and Cs getting close to the COIL molecular absorption value, K because of its long path length and Cs because of the stronger water lines nearby. Surprisingly, the Rb DPAL benefits from the higher buffer gas pressures because the water vapor absorption line that lies nearly on top of the Rb D_1 line - while the K and Cs DPALs are hemmed in by their respective absorption features. The Rb escapes absorption by spreading its power over a broader spectral area. Fig. 42b shows the results from a "air-to-ground" scenario, demonstrating how a shorter path begins to favor the K variant, putting its performance on par with the Rb because of lower molecular oxygen in the overall path. For this case, both the Cs and COIL lasers have about the same molecular absorption for higher Cs gain cell pressures. Fig. 42c shows how a "ground-to-air" scenario also gives similar results when comparing a highly pressure-broadened Cs DPAL to a COIL device while the K and Rb DPAL performances are similar. Given that its path length is twice as long, it is no surprise the molecular absorption is approximately twice that of the "air-to-ground". The over-water "low altitude" scenario in Fig. 42d demonstrates the advantage a K DPAL would have over these shorter paths with very high water vapor while the Rb and Cs DPALs and COIL are all affected by the water vapor content near the sea surface. Finally, Fig. 42e shows similar trend for the scenario describing laser jamming of IR seeking missiles. The worst case K and Rb DPAL configurations perform similarly to the best case Cs configuration. A worst case Cs experiences similar molecular absorption as the COIL, a trend shared in all plots.

Molecular absorption is not the only metric of interest, and all inputs and outputs from HELEEOS are available to compare overall laser performance. Scattering at shorter wavelengths starting in the visible regime and shorter by air molecules can be significant. The scattering cross-section of air molecules is approximately pro-

portional to the Rayleigh regime, of which a COIL device lies at the border of, or arguably beyond. While scattering reduces fluence on target, it also reduces thermal blooming, a trade off which is computed in HELEEOS simulations. Thus, extinction due to scattering can be nearly 8 times greater for a K DPAL compared to a COIL device. For example, the "air-to-air" scenario calculated total aerosol and molecular scattering cross section to be 0.47, 0.41, 0.26, and 0.06 for K, Rb, Cs, and COIL respectively. Losses due to diffraction have the opposite effect, with the diffraction-limited beam diameter on target approximately proportional to wavelength, giving a smaller minimum focusable spot size for a DPAL laser and increasing irradiance. For example, the "air-to-ground" scenario has a diffraction limited beam width of 0.019, 0.021, 0.024, and 0.034 for K, Rb, Cs, and COIL respectively. Strehl ratio, a numerical value ranging from zero to one, represents many effects that increase the effective spot size, and reduces the peak at beam center to a lower value than the peak for the diffraction limited case. Strehl ratio, S, is defined here as the ratio of transmitted to diffraction-limited irradiance, I, at beam center,

$$S = \frac{I(x = 0, y = 0)}{I_D(x = 0, y = 0)} \tag{19}$$

If the Strehl ratio is unity, the system performance is considered "diffraction limited". As beams are spread by atmospheric effects like turbulence and thermal blooming, the Strehl ratio is lowered as the irradiance of the beam is spread outward. Fig. 43 demonstrates Strehl ratio for the various DPAL variants and scenarios Fig. 42.

Just as with molecular absorption, performance of Strehl ratios for Rb DPAL gain cell buffer gas pressures are typically inverted compared to K and Cs, except for the low power "jamming" scenario where all DPAL cases are very close to identical. Overall, it is also seen that molecular absorption has an effect on overall strehls, with a typical Strehl ratio difference from the minimum pressure to the maximum pressure
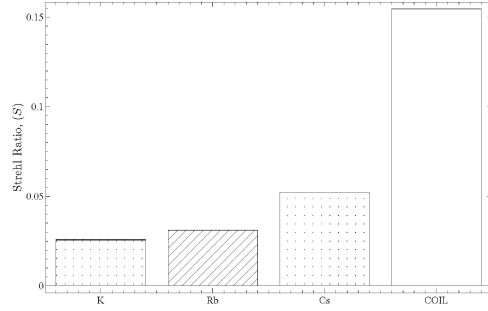
(a)
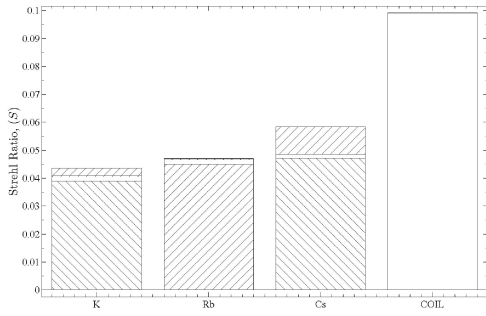
(b)
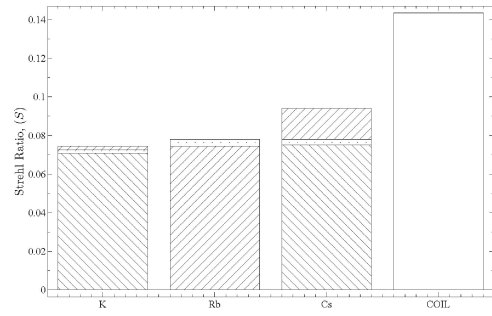
(c)
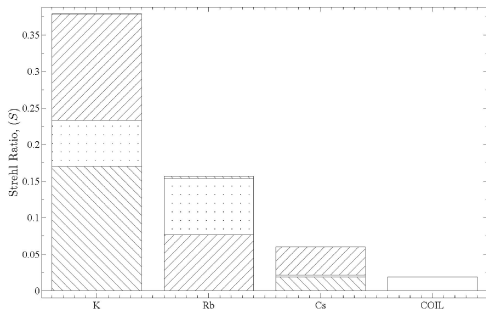
(d)
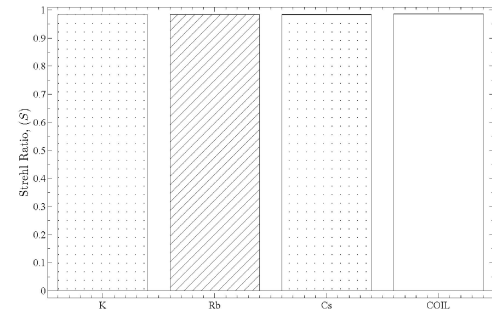
(e)

Figure 43. Strehl ratios for a) "air-to-air" b) "air-to-ground" c) "ground-to-air" d) "low altitude" e) "jamming" scenarios for DPAL lasers with gain cells containing buffer gasses at 1 atm (slant right), 10 atm (dotted), and 20 atm (slant left) of pressure, all compared to a COIL laser (white).

of about 15%, 12%, and 22% for K, Rb, and Cs respectively, further demonstrating how the Cs DPAL is more dependent on gain cell pressure than K or Rb. Interestingly, beam spread is greater for all DPALs than for COIL, giving COIL the highest overall Strehl ratio in nearly every case with the exception of the water-rich "low altitude" case over the water. Separating the results for overall Strehl ratio for each individual run into components cause is difficult because of the internal design of HELEEOS and its dependence on the High energy laser And Relay Engagements (SHaRE), an internal toolkit provided by MZA Associates.

Dwell time, D_T, was calculated using a 90% confidence in the probability of kill and using target damage thresholds 20% of the overall target damage threshold. As expected, dwell time is inversely related to beam Strehl ratio, with very high Strehl ratios exhibiting the lowest dwell times. The "air-to-air" scenario resulted in dwell times with little difference resulting from molecular absorption for different DPAL gain cell pressures, and with COIL performing best over very long paths from its superior molecular scattering performance, and coupled with low absorption from high altitudes and low pressures, there is little thermal blooming in this scenario. The "air-to-ground" and "ground-to-air" had similar trends, with K and Rb performing similarly for their best case pressures, and COIL having the longest required dwell time. The "low altitude" scenario demonstrated a high dependence on DPAL gain cell pressures for Rb and Cs, with K easily outperforming all other devices, a likely result given the high water vapor content over water.

For reference, a plot of diffraction-limited spot area compared to scattering cross-section and turbulence relative variance, each normalized to one, is shown in Fig. 45. Higher relative values indicate poorer beam quality on target. The area of the diffraction-limited beam size is proportional to λ^2, while scattering cross-section is proportional to λ^{-4}, and turbulence is proportional to $\lambda^{-7/6}$, with scattering having
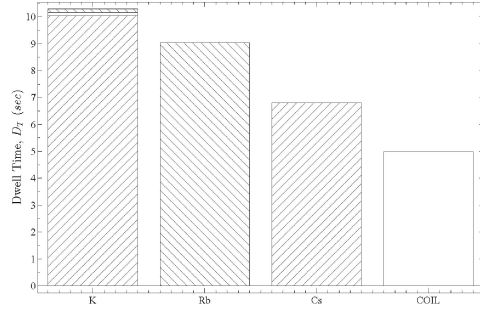
(a)
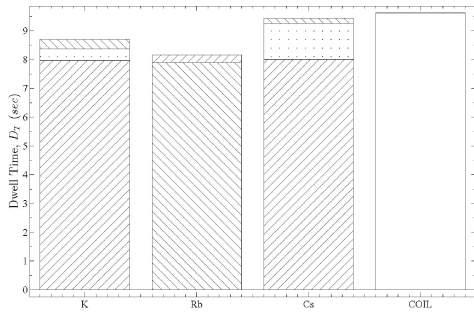
(b)
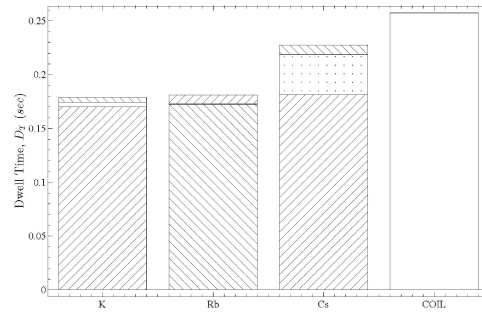
(c)
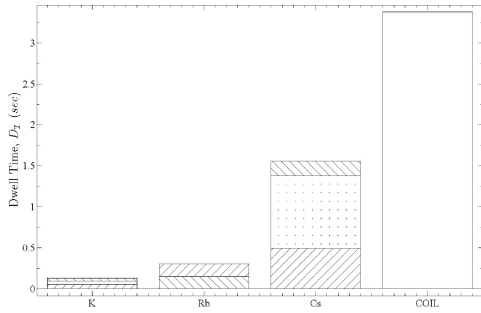
(d)
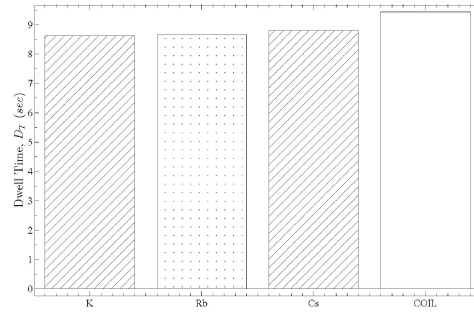
(e)

Figure 44. **Dwell time for a) "air-to-air" b) "air-to-ground" c) "ground-to-air" d) "low altitude" e) "jamming" scenarios for DPAL lasers with gain cells containing buffer gasses at 1 atm (slant right), 10 atm (dotted), and 20 atm (slant left) of pressure, all compared to a COIL laser (white).**
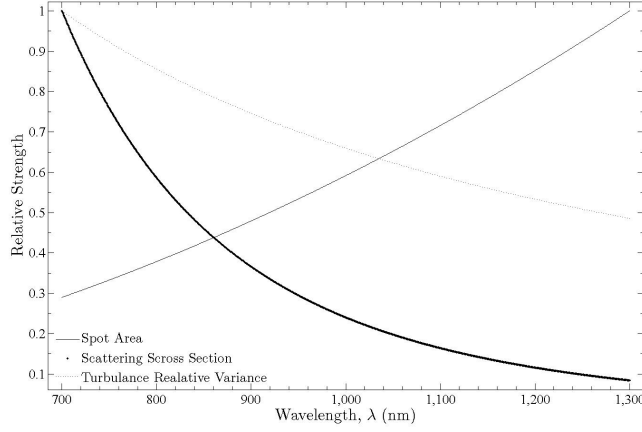
Figure 45. Diffraction Limited Spot Area (-), scattering cross-section (:), and turbulence relative variance (- -), each normalized to one to showing each effect's spectral dependence.

the largest relative change in overall effect over the wavelength range because of its λ^{-4} dependence. Because of scattering's strong degradation of shorter wavelength beams, laser devices with shorter wavelengths will be greatly affected by scattering over long slant ranges, a trend seen in Fig. 44a.

With Rb, Cs, and COIL devices being dependent on water vapor concentration, the distribution of relative humidity recordings at each site using data from the nearest ExPERT site was used to set relative humidity for a one-percentile day, a fiftieth-percentile day, and for a ninety-ninth-percentile day, where relative humidity on a one-percentile day would be very low, for a fiftieth-percentile day would have median humidity found at the site used, and for a ninety-ninth-percentile day would exhibit very high relative humidity. The same series of simulations for the five scenarios discussed above were carried out with a 10 atm gain cell for each DPAL and the typical COIL low pressure gain cell. As expected, molecular absorption for the "air-to-air" case is nearly identical for each percentile relative humidity due to the low water vapor content and minimal broadening of those lines at high altitudes. A close look at the "ground-to-air" case reveals the dependence Rb, Cs, and COIL devices have

(a)

(b)   (c)
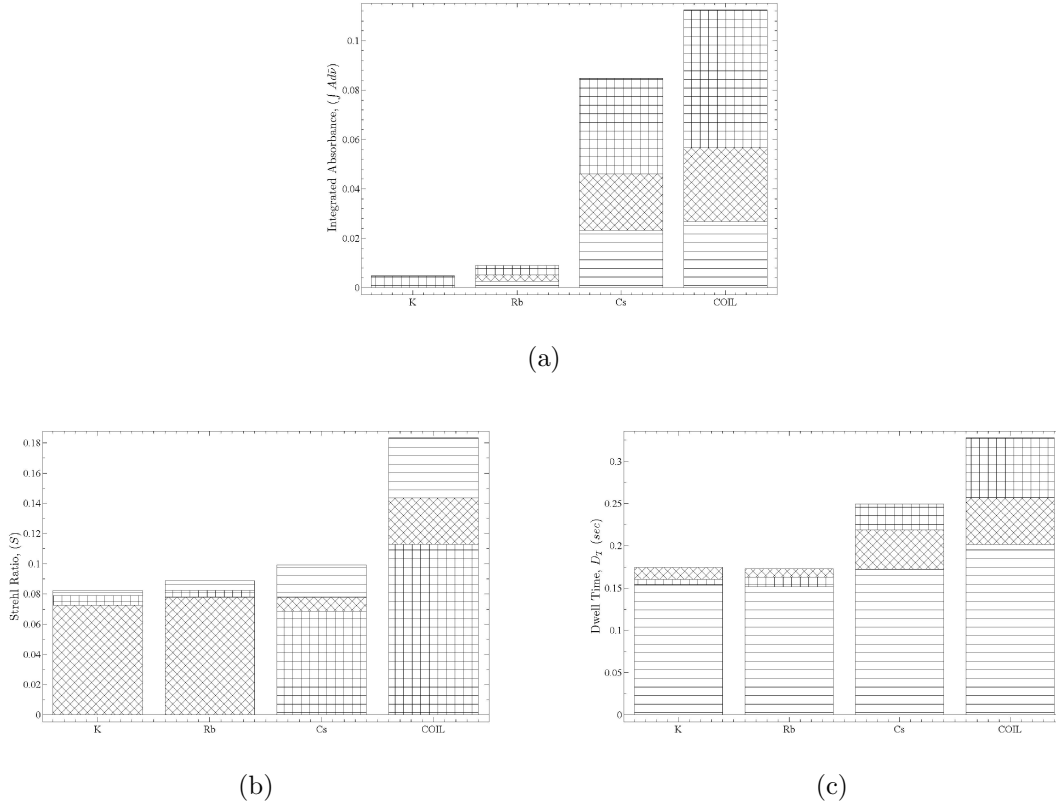
Figure 46. Variation in percentile relative humidity for a) integrated absorbance, b) strehl ratio, and c) dwell time for the "ground-to-air" scenarios for DPAL a laser with a 10 atm gain cell buffer gas pressure each with a 1% (horizontal lines), a 50% (slanted left-slanted right), and a 99% (horizontal-vertical) percentile relative humidity days.

on water vapor content. Fig. 46a demonstrated the vast differences in molecular absorbance from a one-percentile to a ninety-ninth-percentile relative humidity day, where all water dependent devices show the change in integrated molecular absorption as relative humidity increases. For example, the COIL device has over 5 times higher molecular absorbance for the "ground-to-air" between the one-percentile to a ninety-ninth-percentile relative humidity day. This higher overall molecular absorbance contributes to overall beam Strehl ratio, seen in Fig. 46b, where the COIL still has the best Strehl ratio performance. Overall performance for dwell times in Fig. 46c demonstrates how very high water content adds nearly 50% more dwell time to heavily water dependent devices. As expected, the K and Rb DPAL devices are

90

not as susceptible to seasonal and daily changes in relative humidity, and can been seen in this example in variation of relative humidity for the "ground-to-air" scenario.

Conclusions

The TDLAS system is shown to collect information for molecular absorption over atmospheric paths accurately estimating atmospheric content validating atmospheric models. K DPAL atmospheric transmission will be excellent over atmospheres with high water vapor and shorter path lengths with lower laser linewidths. Rb DPAL atmospheric transmission will be excellent over atmospheres with lower water vapor concentrations and will perform relatively better than the Cs DPAL variant. Rb DPAL lasers will benefit from broader laser linewidths by spreading laser emission away from the water line located near resonance. Cs DPAL atmospheric transmission will be the poorest compared to Rb and K variants, and performs best with very little water vapor. Cs DPALs will benefit from lower pressure gain cell configurations over hydrated atmospheric paths. All DPAL systems suffer from higher molecular scattering compared to COIL devices, and DPAL Strehl ratios, and their associated dwell times are less desirable than those from equivalent power COIL devices. Seasonal distribution of relative humidity can result in dwell times 50% longer for Cs DPAL and COIL devices while having little effect on K and Rb DPALs and little effect on all systems at high altitudes. Performance will depend strongly on details of the laser lineshape.

VII. Conclusion

A Tunable Diode Laser Absorption Spectroscopy (TDLAS) apparatus has been designed, built, characterized, and deployed for High Energy Laser (HEL) weapons applications. Long, open-path atmospheric characterization with path lengths exceeding 1 km are studied and documented. The prior state-of-the art limited path lengths to 150 m. The instrument has been ruggedized and deployed in the field, operating at temperatures of -9 C to 25 C. A total 17 indoor and outdoor campaigns were executed collecting a total of 43 sets of data totaling over 500 scans of the potassium, rubidium, and cesium D_1 emission wavelengths. The TDLAS system is being prepared for deployment to DoD HEL test ranges, including the October 2012 test scheduled at the Naval Surface Warfare Center (NSWC) directed energy test facility in Dahlgren, VA.

The high spectral resolution (300 kHz) applied over the broad spectral coverage (over 6 THz) of the instrument, and multiple wavelength regions diode laser wavelengths allow for detection of more than 72 O_2 spectral lines and over 100 H_2O lines. High sampling rates yield over a million samples over the full tunable diode range, 1,500 samples per Doppler limited lineshape, and 15,000 per atmospheric broadened linshape enabling robust Voigt profile characterization and extraction of both temperature and pressure. Absolute wavelength accuracy of 10 MHz was achieved using a wavemeter limited by a stabilized HeNe calibration source and was validated by both alkali frequency standards and by pressure shifted and broadened atmospheric lines from the HITRAN database.

The minimum detectable peak absorbance in a laboratory environment is 0.01. System jitter and atmospheric turbulence introduce additional noise for field deployments, yielding a detectable absorbance of 0.015 over a 150 m paths and 0.04 over 1 km paths. Most collections took place at times of the day when turbulence is

low, pointing to telescope jitter as the dominant source of noise. Even for the very weak O_2 $X^3\Sigma_g^-$ to $b^1\Sigma_g^+$ magnetic dipole transitions, the signal-to-noise ratio under field conditions exceeds 1,000 with a peak signal of 2.51 in absorbance with a 0.0025 noise standard deviation. The 12 inch diameter collimated beam transmitted over 1 km maintains excellent collimation, and at over 4 km distances maintains an 12 inch diameter but because of platform jitter and turbulence the overall beam center moves up two 2 inches from its center over 1 km paths making 4 km paths impossible without larger turning optics.

The instrument is supported by instrument control software based in MATLAB® using the Instrument Control Toolbox and the Data Acquisition Toolbox, as well as manufacturer-supplied shared libraries customized for use with the TDLAS apparatus. Conversion of observed signals to calibrated absorbance as function of calibrated wavelength is also achieved by post-processing methods also written and implemented in MATLAB®, and spectral interpretation to yield atmospheric temperatures, pressures and species concentrations were based on spectroscopic methods and non-linear least-squares fitting methods using the Line-by-Line Radiative Transfer Model (LBLRTM). The new TDLAS instrument represents a significant advance of existing instrument, investigating broad spectral areas at ultra-high spectral resolution over long outdoor paths.

The O_2 $X^3\Sigma_g^-$ to $b^1\Sigma_g^+$ (0,0) rotational spectrum in the vicinity of 762 nm has been characterized by the TDLAS instrument. Temperature was determined to within 0.7%, concentration to 0.8%, and atmospheric pressure to less than 4%. The TDLAS spectra agree with the meteorological data for temperature to within 1.3%, for concentration to within 1.6%, and to atmospheric pressure within less than 10%. Hot bands can be observed over 3 km path lengths in multi-pass cells. Broad spectral band width allows for up to 72 rotational features to be observed in a single unified scan and

direct observation of Boltzman statistical distribution to extract the J dependence of pressure broadening rates observed from Voigt lineshapes. The results suggest a possible improvement to HITRAN database as the field data agrees more closely with Pope's [62] results. Validation of Monocular Passive Ranging (MPR) using Fourier Transform Interferometer (FTIR) device was achieved, demonstrating that the FTIR has a variance in measured absorbance 5 times greater than the TDLAS device measurement. Spectral observations are more sensitive to the state of atmosphere than most modest weather stations predict. Observed baseline changes slowly over tuned wavelength but can be up to 10% of the maximum signal observed and attributing any spectral dependence of the scattering is problematic. Total scattering extinction measurements may require off-axis methods.

Atmospheric absorbance for all three DPAL variants was characterized in the field with path lengths up to 1 km. A high spectral resolution is required for the characterization of HEL propagation due to the narrow linewidths of laser emission, making techniques like FTIR with lower 0.25 cm^{-1} resolution inadequate. Transmission spectra were recorded with atmospheric features co-registered with low pressure alkali cells, yielding wavelength calibration to within 10 MHz, and nearly 2 MHz in close spectral proximity to alkali features. Field data was interpreted to validate LBLRTM simulations using the HITRAN database. With improved atmospheric constituent estimates, no significant variation between simulations and observations can be observed within the statistical limits of the instrument. However, improved meteorological estimates for the state of atmosphere are required to adequately simulate slant paths, and the need for high fidelity weather instrumentation is apparent. The O_2 $X^3\Sigma_g^-$ to $b^1\Sigma_g^+$ is critical to the potassium DPAL, especially the ^PP (31,33) and ^PQ (31,33) features and nearly hot bands. Water vapor is important to both the rubidium and cesium DPALs, with cesium having water vapor lines nearly an order

of magnitude greater than those near rubidium DPAL emission. Water vapor was used to measure temperature, pressure and concentration to within 2.4% or less from 150 m path collections and 3.7% for 1 km path collections when compared to meteorological data. OH and CO_2 lines are scattered near DPAL emission lines, however the atmospheric abundance of these species are so low absorption lines do not impact DPAL atmospheric transmission. Potassium DPAL devices will be insensitive to changes in relative humidity, and rubidium and cesium DPALs will have the least molecular absorption at high altitude and dry slant paths.

The impact of atmospheric transmission on High Energy Laser weapon performance for the emerging DPAL systems was assessed. LBLRTM was integrated into the High Energy Laser End-to-End Operational Simulation (HELEEOS) to compute molecular absorption and five scenarios were considered in this broad application study: a 100 km slant path at high altitude "air-to-air", a 10 km "air-to-ground" slant path, a 5 km "ground-to-air" slant path, an over-ocean "low altitude" slant path, and a low power "jamming" scenario. When considering only molecular absorption, the potassium and rubidium DPALs seems to be the clear winners, however when considering the system engineering metric strehl ratio, the differences between DPAL variants are less exaggerated, with the only clear scenario-specific standout being potassium for very well hydrated slant paths. The warfighter metric, dwell time, also highlights the advantage of a laser system that operates independently of water vapor absorption. It also clearly demonstrates the disadvantage shorter wavelengths have in scattering compared to existing technologies like the Chemical Oxygen Iodine Laser (COIL), making a cesium DPAL an excellent choice for the dry and long path in a high altitude "air-to-air" engagement.

Recommendations

As DPAL systems become more mature, additional opportunities will be available. Using higher source laser powers could be used to study side scattering, and with careful experiment geometry the angular dependence of scattering could also be studied. Performing experiments in heavy aerosol environments will also improve chances of viewing and quantifying side scatter and could be validated with particle counters and a temporal variation. Additional validation could be achieved by collecting information about the size distribution of scatterers. Specialized balanced and calibrated photo detectors could reduce baseline variation in a single scan. Variations in noise baseline could also be captured using shorter lock-in time constants on the order of 10 msec. Collecting turbulence data over the same path simultaneously using the TDLAS system and an off the shelf turbulence measurement device like the BLS900 may demonstrate the capability.

The maximum effective open-path length the of the TDLAS system could be extended by upgrading telescope mounts, altering the optical system design, and increasing laser power. Signal-to-noise ratio could be improved by increasing noise suppression with faster modulation frequency and dynamic range could be improved with upgraded lock-ins operating at significantly higher modulation frequencies. Whole-system reliability and ease of use could be improved by transitioning all optical elements in the optical board to fiber coupled devices and enclosing sensitive devices in thermally controlled enclosures. Large hollow retro-reflective arrays could be used to eliminate the receive telescope and make the alignment process significantly easier, but may exhibit etelon effects.

Improvements to customized hardware control could be implemented increasing the probability of successful data collection. Closed absorption cells could be included during collections to improve signal-to-noise for detailed studies of very small

absorption features. Different modulation techniques could be used to track single absorption features over long time periods to characterize temporal variation along paths. The TDLAS system could be deployed in a variety of different atmospheric environments or place in geometries similar to those where a DPAL may be deployed. Stable and unstable DPAL resonators could be simulated and experimentally tested to determine possible emission lineshapes which could then be applied to make atmospheric transmission estimates.

The device could also be used to monitor species not investigated here, like CO_2, OH, and virtually any species within the range of tunable diode lasers available.

Comparisons between LBLRTM and the Laser Environmental Effects Definition and Reference (LEEDR), and LEEDR can be used to upgrade internal HELEEOS molecular absorption calculations. More detailed HELEEOS studies can be carried out, including different scenarios, comparisons to other modern HEL systems, and more studies of the effects diurnal and seasonal variations have on DPAL propagation.

Appendix A. Physical Constants

Table 2. Physical constants[†]

Symbol	Description	Value/Units
α_{fs}	Fine-structure constant	$1/137.035\,999\,679(94)$
c	Speed of light in vacuum	$299\,792\,458\,\mathrm{m\,s^{-1}}$
h	Planck constant	$6.626\,068\,96(33) \times 10^{-34}\,\mathrm{J\,s}$
		$4.135\,667\,33(10) \times 10^{-15}\,\mathrm{eV\,s}$
$\hbar$	Planck constant $/\ 2\pi$	$1.054\,571\,628(53) \times 10^{-34}\,\mathrm{J\,s}$
		$6.582\,118\,99(16) \times 10^{-16}\,\mathrm{eV\,s}$
k_B	Boltzmann constant	$1.380\,650\,4(24) \times 10^{-23}\,\mathrm{J\,K^{-1}}$
		$8.617\,343(15) \times 10^{-5}\,\mathrm{eV\,K^{-1}}$
ϵ_0	Permittivity (Electric constant)	$8.854\,187\,817 \times 10^{-12}\,\mathrm{F\,m^{-1}}$
μ_0	Permeability (Magnetic constant)	$12.566\,370\,614 \times 10^{-7}\,\mathrm{N\,A^{-2}}$
e	Elementary charge	$1.602\,176\,487(40) \times 10^{-19}\,\mathrm{C}$
m_e	Electron mass	$9.109\,382\,15(45) \times 10^{-31}\,\mathrm{kg}$
m_p	Proton mass	$1.672\,621\,637(83) \times 10^{-27}\,\mathrm{kg}$
m_u	Atomic mass constant	$1.660\,538\,782(83) \times 10^{-27}\,\mathrm{kg}$
P_{atm}	Standard atmosphere	$101\,325\,\mathrm{Pa} = 760\,\mathrm{Torr}$

[†] NIST 2006 CODATA recommended values

Appendix B.   Alkali Data

Potassium Properties

Table 3. Potassium (K) physical properties

Property	Symbol	Value
Atomic number[†]	Z	19
Total nucleons[†]	$Z + N$	58
Ground state[†]	—	$4s^2 S_{1/2}$
Relative natural abundance[†]	$\eta(^{39}K)$	93.2581(44)%
Atomic mass[†]	m	39.0983 u
Melting point[†]	T_m	63.38 °C
Boiling point[†]	T_b	759 °C
Density (solid)[‡]	ρ	856 kg m^{-3}
Nuclear spin[†]	I	3/2
Magnetic moment	μ	+0.391 465 8
Ionization energy[†]	E_I	4.340 663 45 eV

[†] Steck, Daniel A. "Rubidium 87 D Line Data." 2001

Table 4. Potassium D_1 ($4^2\mathbf{S}_{1/2} \to 4^2\mathbf{P}_{1/2}$) transition optical properties[82]

Property	Symbol	Value
Frequency	ν_0	389.286 058 716(62) THz
Energy	$h\nu_0$	1.609 957 707 081 91 eV
Wavelength	λ	770.108 385 049(123) nm
Lifetime	τ	26.37(5) ns
Natural Line Width (FWHM)		6.03(1) MHz

Rubidium Properties

Cesium Properties

Table 5. Potassium D_2 ($4^2\mathbf{S}_{1/2} \to 4^2\mathbf{P}_{3/2}$) transition optical properties[82]

Property	Symbol	Value
Frequency	ν_0	391.016 170 03(12) THz
Energy	$h\nu_0$	1.617 112 872 240 59 eV
Wavelength	λ	766.700 921 822(24) nm
Lifetime	τ	26.37(5) ns
Natural Line Width (FWHM)		6.035(11) MHz

Table 6. Rubidium (Rb) physical properties

Property	Symbol	Value
Atomic number[†]	Z	37
Total nucleons[†]	$Z + N$	87
Ground state[†]	—	$5s^2 S_{1/2}$
Relative natural abundance[†]	$\eta(^{87}Rb)$	27.83%
Atomic mass[†]	m	86.909 180 520(15) u
Melting point[†]	T_m	39.31 °C
Boiling point[†]	T_b	688 °C
Density (solid)[†]	ρ	1532 kg m^{-3}
Nuclear spin[†]	I	3/2
Magnetic moment	μ	+2.751 24
Ionization energy[†]	E_I	3.893 90(2) eV

[†] Tiecke, T.G. "Properties of Potassium." 2010

Table 7. Rubidium D_1 ($5^2\mathbf{S}_{1/2} \to 5^2\mathbf{P}_{1/2}$) transition optical properties[78]

Property	Symbol	Value
Frequency	ν_0	377.107 463 5(4) THz
Energy	$h\nu_0$	1.559 590 99(6) eV
Wavelength	λ	794.978 850 9(8) nm
Lifetime	τ	27.70(4) ns
Decay Rate	Γ	36.10(5) $\times 10^6$ s^{-1}
Natural Line Width (FWHM)		5.746(8) MHz
Absorption Oscillator Strength	f	0.3420(14)

Table 8. Rubidium D_2 ($5^2\mathbf{S}_{1/2} \to 5^2\mathbf{P}_{3/2}$) transition optical properties[78]

Property	Symbol	Value
Frequency	ν_0	384.230 484 468 5(62) THz
Energy	$h\nu_0$	1.589 049 439(58) eV
Wavelength	λ	780.241 209 686(13) nm
Lifetime	τ	26.24(4) ns
Decay Rate	Γ	$38.11(6) \times 10^6\,\mathrm{s}^{-1}$
Natural Line Width (FWHM)		6.065(9) MHz
Absorption Oscillator Strength	f	0.6956(15)

Table 9. Cesium (Cs) physical properties

Property	Symbol	Value
Atomic number[†]	Z	55
Total nucleons[†]	$Z + N$	133
Ground state[†]	—	$6s^2 S_{1/2}$
Relative natural abundance[†]	$\eta(^{133}Cs)$	100%
Atomic mass[†]	m	132.905 452(1) u
Melting point[†]	T_m	28.44 °C
Boiling point[†]	T_b	671.0 °C
Density (solid)[†]	ρ	$1879\,\mathrm{kg\,m}^{-3}$
Nuclear spin[†]	I	7/2
Magnetic moment	μ	+2.579
Ionization energy[†]	E_I	3.893 90(2) eV

[†] Steck, Daniel A. "Cesium D Line Data." 1998

Table 10. Cesium D_1 ($6^2\mathbf{S}_{1/2} \to 6^2\mathbf{P}_{1/2}$) transition optical properties[79]

Property	Symbol	Value
Frequency	ν_0	335.116 048 807(41) THz
Energy	$h\nu_0$	1.385 928 475(50) eV
Wavelength	λ	894.592 959 86(11) nm
Lifetime	τ	34.894(44) ns
Decay Rate	Γ	$28.659(36) \times 10^6\,\mathrm{s}^{-1}$
Natural Line Width (FWHM)		4.5612(57) MHz
Absorption Oscillator Strength	f	0.3438(13)

Table 11. **Cesium D_2 ($6^2\mathbf{S}_{1/2} \to 6^2\mathbf{P}_{3/2}$) transition optical properties[79]**

Property	Symbol	Value
Frequency	ν_0	$351.725\,718\,50(11)\,\mathrm{THz}$
Energy	$h\nu_0$	$1.454\,620\,542(53)\,\mathrm{eV}$
Wavelength	λ	$852.347\,275\,82(27)\,\mathrm{nm}$
Lifetime	τ	$30.473(39)\,\mathrm{ns}$
Decay Rate	Γ	$32.815(41) \times 10^6\,\mathrm{s}^{-1}$
Natural Line Width (FWHM)		$5.2227(66)\,\mathrm{MHz}$
Absorption Oscillator Strength	f	$0.7148(13)$

Appendix C. Matlab® Code

Importing PeakFit Fitting Data

This code was created to take PEAKFIT®fitting results and import them into
MATLAB®. The code is specifically designed to find a specific type of Voigt fit in
PeakFit, the Voigt G/L, but can easily be altered to extract other types of lines
available in PEAKFIT®. The algorithm runs through a standard PEAKFIT®numeric
export files and outputs a structure containing the data on peaks, line center, ampli-
tude, Lorentzian and Doppler widths, and the associated confidence boundaries for
each. A similar routine is available to extract the fitting data from PEAKFIT®data
export files.

```matlab
1  function PeakFitData = peakFitNumericParse;
2  %% -+-+-+-+-+-+-+-+-+-+-+-+-+-+-+-+-+-+-+-+-+-+-+-+-+-+-+-+-+-+-+-+-+
3  % Created - 2010-12-14 - CAR - Chris Rice - crice@afit.edu
4  % Adapted - 2010-12-14 - CAR - From pollOutputs.m
5  %   Adapted txt file parser for peakfit needs.
6  %-+-+-+-+-+-+-+-+-+-+-+-+-+-+-+-+-+-+-+-+-+-+-+-+-+-+-+-+-+-+-+-+-+
7  % m-File that loads a specialized PeakFit Data Output Text File.
8  %-+-+-+-+-+-+-+-+-+-+-+-+-+-+-+-+-+-+-+-+-+-+-+-+-+-+-+-+-+-+-+-+-+
9
10 %% -+-+-+-+-+-+-+-+-+
11 % Cleanup Environment:
12 %-+-+-+-+-+-+-+-+-+-+
13
14 % clear all;
15 % close all;
16 % clc;
17 % tic;
18
19 %% -+-+-+-+-+-+-+-+-+
20 % Heavy Lifting:
21 %-+-+-+-+-+-+-+-+-+-+
22
23 %Choose File From A Directory:
24 [txtFileName, txtPathName] = uigetfile({'*Numeric*.txt';'*.*'},'Please Pick' ...
25     'a Peakfit Numeric File (Must have Numeric In Name');
26 disp([txtFileName]);
27
28 %Strings To Find:
29 str1 = 'Voigt Area G/L';
```

```matlab
30  str2 = 'r^2 Coef Det  DF Adj r^2   Fit Std Err  F-value';
31
32  %Open the File:
33  FID = fopen([txtPathName,txtFileName],'rt');
34
35  %Pull in a line from the file:
36  theLine = fgetl(FID);
37
38  %Placeholder to find matches:
39  numStrMatches = 0;
40  %4 Bundles of Data in a PeakFit File:
41  currentDataBundle = 0;
42
43  %Scan file, determine how many peaks have been found:
44  while(1)
45      %Get Next Line:
46      theLine = fgetl(FID);
47      %Break at end of file:
48      if(¬ischar(theLine))
49          %Never Found The String:
50          break
51      end
52      %Find A String:
53      K = strfind(theLine,str1);
54      %Check For A Match:
55      if(¬isempty(K))
56          %Found a Match:
57          numStrMatches = numStrMatches+1;
58      end
59      %Find A String:
60      K = strfind(theLine,str2);
61      %Check For A Match:
62      if(¬isempty(K))
63          %Get the next line:
64          theLine = fgetl(FID);
65          %Found a Match:
66          fitParams = str2num(theLine);
67      end
68  end
69
70  %Currently End of File, Rewind:
71  frewind(FID);
72
73  %Disp num of peaks:
74  numPeaks = numStrMatches/4;
75  disp([num2str(numPeaks),' Peaks Found: Parsing...']);
76
77  %Pre-form arrays:
78  bundle1 = zeros(numPeaks,4);
79  bundle2 = zeros(numPeaks,6);
80  bundle3 = zeros(numPeaks,6);
81  bundle4 = zeros(numPeaks,5*4);
```

```matlab
82
83  while(1)
84      %Get Next Line:
85      theLine = fgetl(FID);
86      %Break at end of file:
87      if(¬ischar(theLine))
88          %Never Found The String:
89          break
90      end
91      %Find A String:
92      K = strfind(theLine,str1);
93      %Check for a Match:
94      if(¬isempty(K))
95          %Rotate to next bundle of data:
96          currentDataBundle = currentDataBundle+1;
97          if(currentDataBundle==1)
98              bundle1(1,:) = str2num(theLine(24:end));
99              for(m = 2:numPeaks)
100                 theLine = fgetl(FID);
101                 bundle1(m,:) = str2num(theLine(24:end));
102             end
103         elseif(currentDataBundle==2)
104             bundle2(1,:) = str2num(theLine(24:end));
105             for(m = 2:numPeaks)
106                 theLine = fgetl(FID);
107                 bundle2(m,:) = str2num(theLine(24:end));
108             end
109         elseif(currentDataBundle==3)
110             bundle3(1,:) = str2num(theLine(24:end));
111             for(m = 2:numPeaks)
112                 theLine = fgetl(FID);
113                 bundle3(m,:) = str2num(theLine(24:end));
114             end
115         elseif(currentDataBundle==4)
116             theLine = fgetl(FID);theLine = fgetl(FID);
117             bundle4(1,1:5) = str2num(theLine(8:end));
118             theLine = fgetl(FID);
119             bundle4(1,6:10) = str2num(theLine(8:end));
120             theLine = fgetl(FID);
121             %Check if Doppler Width has been fixed:
122             if(length(str2num(theLine(8:end)))==1)
123                 bundle4(1,11) = str2num(theLine(8:end));
124             else
125                 bundle4(1,11:15) = str2num(theLine(8:end));
126             end
127             theLine = fgetl(FID);
128             bundle4(1,16:20) = str2num(theLine(8:end));
129             for(m = 2:numPeaks)
130                 theLine = fgetl(FID);theLine = fgetl(FID);theLine = fgetl(FID);
131                 theLine = fgetl(FID);
132                 bundle4(m,1:5) = str2num(theLine(8:end));
133                 theLine = fgetl(FID);
```

```matlab
134                 bundle4(m,6:10) = str2num(theLine(8:end));
135                 theLine = fgetl(FID);
136                 %Check if Doppler Width has been fixed:
137                 if(length(str2num(theLine(8:end)))==1)
138                     bundle4(m,11) = str2num(theLine(8:end));
139                 else
140                     bundle4(m,11:15) = str2num(theLine(8:end));
141                 end
142                 theLine = fgetl(FID);
143                 bundle4(m,16:20) = str2num(theLine(8:end));
144             end
145         else
146             %Error:
147             error('Error In File Formatting');
148         end
149     end
150 end
151
152 %Close the File:
153 fclose(FID);
154
155 %% -+-+-+-+-+-+-+-+-+-+
156 % Reorganize Data:
157 %-+-+-+-+-+-+-+-+-+-+
158
159 %Overall Fit Params:
160 PeakFitData.rSq = fitParams(1);
161 PeakFitData.stdErr = fitParams(3);
162 %Order the File Output:
163 PeakFitData.B1 = flipud(bundle1);
164 PeakFitData.B2 = flipud(bundle2);
165 PeakFitData.B3 = flipud(bundle3);
166 PeakFitData.B4 = flipud(bundle4);
167 %File Format:
168 PeakFitData.B1Format = {'a0','a1','a2','a3'};
169 PeakFitData.B2Format = {'Amplitude','Center','FWHM','Asym50','FW Base','Asym10'};
170 PeakFitData.B3Format = {'Anlytc Area','% Area','Int Area','% Area','Centroid',...
171     'Moment2'};
172 PeakFitData.B4Format = {'Area','Area Std.Err','Area t-val','Area 95%',...
173     'Area 105%','Center','Center Std.Err','Center t-val','Center 95%',...
174     'Center 105%','Width 1','Width 1 Std.Err','Width 1 t-val','Width 1 95%',...
175     'Width 1 105%','Width 2','Width 2 Std.Err','Width 2 t-val','Width 2 95%',...
176     'Width 2 105%'};
177
178 %Save MatFile:
179 save([txtFileName(1:19),'PeakFit.mat'],'PeakFitData');
180
181 %Save Excel Spreadsheet:
182 warning off MATLAB:xlswrite:AddSheet;
183 fName = [txtFileName(1:end-4),'-PFD.xls'];
184 delete(fName);
185 xlswrite(fName,PeakFitData.B1Format,'DataSet1','A1');
```

```matlab
186  xlswrite(fName,PeakFitData.B1,'DataSet1','A3');
187  xlswrite(fName,PeakFitData.B2Format,'DataSet2','A1');
188  xlswrite(fName,PeakFitData.B2,'DataSet2','A3');
189  xlswrite(fName,PeakFitData.B3Format,'DataSet3','A1');
190  xlswrite(fName,PeakFitData.B3,'DataSet3','A3');
191  xlswrite(fName,PeakFitData.B4Format,'DataSet4','A1');
192  xlswrite(fName,PeakFitData.B4,'DataSet4','A3');
193  warning on MATLAB:xlswrite:AddSheet;
194
195  %Trash Dumb Default Sheets:
196  fPath = pwd; % Current working directory.
197  sheetName = 'Sheet'; % EN: Sheet, DE: Tabelle, etc. (Lang. dependent)
198  % Open Excel file.
199  objExcel = actxserver('Excel.Application');
200  objExcel.Workbooks.Open(fullfile(fPath, fName)); % Full path is necessary!
201  % Delete sheets.
202  try
203  % Throws an error if the sheets do not exist.
204  objExcel.ActiveWorkbook.Worksheets.Item([sheetName '1']).Delete;
205  objExcel.ActiveWorkbook.Worksheets.Item([sheetName '2']).Delete;
206  objExcel.ActiveWorkbook.Worksheets.Item([sheetName '3']).Delete;
207  catch
208  % Do nothing.
209  end
210  % Save, close and clean up.
211  objExcel.ActiveWorkbook.Save;
212  objExcel.ActiveWorkbook.Close;
213  objExcel.Quit;
214  objExcel.delete;
215
216  %Done:
217  disp('Parse Complete');
218
219  return
```

Model for K D_1 Absorbance

The following code calculated the pressure-broadened absorption for the K D_1hyperfine lines. This code was based off existing code demonstrated with cesium. [5] A line center shift was added, pressure broadening values were changed, as well as parameters related to the hyperfine lines of K.

```matlab
1  function [abs] = fnAbsCoeffKD1(freq,T,PN2,PHe,PCH4,PC2H6,P3He)
2  %% -+-+-+-+-+-+-+-+-+-+-+-+-+-+-+-+-+-+-+-+-+-+-+-+-+-+-+-+-+-+-+-+-+
3  % Adapted - 2012-04-12 - CAR - Chris Rice - crice@afit.edu - From Monte
4  % Anderson's Rb Simulation, fnAbsCoeffRbD1 and D2.
5  % Updated - 2012-04-12 - CAR - Additional updates, finding refs for numbers
6  % Updated - 2012-04-19 - CAR - Finished rate updates & final checks.
7  %-+-+-+-+-+-+-+-+-+-+-+-+-+-+-+-+-+-+-+-+-+-+-+-+-+-+-+-+-+-+-+-+-+
8  % Calculates Potassium D1 absorption coefficent (1/cm) at a given frequency
9  % at temperature T (K) and buffer gas pressures (Torr).
10 %-+-+-+-+-+-+-+-+-+-+-+-+-+-+-+-+-+-+-+-+-+-+-+-+-+-+-+-+-+-+-+-+-+
11
12 %% CONSTANTS
13 global c eo h hbar kB AMU;
14 global AmK39 MK39 Inam39 vo39 Iso39 tau;
15 global AmK41 MK41 Inam41 vo41 Iso41;
16 global TransM numTrans;
17 global dv39S12 dv41S12 vHF SFF;
18
19 % Physical Constants (NIST)
20 c = 2.99792458e8;          % vacuum speed of light (m/s)
21 eo = 8.85418781762e-12;    % vacuum permittivity (F/m)
22 h = 6.62606896e-34;        % Planck const (Js)
23 hbar = 1.054571628e-34;    % Planck const/2pi (Js)
24 kB = 1.3806504e-23;        % Boltzmann const (J/K)
25 AMU = 1.660538782e-27;     % Atomic Mass Unit (kg)
26
27 % Potassium Atomic Data
28 AmK39 = 38.96370668;       % Atomic mass (AMU) of K39
29 AmK41 = 40.96182576;       % Atomic mass (AMU) of K41
30 MK39 = AmK39*AMU;          % Mass of K39 atom (kg)
31 MK41 = AmK41*AMU;          % Mass of K41 atom (kg)
32 Inam39 = 3/2;              % Total nuclear angular momentum K39
33 Inam41 = 3/2;              % Total nuclear angular momentum K41
34 Iso39 = 39;                % Isotope number for K39
35 Iso41 = 41;                % Isotope number for K41
36
37 % K D1 Data
38 vo39 = 389.286058716e12;   % Frequency (Hz) K39
39 vo41 = 389.286294205e12;   % Frequency (Hz) K41
```

```matlab
40  tau = 26.37e-9;              % Lifetime (s) K39 and K41
41
42  % REFERENCE:
43  %    T.G. Tiecke
44  %    Properties of Potassium
45  %    http://staff.science.uva.nl/¬tgtiecke/PotassiumProperties.pdf
46
47  % Transition Matrix, contains allowed transitions and pertenent quantum
48  %    numbers in the format (Inam, Jupper, Flower, Fupper)
49  % NOTE: Jlower is 1/2 (ground state).
50  TransM = [Inam39 1/2 1 2 Iso39;
51            Inam39 1/2 1 2 Iso39;
52            Inam39 1/2 2 1 Iso39;
53            Inam39 1/2 2 2 Iso39;
54            Inam41 1/2 1 1 Iso41;
55            Inam41 1/2 1 2 Iso41;
56            Inam41 1/2 2 1 Iso41;
57            Inam41 1/2 2 2 Iso41];
58  numTrans = length(TransM);
59
60  %% PLACEHOLDER – EVERYONE ABOVE THIS LINE IS GOOD TO GO FOR K!
61
62
63  %% Hyperfine Structure – Transition Frequencies (from TransM)
64  vHF = zeros(1,numTrans);
65  for j = 1:numTrans
66      vHF(j) = (hfsEnergyK(TransM(j,1),1,TransM(j,2),TransM(j,4),TransM(j,5))/h)-...
67      (hfsEnergyK(TransM(j,1),0,1/2,TransM(j,3),TransM(j,5))/h) + dvIso(TransM(j,5));
68  end
69  dv39S12 = hfsEnergyK(Inam39,0,1/2,3,Iso39)/h – hfsEnergyK(Inam39,0,1/2,2,Iso39)/h;
70  dv41S12 = hfsEnergyK(Inam41,0,1/2,2,Iso41)/h – hfsEnergyK(Inam41,0,1/2,1,Iso41)/h;
71
72  %% PLACEHOLDER – EVERYONE ABOVE THIS LINE IS GOOD TO GO FOR K!
73
74  %% Line Strength Factors, SFF
75  SFF = zeros(1,numTrans);
76  for(n = 1:numTrans)
77      SFF(n) = S_fun(TransM(n,3),TransM(n,4),0.5,TransM(n,2),TransM(n,1));
78  end
79
80  %% main function output
81  abs = NumDensityK(T)*CrossSectionK(freq,T,PN2,PHe,PCH4,PC2H6,P3He);
82
83  end    %end of fnAbsCoeffKD1 main function ----------------------------
84
85
86
87  %% fnAbsCoeffKD1 SUBFUNCTIONS ==========================================
88
89
90  %% HYPERFINE ENERGY LEVELS ---------------------------------------------
91  function [dEhfs] = hfsEnergyK(Inam,L,J,F,IsoNum)
```

```matlab
92  % Calculates hyperfine structure energy for Cs D1 and D2.
93  %
94  % REFERENCE:
95  %    T.G. Tiecke
96  %    Properties of Potassium
97  %    http://staff.science.uva.nl/¬tgtiecke/PotassiumProperties.pdf
98
99  global h Iso39 Iso41;
100
101 %Hyperfine Structure Constants for K39:
102 A39S12 = h*230.8598601e6;    %(Hz)
103 A39P12 = h*27.775e6;         %(Hz)
104 A39P32 = h*6.093e6;          %(Hz)
105 B39P32 = h*2.786e6;          %(Hz)
106
107 %Hyperfine Structure Constants for K41:
108 A41S12 = h*127.0069352e6;    %(Hz)
109 A41P12 = h*15.245e6;         %(Hz)
110 A41P32 = h*3.363e6;          %(Hz)
111 B41P32 = h*3.351e6;          %(Hz)
112
113 K = F*(F + 1) - Inam*(Inam + 1) - J*(J + 1);
114
115 % tempStr = fprintf('Inam=%0.5g,L=%0.5g,J=%0.5g,F=%0.5g,IsoNum=%0.5g',Inam,
116 %L,J,F,IsoNum);
117 % disp(tempStr);
118 % keyboard;
119
120 if(IsoNum == Iso39)        % K39 hyperfine energy levels
121     if(L == 0)
122         dEhfs = .5*A39S12*K;
123     elseif(L == 1 && J == .5)
124         dEhfs = .5*A39P12*K;
125     elseif(L == 1 && J == 1.5)
126         dEhfs = (.5*A39P32*K) + B39P32*((1.5*K*(K+1) - 2*Inam*(Inam+1)*J*...
127             (J+1))/(4*Inam*(2*Inam-1)*J*(2*J-1)));
128     else
129         tempStr = fprintf('Inam=%0.5g,L=%0.5g,J=%0.5g,F=%0.5g,IsoNum=%0.5g', ...
130             Inam,L,J,F,IsoNum);
131         disp(tempStr);
132         tempStr = fprintf('IMPROPER INPUTS - Hyperfine energy level' ...
133             'determination');
134         disp(tempStr);
135         dEhfs = 0;
136     end
137 elseif(IsoNum == Iso41)    % K41 hyperfine energy levels
138     if(L == 0)
139         dEhfs = .5*A41S12*K;
140     elseif(L == 1 && J == .5)
141         dEhfs = .5*A41P12*K;
142     elseif(L == 1 && J == 1.5)
143         dEhfs = (.5*A41P32*K) + B41P32*((1.5*K*(K+1) - 2*Inam*(Inam+1)*J*...
```

```matlab
                    (J+1))/(4*Inam*(2*Inam-1)*J*(2*J-1)));
    else
        tempStr = fprintf('Inam=%0.5g,L=%0.5g,J=%0.5g,F=%0.5g,IsoNum=%0.5g',...
            Inam,L,J,F,IsoNum);
        disp(tempStr);
        tempStr = fprintf('IMPROPER INPUTS - Hyperfine energy level ' ...
            'determination');
        disp(tempStr);
        dEhfs = 0;
    end
else
    tempStr = fprintf('Inam=%0.5g,L=%0.5g,J=%0.5g,F=%0.5g,IsoNum=%0.5g',...
        Inam,L,J,F,IsoNum);
    disp(tempStr);
    tempStr = fprintf('IMPROPER INPUTS - Hyperfine energy level determination');
    disp(tempStr);
    dEhfs = 0;
end

end     %end of function


%Hyperfine subfunction
function dvisoOut = dvIso(IsoNum)
% Provides Isotope shift for K39 - all frequencies relative to K41.
global vo39 vo41 Iso39 Iso41;

dvo = vo41 - vo39;          % Isotope's hyperfine spectrum rel. to same
                           %   central frquency vo so that
                           %   voK39 + dviso = voK41

if(IsoNum == Iso39)
    dvisoOut = dvo;
elseif(IsoNum == Iso41)
    dvisoOut = 0;
else
    fprintf('\nERROR -- Isotope Number is outside allowed range.\n\n');
end

end



%% LINE STRENGTH FACTORS ------------------------------------------------
function [S] = S_fun(F,Fprime,J,Jprime,I)
S1 = Wigner6j(J,Jprime,1,Fprime,F,I);
S = (2*Fprime+1)*(2*J+1)*(S1^2);

end     %end of function


%% WIGNER 6j FACTORS ----------------------------------------------------
function Wigner = Wigner6j(j1,j2,j3,J1,J2,J3)
% Wigner 6j-symbol calculator. Written by Amita B Deb, Clarendon Lab. 2007.
```

```matlab
196  % Improved by Richard A. Holt, Univ. of Western Ontario, 2009.
197  % Further improved to deal with large input arguments by Lee Harper,
198  % CRL Oxford, 2009.
199
200  % Builds on the m-file Wigner6jcoeff posted by Richard A. Holt.
201
202  % Calculates { j1, j2 ,j3}  using Racah formula. See: Sobelman: Atomic
203  %Spectra and Radiative Transitions.
204  %               J1  J2  J3
205
206  % Finding Triangular coefficients
207
208  tri1 = triangle_coeff(j1,j2,j3);
209  tri2 = triangle_coeff(j1,J2,J3);
210  tri3 = triangle_coeff(J1,j2,J3);
211  tri4 = triangle_coeff(J1,J2,j3);
212
213  if (tri1==0||tri2==0||tri3==0||tri4==0)
214      Wigner=0;
215      return
216  end
217
218  % Finding the range of summation in the Racah formula.
219
220  a(1) = j1 + j2 + j3;
221  a(2) = j1 + J2 + J3;
222  a(3) = J1 + j2 + J3;
223  a(4) = J1 + J2 + j3;
224
225  rangei = max(a);
226
227  k(1) = j1 + j2 + J1 + J2;
228  k(2) = j2 + j3 + J2 + J3;
229  k(3) = j3 + j1 + J3 + J1;
230
231  rangef = min(k);
232
233  Wigner = 0;
234
235      for t=rangei:rangef
236
237          Wigner = Wigner + ((-1)^t)*exp(gammaln(t+2) - fung(t,j1,j2,j3,J1,J2,J3));
238
239      end
240
241      Wigner = (tri1*tri2*tri3*tri4)^(0.5)*Wigner;
242
243  end
244
245  % ----- Wigner6j subfunctions --------------
246  function r = fung(t, j1,j2,j3,J1,J2,J3)
247  % Calculating the logarithm of the denominator in Racah Formula, using
```

```matlab
248  % the gamma function in place of the factorial.
249  r = sum(gammaln([(t-j1-j2-j3);(t-j1-J2-J3);(t-J1-j2-J3);(t-J1-J2-j3);...
250                   (j1+j2+J1+J2-t);(j2+j3+J2+J3-t);(j3+j1+J3+J1-t)] + 1));
251
252  end
253
254  %-------------------------------------------
255  function tri = triangle_coeff(a,b,c)
256  % Calculates triangle coefficients for angular momenta.
257  % This version returns 0 if the triangle inequalities are violated.  (RAH)
258
259  if (a<0 || b<0 || c<0)
260      tri=0;
261      return
262  end
263
264  for xa = abs(a-b):1:a+b
265      if c==xa
266          tri = factorial(a+b-c)*factorial(a-b+c)*factorial(-a+b+c)/( ...
267              factorial(a+b+c+1));
268          return
269      end
270  end
271
272  tri=0;
273
274  end      %end of function
275
276
277  %% CROSS SECTION AT LINE CENTER --------------------------------------------
278  function [s0] = sigma_0K(SFF,vD,x)
279  % Calculates cross section at line center for each hyperfine transition
280  global c vo39 vo41 tau TransM Iso39 Iso41;
281
282  if(TransM(x,5)==Iso39)
283      vo = vo39;
284  elseif(TransM(x,5)==Iso41)
285      vo = vo41;
286  else
287      fprintf('\nERROR in sigma_0K -- Inam is outside allowed range.\n\n');
288      return;
289  end
290
291  dvnat = 1/(2*pi*tau);
292
293  s0 = SFF(x)*(1/tau)*(((c*100)^2)/(8*pi))*(1/((vo+vD(x))^2))*...
294          ((2*TransM(x,2)+1)/(2*.5+1))*(2/(pi*dvnat));
295
296  end
297
298
299  %% NUMBER DENSITY ----------------------------------------------------------
```

```matlab
300  function [ndensity] = NumDensityK(T)
301  % calculates number density (cm^-3) given Temperature in Kelvin
302  global kB;
303
304  ndensity = (KVaporPressure(T))/(kB*T)*101325*(1e-6);
305  end
306
307
308  %% VAPOR PRESSURE ----------------------------------------------------------
309  function [Pv] = KVaporPressure(T)
310  % Provides K vapor pressure in atmospheres given T in Kelvin
311  %
312  % REFERENCE:
313  %   C.B.Alcock, V.P.Itkin, and M.K.Horrigan
314  %   Vapour pressure equations for the metallic elements: 298-2500K
315  %   Canadian Metallurgical Quarterly, 1984, 23, 309-313
316  %
317  % "Precise" equation for K vapour pressure.
318  % Uses melting point for K at 336.8K (63.65 degC)
319  % Valid for temperatures from melting point to 600K.
320  %
321  %   For best precision, use temperatures between melting point and 600K.
322
323  if(T >= 336.8 && T <= 600)
324      a = 8.233;
325      b = -4693;
326      c = -1.2403;
327      Pv = 10.^(a + b*(T^-1) + c*log10(T));
328  elseif (T >= 298 && T < 336.8)
329      a = 4.961;
330      b = -4646;
331      Pv = 10.^(a + b*(T^-1));
332  elseif (T < 298 || T > 600)
333      fprintf('\nTemperature is outside of allowed range.\n\n')
334      return
335  end
336
337  end
338
339
340  %% CROSS SECTION -----------------------------------------------------------
341  function [cs] = CrossSectionK(x,T,PN2,PHe,PCH4,PC2H6,P3He)
342  % Calculates cross section as function of frequency, x
343  global tau s0 vo39 vo41 TransM vHF numTrans Iso39 Iso41 c SFF;
344
345  dvnat = 1/(2*pi*tau);        % natural linewidth, Δ nu natural
346  csHF = zeros(1,numTrans);   % Cross section for an individual HF transition
347
348  temp = 0;
349  for n = 1:numTrans
350      Flwr = TransM(n,3);
351      IsoNum = TransM(n,5);
```

```matlab
352        [gamma,shift,dvD,dvL] = BufferGasK(T,IsoNum,PN2,PHe,PCH4,PC2H6,P3He);
353        if(IsoNum == Iso39)      % Set central frequency based on isotope (IsoNum)
354            vo = vo39;
355        elseif(IsoNum == Iso41)
356            vo = vo41;
357        else
358            fprintf('\nERROR in CrossSectionK-Isotope Number is outside allowed range.\n\n')
359            return;
360        end
361
362        s0 = SFF(n)*(1/tau)*(((c*100)^2)/(4*pi))*(1/((vo+vHF(n)+shift)^2))*...
363            ((2*TransM(n,2)+1)/(2*.5+1));
364
365        csHF = KNatAbundance(IsoNum) * BoltzRatioK(IsoNum,Flwr,T) * s0 * ...
366            ((x + vHF(n) + shift + vo) / (vHF(n) + shift + vo)) * ...
367            gVoigt((x - vHF(n)-shift),dvL,dvD);
368        temp = temp + csHF;
369    end
370
371 cs = temp;
372
373 end
374
375 %%
376 % Need Total Nuclear Ang. Momentum
377
378 function eta = KNatAbundance(IsoNum)
379 % Return Potassium natural abundance based on Total nuclear angular momentum:
380 global Iso39 Iso41;
381
382 % REFERENCE:
383 %    T.G. Tiecke
384 %    Properties of Potassium
385 %    http://staff.science.uva.nl/¬tgtiecke/PotassiumProperties.pdf
386
387 %Natural Abundance Ratios:
388 Eta39 = 0.932581; %Nuclear Spin = 3/2
389 Eta41 = 0.067302; %Nuclear Spin = 3/2
390 %Note: Eta40 = 0.000117; %Nuclear Spin = 4 and is ignored here b/c of low natural
391 %abundance.
392
393 if (IsoNum == Iso39)
394     eta = Eta39;
395     return;
396 elseif (IsoNum == Iso41)
397     eta = Eta41;
398     return;
399 else
400     fprintf('\nIsotope Number is outside of allowed range for K39 or K41.\n\n');
401     return;
402 end
403
```

```matlab
404  end
405
406  %% BUFFER GAS EFFECTS ------------------------------------------------
407  function [gamma,shift,dvD,dvL] = BufferGasK(T,IsoNum,PN2,PHe,PCH4,PC2H6,P3He)
408  % Rb buffer gas effects - pressure broadening and frequency shift
409  %
410  % REFERENCE:
411  %    Pitz, G. A.
412  %    Pressure broadening and shift of the potassium D1 transition by the
413  %    noble gasses and N2, H2, HD, D2, CH4, C2H6, C38, and n-C4H10
414  %    JQSRT, 113, 387-395 2012.
415
416  global tau c kB Iso39 Iso41 MK39 MK41 vo39 vo41;
417
418  %Calculate Broadening:
419  gamma = (17.78e6)*((T/328)^(1/2))*PN2  ... % MHz/Torr (Pitz)
420        + (13.08e6)*((T/328)^(1/2))*PHe  ... % MHz/Torr (Pitz)
421        + (29.35e6)*((T/328)^(1/2))*PCH4 ... % MHz/Torr (Pitz)
422        + (26.63e6)*((T/328)^(1/2))*PC2H6... % MHz/Torr (Pitz)
423        + (17.46e6)*((T/328)^(1/2))*P3He;    % MHz/Torr (Pitz)
424  % gamma = 0;  %for test purposes to check the buffergas shift
425
426  %Calculate Shift:
427  shift = (-6.80e6)*((T/328)^(1/2))*PN2  ... % MHz/Torr (Pitz)
428        + ( 1.63e6)*((T/328)^(1/2))*PHe  ... % MHz/Torr (Pitz)
429        + (-7.41e6)*((T/328)^(1/2))*PCH4 ... % MHz/Torr (Pitz)
430        + (-8.32e6)*((T/328)^(1/2))*PC2H6... % MHz/Torr (Pitz)
431        + ( 6.82e6)*((T/328)^(1/2))*P3He;    % MHz/Torr (Pitz)
432
433  % Set central frequency and mass based on isotope
434  if (IsoNum == Iso39)
435      vo = vo39;
436      MK = MK39;
437  elseif(IsoNum == Iso41)
438      vo = vo41;
439      MK = MK41;
440  else
441      fprintf('\nERROR in BufferGasK-Iso is outside range.\n\n');
442      return;
443  end
444
445  %Calculate Doppler and Lorentz:
446  dvD = (vo + shift)*((8*kB*T*log(2))/(MK*(c^2)))^(1/2);
447  dvL = (1/(2*pi*tau)) + gamma;
448
449  end
450
451  %% BOLTZMAN RATIO ---------------------------------------------------------
452  function [BR] = BoltzRatioK(IsoNum,F,T)
453  global kB h dv39S12 dv41S12 Iso39 Iso41;
454
455  if(IsoNum == Iso39)
```

```matlab
        if(F == 1)
            BR = 5./(5 + 7*exp(-(h*dv39S12)./(kB.*T)));
        elseif(F == 2)
            BR = (7*exp(-(h*dv39S12)./(kB.*T)))./(5 + 7*exp(-(h*dv39S12)./(kB.*T)));
        elseif(F ≠ 1 && F ≠ 2)
            fprintf('\nIMPROPER INPUTS-455\n\n')
            BR = 0;
        end
elseif(IsoNum == Iso41)
        if(F == 1)
            BR = 3./(3 + 5*exp(-(h*dv41S12)./(kB.*T)));
        elseif(F == 2)
            BR = (5*exp(-(h*dv41S12)./(kB.*T)))./(3 + 5*exp(-(h*dv41S12)./(kB.*T)));
        elseif(F ≠ 1 && F ≠ 2)
            fprintf('\nIMPROPER INPUTS-464\n\n')
            BR = 0;
        end
else
        fprintf('\nIMPROPER INPUTS-468\n\n')
        BR = 0;
end

end


%% VOIGT LINESHAPE ----------------------------------------------------------
function [y] = gVoigt(v,dvL,dvD)
% A useful approximation for the Voigt convolution is given by Thompson
%
% REFERENCE:
% William J. Thompson
% Numerous neat algorithms for the Voigt profile function.
% Computers in Physics, Vol 7, No. 6, Nov/Dec 1993.
%
%   gV(u,a) = Re[Exp(z^2)erfc(z)]
%       z = a + iu
%       a = sqrt(ln(2)) vLorentzian/vDoppler
%       u = 2 sqrt(ln(2)) (v-vo)/vDoppler

% NOTE: Not valid for Doppler free spectra where vDoppler = 0
% NOTE: erfc(z) = 1 - erf(z) (related to the Faddeeva function)

a = sqrt(log(2))*(dvL/dvD);
u = 2*sqrt(log(2))*(v/dvD);
z = a + 1i*u;
y = 2*sqrt(log(2)/pi)*(1/dvD)*real(faddeeva(1i*z));
end

% ----- gVoigt subfunctions --------------

function w = faddeeva(z,N)
% FADDEEVA    Faddeeva function
```

```
508  %    W = FADDEEVA(Z) is the Faddeeva function, aka the plasma dispersion
509  %    function, for each element of Z. The Faddeeva function is defined as:
510  %
511  %       w(z) = exp(-z^2) * erfc(-j*z)
512  %
513  %    where erfc(x) is the complex complementary error function.
514  %
515  %    W = FADDEEVA(Z,N) can be used to explicitly specify the number of terms
516  %    to truncate the expansion (see (13) in [1]). N = 16 is used as default.
517  %
518  %    Example:
519  %        x = linspace(-10,10,1001); [X,Y] = meshgrid(x,x);
520  %        W = faddeeva(complex(X,Y));
521  %        figure;
522  %        subplot(121); imagesc(x,x,real(W)); axis xy square; caxis([-1 1]);
523  %        title('re(faddeeva(z))'); xlabel('re(z)'); ylabel('im(z)');
524  %        subplot(122); imagesc(x,x,imag(W)); axis xy square; caxis([-1 1]);
525  %        title('im(faddeeva(z))'); xlabel('re(z)'); ylabel('im(z)');
526  %
527  %    Reference:
528  %    [1] J.A.C. Weideman, "Computation of the Complex Error Function," SIAM
529  %        J. Numerical Analysis, pp. 1497-1518, No. 5, Vol. 31, Oct., 1994
530  %        Available Online: http://www.jstor.org/stable/2158232
531
532  if nargin<2, N = []; end
533  if isempty(N), N = 16; end
534
535  w = zeros(size(z)); % initialize output
536
537  %%%%%
538  % for purely imaginary-valued inputs, use erf as is if z is real
539  idx = real(z)==0; %
540  w(idx) = exp(-z(idx).^2).*erfc(imag(z(idx)));
541
542  if all(idx), return; end
543  idx = ¬idx;
544
545  %%%%%
546  % for complex-valued inputs
547
548  % make sure all points are in the upper half-plane (positive imag. values)
549  idx1 = idx & imag(z)<0;
550  z(idx1) = conj(z(idx1));
551
552  M = 2*N;
553  M2 = 2*M;
554  k = (-M+1:1:M-1)'; % M2 = no. of sampling points.
555  L = sqrt(N/sqrt(2)); % Optimal choice of L.
556
557  theta = k*pi/M;
558  t = L*tan(theta/2); % Variables theta and t.
559  f = exp(-t.^2).*(L^2+t.^2);
```

```matlab
560  f = [0; f]; % Function to be transformed.
561  a = real(fft(fftshift(f)))/M2; % Coefficients of transform.
562  a = flipud(a(2:N+1)); % Reorder coefficients.
563
564  Z = (L+1i*z(idx))./(L-1i*z(idx));
565  p = polyval(a,Z); % Polynomial evaluation.
566  w(idx) = 2*p./(L-1i*z(idx)).^2 + (1/sqrt(pi))./(L-1i*z(idx)); % Evaluate w(z).
567
568  % convert the upper half-plane results to the lower half-plane if necessary
569  w(idx1) = conj(2*exp(-z(idx1).^2) - w(idx1));
570
571  end
```

Model for K D_2 Absorbance

The following code calculated the pressure-broadened absorption for the K D_2 hyperfine lines. This code was based off existing code demonstrated with cesium. [5] A line center shift was added, pressure broadening values were changed, as well as parameters related to the hyperfine lines of K.

```matlab
1   function [abs] = fnAbsCoeffKD2(freq,T,PN2,PHe,PCH4,PC2H6,P3He)
2   %% -+-+-+-+-+-+-+-+-+-+-+-+-+-+-+-+-+-+-+-+-+-+-+-+-+-+-+-+-+-+-+-+-+-+-+
3   % Adapted - 2012-04-12 - CAR - Chris Rice - crice@afit.edu - From Monte
4   % Anderson's Rb Simulation, fnAbsCoeffRbD1 and D2.
5   % Updated - 2012-04-12 - CAR - Additional updates, finding refs for numbers
6   % Updated - 2012-04-19 - CAR - Finished rate updates & final checks.
7   %-+-+-+-+-+-+-+-+-+-+-+-+-+-+-+-+-+-+-+-+-+-+-+-+-+-+-+-+-+-+-+-+-+-+-+
8   % Calculates Potassium D2 absorption coefficent (1/cm) at a given frequency
9   % at temperature T (K) and buffer gas pressures (Torr).
10  %-+-+-+-+-+-+-+-+-+-+-+-+-+-+-+-+-+-+-+-+-+-+-+-+-+-+-+-+-+-+-+-+-+-+-+
11
12  %% CONSTANTS
13  global c eo h hbar kB AMU;
14  global AmK39 MK39 Inam39 vo39 Iso39 tau;
15  global AmK41 MK41 Inam41 vo41 Iso41;
16  global TransM numTrans;
17  global dv39S12 dv41S12 vHF SFF;
18
19  % Physical Constants (NIST)
20  c = 2.99792458e8;          % vacuum speed of light (m/s)
21  eo = 8.85418781762e-12;    % vacuum permittivity (F/m)
22  h = 6.62606896e-34;        % Planck const (Js)
23  hbar = 1.054571628e-34;    % Planck const/2pi (Js)
24  kB = 1.3806504e-23;        % Boltzmann const (J/K)
25  AMU = 1.660538782e-27;     % Atomic Mass Unit (kg)
26
27  % Potassium Atomic Data
28  AmK39 = 38.96370668;       % Atomic mass (AMU) of K39
29  AmK41 = 40.96182576;       % Atomic mass (AMU) of K41
30  MK39 = AmK39*AMU;          % Mass of K39 atom (kg)
31  MK41 = AmK41*AMU;          % Mass of K41 atom (kg)
32  Inam39 = 3/2;              % Total nuclear angular momentum K39
33  Inam41 = 3/2;              % Total nuclear angular momentum K41
34  Iso39 = 39;                % Isotope number for K39
35  Iso41 = 41;                % Isotope number for K41
36
37  % K D2 Data
38  vo39 = 391.01617003e12;    % Frequency (Hz) K39
39  vo41 = 391.01640621e12;    % Frequency (Hz) K41
```

```matlab
40  tau = 26.37e-9;              % Lifetime (s) K39 and K41
41
42  % REFERENCE:
43  %    T.G. Tiecke
44  %    Properties of Potassium
45  %    http://staff.science.uva.nl/¬tgtiecke/PotassiumProperties.pdf
46
47  % Transition Matrix, contains allowed transitions and pertenent quantum
48  %    numbers in the format (Inam, Jupper, Flower, Fupper, IsoNum)
49  % NOTE: Jlower is 1/2 (ground state).
50  TransM = [Inam39 3/2 1 0 Iso39;
51            Inam39 3/2 1 1 Iso39;
52            Inam39 3/2 1 2 Iso39;
53            Inam39 3/2 2 1 Iso39;
54            Inam39 3/2 2 2 Iso39;
55            Inam39 3/2 2 3 Iso39;
56            Inam41 3/2 1 0 Iso41;
57            Inam41 3/2 1 1 Iso41;
58            Inam41 3/2 1 2 Iso41;
59            Inam41 3/2 2 1 Iso41;
60            Inam41 3/2 2 2 Iso41;
61            Inam41 3/2 2 3 Iso41;];
62  numTrans = length(TransM);
63
64  %% Hyperfine Structure - Transition Frequencies (from TransM)
65  vHF = zeros(1,numTrans);
66  for j = 1:numTrans
67      vHF(j) = (hfsEnergyK(TransM(j,1),1,TransM(j,2),TransM(j,4),TransM(j,5))/h)-...
68    (hfsEnergyK(TransM(j,1),0,1/2,TransM(j,3),TransM(j,5))/h) + dvIso(TransM(j,5));
69  end
70  dv39S12 = hfsEnergyK(Inam39,0,1/2,3,Iso39)/h - hfsEnergyK(Inam39,0,1/2,2,Iso39)/h;
71  dv41S12 = hfsEnergyK(Inam41,0,1/2,2,Iso41)/h - hfsEnergyK(Inam41,0,1/2,1,Iso41)/h;
72
73  %% PLACEHOLDER - EVERYONE ABOVE THIS LINE IS GOOD TO GO FOR K!
74
75  %% Line Strength Factors, SFF
76  SFF = zeros(1,numTrans);
77  for(n = 1:numTrans)
78      SFF(n) = S_fun(TransM(n,3),TransM(n,4),0.5,TransM(n,2),TransM(n,1));
79  end
80
81  %% main function output
82  abs = NumDensityK(T)*CrossSectionK(freq,T,PN2,PHe,PCH4,PC2H6,P3He);
83
84  end    %end of fnAbsCoeffKD2 main function ----------------------------
85
86
87
88  %% fnAbsCoeffKD2 SUBFUNCTIONS ============================================
89
90
91  %% HYPERFINE ENERGY LEVELS ----------------------------------------------
```

```matlab
function [dEhfs] = hfsEnergyK(Inam,L,J,F,IsoNum)
% Calculates hyperfine structure energy for Cs D1 and D2.
%
% REFERENCE:
%   T.G. Tiecke
%   Properties of Potassium
%   http://staff.science.uva.nl/¬tgtiecke/PotassiumProperties.pdf

global h Iso39 Iso41;

%Hyperfine Structure Constants for K39:
A39S12 = h*230.8598601e6;   %(Hz)
A39P12 = h*27.775e6;        %(Hz)
A39P32 = h*6.093e6;         %(Hz)
B39P32 = h*2.786e6;         %(Hz)

%Hyperfine Structure Constants for K41:
A41S12 = h*127.0069352e6;   %(Hz)
A41P12 = h*15.245e6;        %(Hz)
A41P32 = h*3.363e6;         %(Hz)
B41P32 = h*3.351e6;         %(Hz)

K = F*(F + 1) - Inam*(Inam + 1) - J*(J + 1);

if(IsoNum == Iso39)         % K39 hyperfine energy levels
    if(L == 0)
        dEhfs = .5*A39S12*K;
    elseif(L == 1 && J == .5)
        dEhfs = .5*A39P12*K;
    elseif(L == 1 && J == 1.5)
        dEhfs = (.5*A39P32*K) + B39P32*((1.5*K*(K+1) - 2*Inam*(Inam+1)*J*(J+1)) ...
            /(4*Inam*(2*Inam-1)*J*(2*J-1)));
    else
        tempStr = fprintf('Inam=%0.5g,L=%0.5g,J=%0.5g,F=%0.5g,IsoNum=%0.5g',...
            Inam,L,J,F,IsoNum);
        disp(tempStr);
        tempStr = fprintf('IMPROPER INPUTS - Hyperfine energy level ' ...
            'determination');
        disp(tempStr);
        dEhfs = 0;
    end
elseif(IsoNum == Iso41)     % K41 hyperfine energy levels
    if(L == 0)
        dEhfs = .5*A41S12*K;
    elseif(L == 1 && J == .5)
        dEhfs = .5*A41P12*K;
    elseif(L == 1 && J == 1.5)
        dEhfs = (.5*A41P32*K) + B41P32*((1.5*K*(K+1) - 2*Inam*(Inam+1)*J* ...
            (J+1))/(4*Inam*(2*Inam-1)*J*(2*J-1)));
    else
        tempStr = fprintf('Inam=%0.5g,L=%0.5g,J=%0.5g,F=%0.5g,IsoNum=%0.5g', ...
            Inam,L,J,F,IsoNum);
```

```matlab
144            disp(tempStr);
145            tempStr = fprintf('IMPROPER INPUTS - Hyperfine energy level '...
146                'determination');
147            disp(tempStr);
148            dEhfs = 0;
149        end
150    else
151        tempStr = fprintf('Inam=%0.5g,L=%0.5g,J=%0.5g,F=%0.5g,IsoNum=%0.5g',...
152            Inam,L,J,F,IsoNum);
153        disp(tempStr);
154        tempStr = fprintf('IMPROPER INPUTS - Hyperfine energy level determination');
155        disp(tempStr);
156        dEhfs = 0;
157    end
158
159    end      %end of function
160
161    %Hyperfine subfunction
162    function dvisoOut = dvIso(IsoNum)
163    % Provides Isotope shift for K39 - all frequencies relative to K41.
164    global vo39 vo41 Iso39 Iso41;
165
166    dvo = vo41 - vo39;         % Isotope's hyperfine spectrum rel. to same
167                              %    central frquency vo so that
168                              %    voK39 + dviso = voK41
169
170    if(IsoNum == Iso39)
171        dvisoOut = dvo;
172    elseif(IsoNum == Iso41)
173        dvisoOut = 0;
174    else
175        fprintf('\nERROR -- Isotope Number is outside allowed range.\n\n');
176    end
177
178    end
179
180
181    %% LINE STRENGTH FACTORS -----------------------------------------------
182    function [S] = S_fun(F,Fprime,J,Jprime,I)
183    S1 = Wigner6j(J,Jprime,1,Fprime,F,I);
184    S = (2*Fprime+1)*(2*J+1)*(S1^2);
185
186    end      %end of function
187
188
189    %% WIGNER 6j FACTORS ---------------------------------------------------
190    function Wigner = Wigner6j(j1,j2,j3,J1,J2,J3)
191    % Wigner 6j-symbol calculator. Written by Amita B Deb, Clarendon Lab. 2007.
192    % Improved by Richard A. Holt, Univ. of Western Ontario, 2009.
193    % Further improved to deal with large input arguments by Lee Harper,
194    % CRL Oxford, 2009.
195
```

```matlab
196  % Builds on the m-file Wigner6jcoeff posted by Richard A. Holt.
197
198  % Calculates { j1, j2 ,j3}  using Racah formula. See: Sobelman: Atomic
199  %Spectra and Radiative Transitions.
200  %              J1  J2  J3
201
202  % Finding Triangular coefficients
203
204  tri1 = triangle_coeff(j1,j2,j3);
205  tri2 = triangle_coeff(j1,J2,J3);
206  tri3 = triangle_coeff(J1,j2,J3);
207  tri4 = triangle_coeff(J1,J2,j3);
208
209  if (tri1==0||tri2==0||tri3==0||tri4==0)
210      Wigner=0;
211      return
212  end
213
214  % Finding the range of summation in the Racah formula.
215
216  a(1) = j1 + j2 + j3;
217  a(2) = j1 + J2 + J3;
218  a(3) = J1 + j2 + J3;
219  a(4) = J1 + J2 + j3;
220
221  rangei = max(a);
222
223  k(1) = j1 + j2 + J1 + J2;
224  k(2) = j2 + j3 + J2 + J3;
225  k(3) = j3 + j1 + J3 + J1;
226
227  rangef = min(k);
228
229  Wigner = 0;
230
231      for t=rangei:rangef
232
233          Wigner = Wigner + ((-1)^t)*exp(gammaln(t+2) - fung(t,j1,j2,j3,J1,J2,J3));
234
235      end
236
237      Wigner = (tri1*tri2*tri3*tri4)^(0.5)*Wigner;
238
239  end
240
241  % ----- Wigner6j subfunctions --------------
242  function r = fung(t, j1,j2,j3,J1,J2,J3)
243  % Calculating the logarithm of the denominator in Racah Formula, using
244  % the gamma function in place of the factorial.
245  r = sum(gammaln([(t-j1-j2-j3);(t-j1-J2-J3);(t-J1-j2-J3);(t-J1-J2-j3);...
246                  (j1+j2+J1+J2-t);(j2+j3+J2+J3-t);(j3+j1+J3+J1-t)] + 1));
247
```

```matlab
248  end
249
250  %------------------------------------------
251  function tri = triangle_coeff(a,b,c)
252  % Calculates triangle coefficients for angular momenta.
253  % This version returns 0 if the triangle inequalities are violated.  (RAH)
254
255  if (a<0 || b<0 || c<0)
256      tri=0;
257      return
258  end
259
260  for xa = abs(a-b):1:a+b
261      if c==xa
262          tri = factorial(a+b-c)*factorial(a-b+c)*factorial(-a+b+c)/ ...
263              (factorial(a+b+c+1));
264          return
265      end
266  end
267
268  tri=0;
269
270  end     %end of function
271
272
273  %% CROSS SECTION AT LINE CENTER -------------------------------------------
274  function [s0] = sigma_0K(SFF,vD,x)
275  % Calculates cross section at line center for each hyperfine transition
276  global c vo39 vo41 tau TransM Iso39 Iso41;
277
278  if(TransM(x,5)==Iso39)
279      vo = vo39;
280  elseif(TransM(x,5)==Iso41)
281      vo = vo41;
282  else
283      fprintf('\nERROR in sigma_0K -- Inam is outside allowed range.\n\n');
284      return;
285  end
286
287  dvnat = 1/(2*pi*tau);
288
289  s0 = SFF(x)*(1/tau)*(((c*100)^2)/(8*pi))*(1/((vo+vD(x))^2))*...
290          ((2*TransM(x,2)+1)/(2*.5+1))*(2/(pi*dvnat));
291
292  end
293
294
295  %% NUMBER DENSITY ---------------------------------------------------------
296  function [ndensity] = NumDensityK(T)
297  % calculates number density (cm^-3) given Temperature in Kelvin
298  global kB;
299
```

```matlab
300  ndensity = (KVaporPressure(T))/(kB*T)*101325*(1e-6);
301  end
302
303
304  %% VAPOR PRESSURE -------------------------------------------------------
305  function [Pv] = KVaporPressure(T)
306  % Provides K vapor pressure in atmospheres given T in Kelvin
307  %
308  % REFERENCE:
309  %    C.B.Alcock, V.P.Itkin, and M.K.Horrigan
310  %    Vapour pressure equations for the metallic elements: 298-2500K
311  %    Canadian Metallurgical Quarterly, 1984, 23, 309-313
312  %
313  % "Precise" equation for K vapour pressure.
314  % Uses melting point for K at 336.8K (63.65 degC)
315  % Valid for temperatures from melting point to 600K.
316  %
317  %    For best precision, use temperatures between melting point and 600K.
318
319  if(T >= 336.8 && T <= 600)
320      a = 8.233;
321      b = -4693;
322      c = -1.2403;
323      Pv = 10.^(a + b*(T^-1) + c*log10(T));
324  elseif (T >= 298 && T < 336.8)
325      a = 4.961;
326      b = -4646;
327      Pv = 10.^(a + b*(T^-1));
328  elseif (T < 298 || T > 600)
329      fprintf('\nTemperature is outside of allowed range.\n\n')
330      return
331  end
332
333  end
334
335
336  %% CROSS SECTION --------------------------------------------------------
337  function [cs] = CrossSectionK(x,T,PN2,PHe,PCH4,PC2H6,P3He)
338  % Calculates cross section as function of frequency, x
339  global tau s0 vo39 vo41 TransM vHF numTrans Iso39 Iso41 c SFF;
340
341  dvnat = 1/(2*pi*tau);        % natural linewidth, Δ nu natural
342  csHF = zeros(1,numTrans);    % Cross section for an individual HF transition
343
344  temp = 0;
345  for n = 1:numTrans
346      Flwr = TransM(n,3);
347      IsoNum = TransM(n,5);
348      [gamma,shift,dvD,dvL] = BufferGasK(T,IsoNum,PN2,PHe,PCH4,PC2H6,P3He);
349      if(IsoNum == Iso39)      % Set central frequency based on isotope (IsoNum)
350          vo = vo39;
351      elseif(IsoNum == Iso41)
```

```matlab
352            vo = vo41;
353        else
354            fprintf('\nERROR in CrossSectionK-Isotope Number is outside '...
355                'allowed range.\n\n');
356            return;
357        end
358
359        s0 = SFF(n)*(1/tau)*(((c*100)^2)/(4*pi))*(1/((vo+vHF(n)+shift)^2))*...
360            ((2*TransM(n,2)+1)/(2*.5+1));
361
362        csHF = KNatAbundance(IsoNum) * BoltzRatioK(IsoNum,Flwr,T) * s0 * ...
363            ((x + vHF(n) + shift + vo) / (vHF(n) + shift + vo)) * ...
364            gVoigt((x - vHF(n)-shift),dvL,dvD);
365        temp = temp + csHF;
366    end
367
368 cs = temp;
369
370 end
371
372 %%
373 % Need Total Nuclear Ang. Momentum
374
375 function eta = KNatAbundance(IsoNum)
376 % Return Potassium natural abundance based on Total nuclear angular momentum:
377 global Iso39 Iso41;
378
379 % REFERENCE:
380 %   T.G. Tiecke
381 %   Properties of Potassium
382 %   http://staff.science.uva.nl/¬tgtiecke/PotassiumProperties.pdf
383
384 %Natural Abundance Ratios:
385 Eta39 = 0.932581; %Nuclear Spin = 3/2
386 Eta41 = 0.067302; %Nuclear Spin = 3/2
387 %Note: Eta40 = 0.000117; %Nuclear Spin = 4 and is ignored here b/c of low natural
388 %abundance.
389
390 if (IsoNum == Iso39)
391    eta = Eta39;
392    return;
393 elseif (IsoNum == Iso41)
394    eta = Eta41;
395    return;
396 else
397    fprintf('\nIsotope Number is outside of allowed range for K39 or K41.\n\n');
398    return;
399 end
400
401 end
402
403 %% BUFFER GAS EFFECTS ----------------------------------------------------
```

```matlab
404  function [gamma,shift,dvD,dvL] = BufferGasK(T,IsoNum,PN2,PHe,PCH4,PC2H6,P3He)
405  % Rb buffer gas effects - pressure broadening and frequency shift
406  %
407  % REFERENCES:
408  %    Nyunt Lwin and D G McCartan
409  %    Collision broadening of the potassium resonance lines by noble gases
410  %    J. Phys. B: Atom. Molec. Phys., Vol. 11, No. 22. 1978.
411  %
412  %    Pitz, G. A.
413  %    Pressure broadening and shift of the potassium D1 transition by the
414  %    noble gasses and N2, H2, HD, D2, CH4, C2H6, C38, and n-C4H10
415  %    JQSRT, 113, 387-395 2012.
416  %
417  %    Pitz, G. A.
418  %    Private communication for D2 line broadening and shift.
419  %    2012-MAY-01.
420
421  global tau c kB Iso39 Iso41 MK39 MK41 vo39 vo41;
422
423  %Calculate Broadening:
424  gamma = (18.84e6)*((T/400)^(1/2))*PN2  ... % MHz/Torr (Lwin)
425       + (19.84e6)*((T/318)^(1/2))*PHe  ... % MHz/Torr (Pitz Commun.)
426       + (27.78e6)*((T/318)^(1/2))*PCH4 ... % MHz/Torr (Pitz Commun.)
427       + (27.60e6)*((T/318)^(1/2))*PC2H6... % MHz/Torr (Pitz Commun.)
428       + (21.14e6)*((T/328)^(1/2))*P3He;    % MHz/Torr (Extrap. Guess using
429    %D1 Pitz #s)
430  % gamma = 0;  %for test purposes to check the buffergas shift
431
432  %Calculate Shift:
433  shift = (-10.14e6)*((T/400)^(1/2))*PN2  ... % MHz/Torr (Lwin)
434       + (   0.52e6)*((T/318)^(1/2))*PHe  ... % MHz/Torr (Pitz Commun.)
435       + (  -8.38e6)*((T/318)^(1/2))*PCH4 ... % MHz/Torr (Pitz Commun.)
436       + (  -8.04e6)*((T/318)^(1/2))*PC2H6... % MHz/Torr (Pitz Commun.)
437       + (   7.72e6)*((T/328)^(1/2))*P3He;    % MHz/Torr (Extrap. Guess using
438    %D1 Pitz #s)
439
440  % Set central frequency and mass based on isotope
441  if (IsoNum == Iso39)
442      vo = vo39;
443      MK = MK39;
444  elseif(IsoNum == Iso41)
445      vo = vo41;
446      MK = MK41;
447  else
448      fprintf('\nERROR in BufferGasK-Iso is outside range.\n\n');
449      return;
450  end
451
452  %Calculate Doppler and Lorentz:
453  dvD = (vo + shift)*((8*kB*T*log(2))/(MK*(c^2)))^(1/2);
454  dvL = (1/(2*pi*tau)) + gamma;
455
```

```matlab
456 end
457
458
459 %% BOLTZMAN RATIO ---------------------------------------------------------
460 function [BR] = BoltzRatioK(IsoNum,F,T)
461 global kB h dv39S12 dv41S12 Iso39 Iso41;
462
463 if(IsoNum == Iso39)
464     if(F == 1)
465         BR = 5./(5 + 7*exp(-(h*dv39S12)./(kB.*T)));
466     elseif(F == 2)
467         BR = (7*exp(-(h*dv39S12)./(kB.*T)))./(5 + 7*exp(-(h*dv39S12)./(kB.*T)));
468     elseif(F ≠ 1 && F ≠ 2)
469         fprintf('\nIMPROPER INPUTS\n\n')
470         BR = 0;
471     end
472 elseif(IsoNum == Iso41)
473     if(F == 1)
474         BR = 3./(3 + 5*exp(-(h*dv41S12)./(kB.*T)));
475     elseif(F == 2)
476         BR = (5*exp(-(h*dv41S12)./(kB.*T)))./(3 + 5*exp(-(h*dv41S12)./(kB.*T)));
477     elseif(F ≠ 1 && F ≠ 2)
478         fprintf('\nIMPROPER INPUTS\n\n')
479         BR = 0;
480     end
481 else
482     fprintf('\nIMPROPER INPUTS\n\n')
483     BR = 0;
484 end
485
486 end
487
488
489 %% VOIGT LINESHAPE --------------------------------------------------------
490 function [y] = gVoigt(v,dvL,dvD)
491 % A useful approximation for the Voigt convolution is given by Thompson
492 %
493 % REFERENCE:
494 % William J. Thompson
495 % Numerous neat algorithms for the Voigt profile function.
496 % Computers in Physics, Vol 7, No. 6, Nov/Dec 1993.
497 %
498 %   gV(u,a) = Re[Exp(z^2)erfc(z)]
499 %       z = a + iu
500 %       a = sqrt(ln(2)) vLorentzian/vDoppler
501 %       u = 2 sqrt(ln(2)) (v-vo)/vDoppler
502
503 % NOTE: Not valid for Doppler free spectra where vDoppler = 0
504 % NOTE: erfc(z) = 1 - erf(z) (related to the Faddeeva function)
505
506 a = sqrt(log(2))*(dvL/dvD);
507 u = 2*sqrt(log(2))*(v/dvD);
```

```matlab
508  z = a + 1i*u;
509  y = 2*sqrt(log(2)/pi)*(1/dvD)*real(faddeeva(1i*z));
510  end
511
512  % ----- gVoigt subfunctions --------------
513
514  function w = faddeeva(z,N)
515  % FADDEEVA    Faddeeva function
516  %    W = FADDEEVA(Z) is the Faddeeva function, aka the plasma dispersion
517  %    function, for each element of Z. The Faddeeva function is defined as:
518  %
519  %       w(z) = exp(-z^2) * erfc(-j*z)
520  %
521  %    where erfc(x) is the complex complementary error function.
522  %
523  %    W = FADDEEVA(Z,N) can be used to explicitly specify the number of terms
524  %    to truncate the expansion (see (13) in [1]). N = 16 is used as default.
525  %
526  %    Example:
527  %        x = linspace(-10,10,1001); [X,Y] = meshgrid(x,x);
528  %        W = faddeeva(complex(X,Y));
529  %        figure;
530  %        subplot(121); imagesc(x,x,real(W)); axis xy square; caxis([-1 1]);
531  %        title('re(faddeeva(z))'); xlabel('re(z)'); ylabel('im(z)');
532  %        subplot(122); imagesc(x,x,imag(W)); axis xy square; caxis([-1 1]);
533  %        title('im(faddeeva(z))'); xlabel('re(z)'); ylabel('im(z)');
534  %
535  %    Reference:
536  %    [1] J.A.C. Weideman, "Computation of the Complex Error Function," SIAM
537  %        J. Numerical Analysis, pp. 1497-1518, No. 5, Vol. 31, Oct., 1994
538  %        Available Online: http://www.jstor.org/stable/2158232
539
540  if nargin<2, N = []; end
541  if isempty(N), N = 16; end
542
543  w = zeros(size(z)); % initialize output
544
545  %%%%
546  % for purely imaginary-valued inputs, use erf as is if z is real
547  idx = real(z)==0; %
548  w(idx) = exp(-z(idx).^2).*erfc(imag(z(idx)));
549
550  if all(idx), return; end
551  idx = ¬idx;
552
553  %%%%
554  % for complex-valued inputs
555
556  % make sure all points are in the upper half-plane (positive imag. values)
557  idx1 = idx & imag(z)<0;
558  z(idx1) = conj(z(idx1));
559
```

```matlab
560  M = 2*N;
561  M2 = 2*M;
562  k = (-M+1:1:M-1)'; % M2 = no. of sampling points.
563  L = sqrt(N/sqrt(2)); % Optimal choice of L.
564
565  theta = k*pi/M;
566  t = L*tan(theta/2); % Variables theta and t.
567  f = exp(-t.^2).*(L^2+t.^2);
568  f = [0; f]; % Function to be transformed.
569  a = real(fft(fftshift(f)))/M2; % Coefficients of transform.
570  a = flipud(a(2:N+1)); % Reorder coefficients.
571
572  Z = (L+1i*z(idx))./(L-1i*z(idx));
573  p = polyval(a,Z); % Polynomial evaluation.
574  w(idx) = 2*p./(L-1i*z(idx)).^2 + (1/sqrt(pi))./(L-1i*z(idx)); % Evaluate w(z).
575
576  % convert the upper half-plane results to the lower half-plane if necessary
577  w(idx1) = conj(2*exp(-z(idx1).^2) - w(idx1));
578
579  end
```

Use of K D_1 and D_2 Absorption Lines

The following code sample illustrates use of Matlab® functions `fnAbsCoeffKD1.m`, `fnAbsCoeffKD2.m` creating and output for both the D_1 and D_2 K lines. The code below was used to create the spectral profiles for the pressure-broadened DPAL gain cells used to calculate atmospheric molecular absorption.

```matlab
% Adapted - 2012 - CAR - From PMonte Anderson's original code
%-+-+-+-+-+-+-+-+-+-+-+-+-+-+-+-+-+-+-+-+-+-+-+-+-+-+-+-+-+-+-+-+-+-+-+-+
% m-File tha computes Absorption Coefficient D1 and D2 using fnAbsCoeffCsD1
% and fnAbsCoeffCsD2.
%-+-+-+-+-+-+-+-+-+-+-+-+-+-+-+-+-+-+-+-+-+-+-+-+-+-+-+-+-+-+-+-+-+-+-+-+

%% -+-+-+-+-+-+-+-+-+
% Cleanup Environment:
%-+-+-+-+-+-+-+-+-+

close all
clear all
clc

%% -+-+-+-+-+-+-+-+-+
% General Settings:
%-+-+-+-+-+-+-+-+-+

%Start Clock:
tic;

%Vary One Of The Input Parameters:
numPoints = 10000;
VarPMat = 760.*[1,5,10,20];
numRuns = length(VarPMat);

%Pre-create Each Outout Matrix:
absCoeffD1Mat = zeros(numPoints,numRuns);
absCoeffD2Mat = zeros(numPoints,numRuns);

%% -+-+-+-+-+-+-+-+-+
%Run Sim For Each:
%-+-+-+-+-+-+-+-+-+

for(m = 1:numRuns)
    %% calcuations
    c = 2.99792458e8;      %m/s
    voD1 = 389286058.716;  %MHz
    voD2 = 391016170.03;   %MHz
```

```matlab
40
41      %Detune Freq (GHz):
42      nu = linspace(-5000e9,5000e9,numPoints);
43
44      T = 60 + 273.15; %T in K - What should be used here
45      PN2 = 0; %0 (Torr)
46      PHe = VarPMat(m); %200 %Typical DPALs Helium pressure (Torr)
47      PCH4 = 0; %400 %Typical DPALs methane pressure (Torr)
48      PC2H6 = 100; %100 %Typical DPALs ethane pressure (Torr)
49      P3He = 0;
50      cell_length = 5;
51
52      absCoeffD1 = zeros(length(nu),1);
53      absCoeffD2 = zeros(length(nu),1);
54      lambdaD1 = zeros(length(nu),1);
55      lambdaD2 = zeros(length(nu),1);
56      nuD1 = zeros(length(nu),1);
57      nuD2 = zeros(length(nu),1);
58
59      for i=1:length(nu)
60          absCoeffD1(i) = fnAbsCoeffKD1(nu(i),T,PN2,PHe,PCH4,PC2H6,P3He);
61          absCoeffD2(i) = fnAbsCoeffKD2(nu(i),T,PN2,PHe,PCH4,PC2H6,P3He);
62          lambdaD1(i) = c./(nu(i)*(1e-9)+voD1*(1e-3));
63          lambdaD2(i) = c./(nu(i)*(1e-9)+voD2*(1e-3));
64          nuD1(i) = (nu(i)+voD1*(1e6))./(c*100);
65          nuD2(i) = (nu(i)+voD2*(1e6))./(c*100);
66      end
67
68      %Store the Data:
69      absCoeffD1Mat(:,m) = absCoeffD1;
70      absCoeffD2Mat(:,m) = absCoeffD2;
71      absCoeffD1MatNorm(:,m) = absCoeffD1./max(absCoeffD1);
72      absCoeffD2MatNorm(:,m) = absCoeffD2./max(absCoeffD2);
73      %End Of Calc:
74      toc
75  end
76
77  %% -+-+-+-+-+-+-+-+-+-+
78  % Plotting:
79  %-+-+-+-+-+-+-+-+-+-+
80
81  close all;
82  opts = ['font_size,1,font_scale,1.15'];
83  fSz = 1;
84  fSc = 1.15;
85  figurePos = [10 60 1000*(1+sqrt(5))/2 1000];
86
87  %Plot Each Line in Wavenumber:
88  figure;
89  plot(nuD1,absCoeffD1Mat)
90  xlabel('Wavenumber, $cm^{-1}$','Interpreter','latex');
91  ylabel('Abs Coeff $(cm^{-1})$','Interpreter','latex');
```

```matlab
92   title(['$D_1$'],'Interpreter','latex')
93   legend(num2str(VarPMat'))
94   set(gco,'Interpreter','latex');
95   nPlot(gcf,'font_size',fSz,'font_scale',fSc);drawnow;
96   set(gcf,'Position',figurePos);
97
98
99   %% Plot Each Line in Relative Freq:
100  figure;
101  temp = linspace(0,0.9,numRuns);
102  cMat = [temp;temp;temp];
103  for(m = 1:numRuns)
104      plot(nu*1e-9,absCoeffD1Mat(:,m),'Color',cMat(:,m)')
105      hold on;
106  end
107  xlabel('Detuning Freq. (GHz)');
108  ylabel('Abs. Coeff. (cm^{-1})');
109
110  return;
```

Frequency Calibration of Tunable Laser Data Using an Etelon

The following code stitches together spectrally adjacent laser scans of the New-Focus tunable diode lasers and calibrates the x-axis of the final data using an etelon in the absence of a high resolution wavemeter. The algorithm first linearizes each individual scan using the etelon response by finding the peaks given the approximate etelon free spectral range. Then, detector response for the laser power reference signal is used for adjacent scans to find where the two laser scans should be joined together. Additional signals can be used to improve the estimate, however the etleon and laser power reference signal typically work best. Natural eteloning in the system also improves the process of joining adjacent free spectral ranges.

```matlab
1  function [completeDataOut] = mergeFSREtelon(fullData);
2  %% -+-+-+-+-+-+-+-+-+-+-+-+-+-+-+-+-+-+-+-+-+-+-+-+-+-+-+-+-+-+-+-+-+-+-+-+
3  % Created - 2012-03-22 - CAR - Chris Rice - crice@afit.edu
4  % Updated - 2012-03-22 - CAR - Adapted from merge FSR.
5  %-+-+-+-+-+-+-+-+-+-+-+-+-+-+-+-+-+-+-+-+-+-+-+-+-+-+-+-+-+-+-+-+-+-+-+-+
6  % m-File that takes the full data structure and creates a full data output.
7  %-+-+-+-+-+-+-+-+-+-+-+-+-+-+-+-+-+-+-+-+-+-+-+-+-+-+-+-+-+-+-+-+-+-+-+-+
8
9  %% Init:
10
11 %Verbose Mode:
12 verbose = 1;
13
14 %Input Structure Should Look Like:
15 szIn = size(fullData);
16
17 %Number Of Points In Each Collection:
18 numPts = szIn(1);
19 %Input Vector is 5 columns:
20 % Setup:
21 %    SRS510 I ----->DAQ AnIn0
22 %    SRS510 I0----->DAQ AnIn1
23 %    SRS510 Ref---->DAQ AnIn2
24 %    SRS530 Etelon->DAQ AnIn3
25 %    NF Lambda----->DAQ AnIn4
26 numChan = szIn(2);
27
28 %Number of Scans In Collection:
29 numScans = szIn(3);
```

```matlab
30
31  %% Linearize The Data:
32  tempSz = size(fullData);
33  %Pre-create the output:
34  fullDataLinear = zeros(tempSz(1),tempSz(2)+1,tempSz(3));
35  %For each scan, use FSR to linearize data:
36  for(m = 1:numScans)
37      %Find Freq. Axis:
38      [freqOut,freqIn] = linearizeEtelonScan(fullData(:,4,m));
39      %Use Old and New Freq. Matricies to re-scale data:
40      for(n = 1:numChan)
41          fullDataLinear(:,n,m) = interp1(freqIn,fullData(:,n,m),freqOut);
42      end
43      fullDataLinear(:,7,m) = freqOut;
44  end
45
46  %% Heavy Lifting:
47  for(m = 2:numScans);
48      if(verbose);disp(['Joining Scan # = ',num2str(m)]);end
49      %Pull Out Data:
50      leftFSR = fullDataLinear(:,:,m-1);
51      rightFSR = fullDataLinear(:,:,m);
52      %Pass the left FSR and the right FSR Scans:
53      [LFSRInd(m),RFSRInd(m)] = mergeTwoFSREtelon(leftFSR,rightFSR);
54  end
55
56  %% Merge The Data Into One Marix:
57  for(m = 1:numScans)
58      if(m≠1)
59          completeDataOut = [completeDataOut;fullDataLinear(RFSRInd(m):end,:,m)];
60      else
61          completeDataOut = fullDataLinear(1:LFSRInd(m+1),:,m);
62      end
63  end
64
65  %% Check The Relative Freq. Channel, Make Continuous:
66  CDODiff = diff(completeDataOut(:,7));
67  %Find All Positive Movement:
68  posInd = find(CDODiff>0);
69  negInd = find(CDODiff≤0);
70  %Find Where Points Lie:
71  CDOMean = mean(CDODiff(posInd));
72  CDOSTD = std(CDODiff(posInd));
73
74  %Cycle Through Scans:
75  currMaxFreq = completeDataOut(negInd(1),7);
76  freqNew = zeros(size(completeDataOut(:,7)));
77  freqNew(1:negInd(1)) = completeDataOut(1:negInd(1),7);
78  for(m = 2:length(negInd))
79      freqNew(negInd(m-1)+1:negInd(m)) = completeDataOut(negInd(m-1)+1:negInd(m),...
80          7)+currMaxFreq-min(completeDataOut(negInd(m-1)+1:negInd(m),7));
81      %Current Max Freq:
```

```matlab
82          currMaxFreq = freqNew(negInd(m));
83    end
84    %Finish Off Last Scan:
85    freqNew(negInd(m)+1:end) = completeDataOut(negInd(m)+1:end,7)+currMaxFreq-...
86          min(completeDataOut(negInd(m)+1:end,7));
87
88    %Re-write Old Matrix:
89    completeDataOut(:,7) = freqNew;
90
91
92    %% Cleanup:
93    %None.
94    return;
```

Bristol Wavemeter control by Matlab®

The following code demonstrates the use of a Bristol 621A wavemeter with MAT-LAB®. In order to use the following code, the Bristol install package must have been completed, and the files CLDevIface.h, CLDevIface.dll, and CLDevIface.lib must be in the MatLab active path. The Bristol wavemeter has a relatively slow and inaccurate response compared the the High Finesse WSU2, but its use during the course of an experiment is still preferred to no spectral reference and is an excellent diagnostic tool.

```matlab
function [libName,BristolDevHandle] = initBristol(comNumber);
%% -+-+-+-+-+-+-+-+-+-+-+-+-+-+-+-+-+-+-+-+-+-+-+-+-+-+-+-+-+-+-+-+-+-+-+-+
% Created - 2009-02-05 - CAR - Chris Rice - crice@afit.edu
% Updated - 2009-02-12 - CAR - Adapted from test code of runWavemeter
%-+-+-+-+-+-+-+-+-+-+-+-+-+-+-+-+-+-+-+-+-+-+-+-+-+-+-+-+-+-+-+-+-+-+-+-+-+
% Loads Bristol SI Labs CP2101 USB-2-UART Library for access to Bristol
% 621A from MatLab
% NOTE - Currently closure of the Bristol dynamic-linked library causes
% program termination - do not close library until this is fixed by Bristol
%-+-+-+-+-+-+-+-+-+-+-+-+-+-+-+-+-+-+-+-+-+-+-+-+-+-+-+-+-+-+-+-+-+-+-+-+-+

%% -+-+-+-+-+-+-+-+-+-+-+
% Attempt to Load Library:
%-+-+-+-+-+-+-+-+-+-+-+

libName = 'BristolLibrary';

%Check For Load:
libLoaded = libisloaded(libName)
if(libLoaded)
    %If Loaded, Unload and re-load:
    %(Some versions of Britol Lib. Fail During MatLab Unload Calls):
    unloadlibrary(libName)
end

%Loads Library:
loadlibrary('CLDevIface.dll','cldevdll.h','alias',libName);

%Display Functions In Library:
libfunctions(libName);

%View Functions of Library:
libfunctionsview(libName)
```

```matlab
34  %View Version of Library:
35  calllib(libName,'CLGetDllVersion');
36
37  %% -+-+-+-+-+-+-+-+-+-+-+-+-+
38  % Open The Device:
39  %-+-+-+-+-+-+-+-+-+-+-+-+-+-+
40
41  BristolDevHandle = calllib(libName,'CLOpenUSBSerialDevice',comNumber);
42
43  %% -+-+-+-+-+-+-+-+-+-+-+-+-+
44  % Test A Few Calls To Library:
45  %-+-+-+-+-+-+-+-+-+-+-+-+-+-+
46
47  Blambda = calllib(libName,'CLGetLambdaReading',BristolDevHandle)
48  Bpower = calllib(libName,'CLGetPowerReading',BristolDevHandle)
49
50  %% -+-+-+-+-+-+-+-+-+-+-+
51  % Attempt to Cleanup:
52  %-+-+-+-+-+-+-+-+-+-+-+
53
54  %Close the Device:
55  %(Some versions of Britol Lib. Fail During MatLab Unload Calls):
56  test = calllib(libName,'CLCloseDevice',BristolDevHandle)
57
58  %Unload the Library:
59  %(Some versions of Britol Lib. Fail During MatLab Unload Calls):
60  unloadlibrary(libName)
61
62  return
```

High Finesse Wavemeter control by Matlab®

The following code demonstrates the use of a High Finesse WSU2 wavemeter with MATLAB®. In order to use the following code, the High Finesse install package must have been completed, and the file wlmData.dll must be in the MatLab active path or Windows system 32 library folder along with its associated header file. The routine also demonstrates how public functions of the shared library can be investigated, leading future programmers towards other development options.

```matlab
function [libName] = initHFWM;
%% -+-+-+-+-+-+-+-+-+-+-+-+-+-+-+-+-+-+-+-+-+-+-+-+-+-+-+-+-+-+-+-+-+
% Created - 2010-05-01 - CAR - Chris Rice - crice@afit.edu
% Updated - 2010-05-04 - CAR - Changed Source Origin to \{OS}\system32
% Updated - 2010-05-06 - CAR - Altered function, Integrated into system
% Updated - 2011-05-23 - CAR - Added more comments for testing with Stefan
% Burgardt, inserted more 'save' commands for testing.
%-+-+-+-+-+-+-+-+-+-+-+-+-+-+-+-+-+-+-+-+-+-+-+-+-+-+-+-+-+-+-+-+-+-+
% Loads HighFinesse WS-U2 Access dll for control of wavemeter from MatLab
%-+-+-+-+-+-+-+-+-+-+-+-+-+-+-+-+-+-+-+-+-+-+-+-+-+-+-+-+-+-+-+-+-+-+
% Proprietary information!  Copyright Chris Rice.  Proprietary information!
%-+-+-+-+-+-+-+-+-+-+-+-+-+-+-+-+-+-+-+-+-+-+-+-+-+-+-+-+-+-+-+-+-+-+

%% -+-+-+-+-+-+-+-+-+-+-+
% Attempt to Load Library:
%-+-+-+-+-+-+-+-+-+-+-+-+

libName = 'WSULibrary';

%Test to see if 'save' command still works:
save('Test1.mat');

%Check For Load:
libLoaded = libisloaded(libName);
if(libLoaded)
    %If Loaded, Unload and re-load: (Should We Reload or let it be?)
    disp('HighFinesse Library Already Loaded - Unloading...');
    unloadlibrary(libName);
    disp('HighFinesse Library Unload Successfull.');
end

%Test to see if 'save' command still works:
save('Test2.mat')

%Loads Library
```

```matlab
36   %IMPORTANT - ONCE THIS LIBRARY IS OPEN, THE SHARED MEMORY IS USED BY THIS %
37   %LIBRARY ONLY, OTHER COPIES WILL NOT WORK WHILE THIS IS OPEN:
38   loadlibrary('C:\windows\system32\wlmData.dll','C:\windows\system32\wlmData.h',...
39       'alias',libName);
40   disp('HighFinesse Library Load Successfull.');
41
42   %Test to see if 'save' command still works:
43   save('Test3.mat')
44
45   %Display Functions In Library (Not Needed as a function):
46   % libfunctions(libName,'-full');
47
48   %GUI View Functions and Version of Library (Not Needed as a function):
49   % libfunctionsview(libName)
50
51   %% -+-+-+-+-+-+-+-+-+-+-+-+-+
52   % Open The Device:
53   %-+-+-+-+-+-+-+-+-+-+-+-+-+
54
55   % Instantiate - Check for Server, If not start, start it: (Is This Required?)
56   WLMServerOn = 0;
57   %Instantiate(ReasonForCall,Mode,P1,P2)
58   %RFC  [-1=Check For Server | 0=Reset | 1=Insall or Remove Callback for Export
59   % | 2=Copy Pattern | 3=InstControlWLM (Obsolete) | 4=Delay (Obsolete) |
60   % 5=Priority (Obsolete)]
61   %Mode [0=NotifyInstallCallback | 1=NotifyRemoveCallback |
62   % 2=NotifyInstallWaitEvent | 3=NotifyRemoveWaitEvent |
63   % 4=NotifyInstallCallbackEx | 5=NotifyInstallWaitEventEx]
64   %P1   [Callback Address for install of callback or timeout for wait-event]
65   %P2   [Priority of Callback (0=Standard)]
66   WLMServerOn = calllib(libName,'Instantiate',-1,0,0,0);
67
68   %Test to see if 'save' command still works:
69   save('Test4.mat')
70
71   if(WLMServerOn==0)
72       %Test to see if 'save' command still works:
73       save('Test5.mat')
74
75       %Start The WLM Server:
76       %ControlWLM(Action,App,Ver)
77       %Act [1=WLMShow | 2=WLMHide | 3=WLMExit | 10=WLMWait |
78       %20=WLMStartSilent | 40=WLMSilent]
79       %App [Pointer to String of Application to Start (0=NoAppToStart)]
80       %Ver [0=Last Used Server]
81       WLMServerOn = calllib(libName,'ControlWLM',1,0,0);
82   end
83
84   %Test to see if 'save' command still works:
85   save('Test6.mat')
86
87   %Display Wavemeter Version:
```

```matlab
88  WLMVersion = calllib(libName,'GetWLMVersion',1);
89  disp(['Using WSU-2 Version ',num2str(WLMVersion)]);
90
91  %Set the Result Mode UNIT->[0=WLVac, 1=WLAir, 2=Freq, 3=WN, 4=PhotEnergy]:
92  theError = calllib(libName,'SetResultMode',3);
93
94  %Test to see if 'save' command still works:
95  save('Test7.mat')
96
97  %Set Exposure Mode [0=Off, 1=Auto]:
98  theError = calllib(libName,'SetExposureMode',1);
99
100 %Test to see if 'save' command still works:
101 save('Test8.mat')
102
103 %Start Measurement:
104 if(WLMServerOn==1)
105     %Start a measurement operation [0x00=Stop,0x01=Adjustment,
106     % 0x02=Measurement,0x04=Record,0x08=Replay];
107     WLMOperation = calllib(libName,'Operation',2);
108 end
109
110 %Take A Measurement:
111 tempWave = calllib(libName,'GetWavelengthNum',1,0);
112
113 %-+-+-+-+-+-+-+-+-+-+-+-+-+-+-+-+-+-+-+-+-+-+-+-+-+-+-+-+-+-+-+-+-+
114 %All code in this document is Proprietary information! Copyright Chris Rice
115 %-+-+-+-+-+-+-+-+-+-+-+-+-+-+-+-+-+-+-+-+-+-+-+-+-+-+-+-+-+-+-+-+-+
```

High Finesse Wavemeter Calibration and Use

The following code calibrates a High Finesse WSU2 wavemeter using a frequency stabilized HeNe laser using MATLAB®. In order to use the following code, the High Finesse install package must have been completed and the file wlmData.dll must be in the MATLAB® active path or Windows system 32 library folder along with its associated header file. This only works with High Finesse wavemeters with the optional calibration laser port located on the device - the code would need to be altered to use the external fiber switch, a popular option on High Finesse wavemeters.

```matlab
1   function [theError] = calHFWM(HFWMLib);
2   %-+-+-+-+-+-+-+-+-+-+-+-+-+-+-+-+-+-+-+-+-+-+-+-+-+-+-+-+-+-+-+-+-+-+
3   %Chris Rice
4   %Created - 2010-11-10 - CAR - crice@afit.edu
5   %Updated - 2010-11-10 - CAR - Used long string of inputs to make this cal
6   %and cleaned up code outside of this function.
7   %-+-+-+-+-+-+-+-+-+-+-+-+-+-+-+-+-+-+-+-+-+-+-+-+-+-+-+-+-+-+-+-+-+-+
8
9   %Switch To Rear Port (Mode->[1=Serial,2=Separated Low,3=Seperated Specific]
10  %,Port->[Front=1,Back=2],Channel,Not Used):
11  theError1 = calllib(HFWMLib,'SetActiveChannel',3,2,5,0);
12  %Stop a measurement operation [0x00=Stop,0x01=Adjustment,0x02=Measurement,
13  %0x04=Record,0x08=Replay];
14  WLMOperation = calllib(HFWMLib,'Operation',0);
15  %Calibrate the Wavemeter (Type->[0=HeNe],UNIT->[0=WLVac, 1=WLAir, 2=Freq,
16  %3=WN, 4=PhotEnergy],Value,Channel):
17  theError2 = calllib(HFWMLib,'Calibration',0,0,632.9910760,5);
18  %Re-Start a measurement operation [0x00=Stop,0x01=Adjustment,
19  %0x02=Measurement,0x04=Record,0x08=Replay];
20  WLMOperation = calllib(HFWMLib,'Operation',2);
21  %Switch To Front Port (Mode->[1=Serial,2=Seperated Low,3=Seperated
22  %Specific],Port->[Front=1,Back=2],Channel,Not Used):
23  theError3 = calllib(HFWMLib,'SetActiveChannel',3,1,1,0);
24
25  %Combine Errors:
26  theError = theError1|theError2|theError3;
```

This MATLAB®function can be called at any time the High Finesse WSU2 is not being calibrated to retrieve the current frequency of the laser being investigated.

```matlab
function [output] = getHFWM(HFWMLib,cmd);
%-+-+-+-+-+-+-+-+-+-+-+-+-+-+-+-+-+-+-+-+-+-+-+-+-+-+-+-+-+-+-+-+-+-+-+
%Chris Rice
%Created - 2010-11-11 - CAR - crice@afit.edu
%Updated - 2010-11-11 - CAR - Used to find various params from WM
%-+-+-+-+-+-+-+-+-+-+-+-+-+-+-+-+-+-+-+-+-+-+-+-+-+-+-+-+-+-+-+-+-+-+-+
%-'WL' - returns an average for vaccum wavelength in nm
%-+-+-+-+-+-+-+-+-+-+-+-+-+-+-+-+-+-+-+-+-+-+-+-+-+-+-+-+-+-+-+-+-+-+-+

if(strcmp(cmd,'WL'))
    %Get An Average Value, check each one for bad values:
    for(m = 1:10)
        theFreqs(m) = calllib(HFWMLib,'GetFrequencyNum',1,0);
        if(theFreqs(m)<0)
            sampTry = 0;
            while(theFreqs(m)<0)
                pause(0.001);
                theFreqs(m) = calllib(HFWMLib,'GetFrequencyNum',1,0);
                sampTry=sampTry+1;
                if(sampTry>5000)
                    error('Cannot Get Good Sample from Wavemeter');
                    break
                end
            end
        end
    end
    output = 299792.458/mean(theFreqs);
end

%Return Output:
return
```

144

HELEEOS Batch Runs

The following code demonstrates the routine used to run HELEEOS while varying the scenario (pre-created with the HELEEOS GUI), laser type, and if a DPAL, gain cell pressure. The routine also saves the data for future analysis, and the plotting routines plot and sort the associated bar graphs so that the bar graph order is plotted with the shorted bars in the front and the tallest bars in the back.

```matlab
1  %% -+-+-+-+-+-+-+-+-+-+-+-+-+-+-+-+-+-+-+-+-+-+-+-+-+-+-+-+-+-+-+-+-+-+-+-+
2  % Adapted - 2012-05-22 - CAR - Chris Rice - crice@afit.edu - From
3  % sample_ExPERT_script.m
4  % Updated - 2012-05-25 - CAR - From PostProcDataNLinFit.m
5  %   Removed all MatLab nLinFit calls, will use PeakFit for fitting
6  %-+-+-+-+-+-+-+-+-+-+-+-+-+-+-+-+-+-+-+-+-+-+-+-+-+-+-+-+-+-+-+-+-+-+-+-+
7  % m-File that runs HELEEOS through a variety of simulations:
8  %-+-+-+-+-+-+-+-+-+-+-+-+-+-+-+-+-+-+-+-+-+-+-+-+-+-+-+-+-+-+-+-+-+-+-+-+
9
10 %% -+-+-+-+-+-+-+-+-+-+-+-+-+
11 % Setup Initial Variables:
12 %-+-+-+-+-+-+-+-+-+-+-+-+-+
13
14 tic;
15 global inputs outputs
16
17 %Add path for HELEEOS Scripts:
18 %change to your path settings:
19 addpath(genpath('D:\School\Doctorate\HELEEOS\HELEEOS'))
20
21 %Load HELEEOS Pre-Created Profiles:
22 load('D:\School\Doctorate\HELEEOS\HELEEOS\GUIs\HELEEOS\mainHeleeos3Library.mat')
23
24 %Find Out How Many Scinarios There Are - Pull Out Settings:
25 [numGeometries,¬] = size(savedStructures);
26 for(m = 1:numGeometries)
27     runInputsDesc{m} = savedStructures{m,1};
28     runInputs{m} = savedStructures{m,2};
29 end
30
31 %Pick Out Laser Types:
32 numLasers = 4; %K DPAL, Rb DPAL, Cs DPAL, COIL
33 numLasersLabels = {'K','Rb','Cs','COIL'};
34 useLBLRTMs = [1 1 1 1];
35 laserWavelengths = [0.7701 0.7949 0.8945 1.31525].*1e-006;
36 laserTypes = [1 2 3 4];
37
```

```matlab
38  %Number Of Pressures:
39  pressures = [760 760*10 760*20];
40  numPressures = length(pressures);
41
42  %Clear Out Saved Structures - No Longer Needed:
43  clear savedStructures
44
45  %% -+-+-+-+-+-+-+-+-+-+-+-+
46  % Heavy Lifting:
47  %-+-+-+-+-+-+-+-+-+-+-+-+
48
49  %Initalize Counters:
50  counts = 0;
51
52  %Step through each scenario in HELEEOS and calculate irradiance:
53  for(m = 1:numGeometries)
54      for(n = 1:numLasers)
55          for(mm = 1:numPressures)
56              %Pick An Input:
57              inputsStruct = runInputs{m};
58              %Check Time of Calculation:
59              tinit = toc;
60              %Re-structure Inputs For HELEEOS:
61              transformedInputs = GuiStruct2DataStruct(inputsStruct);
62              %Need Assignments For The Following Variables:
63              transformedInputs.DPAL.useLBLRTM = 1;
64              %Switch For Laser Wavelength:
65              transformedInputs.DPAL.laserWavelength = laserWavelengths(n);
66              transformedInputs.Laser.wavelength = laserWavelengths(n);
67              %Switch For Laser Type:
68              transformedInputs.DPAL.laserType = laserTypes(n);
69              %Laser Pressure (Torr):
70              transformedInputs.DPAL.laserPressure = pressures(mm);
71              transformedInputs.DPAL.runDesc = runInputsDesc{m};
72
73              %Execute calculation:
74              outputs = heleeosCalcTotalScenario(transformedInputs,false);
75
76              %Store All Inputs And Outputs:
77              AllInputs{m,n,mm} = transformedInputs;
78              AllOutputs{m,n,mm}= outputs;
79
80              %Store  Outputs (Peak Irradiance, All Effects):
81              out{m,n,mm} = outputs.avg.irrAllEffectsPeak;
82
83              %Update Cycle:
84              counts = counts + 1;
85              %Update Display:
86              avgTime = toc/(counts);
87              timeRemaining = (numGeometries*numLasers*numPressures-counts)*...
88                  avgTime;
89              disp(['Done with Site ',num2str(counts),'/',num2str(numGeometries*...
```

```matlab
90                    numLasers*numPressures)]);
91               disp(['Time Remaining ',num2str(timeRemaining),' Avg Time: ',...
92                    num2str(avgTime)]);
93               pause(.01);
94           end
95       end
96  end
97
98  %% -+-+-+-+-+-+-+-+-+-+-+-+-+
99  % Save Those Outputs:
100 %-+-+-+-+-+-+-+-+-+-+-+-+-+
101
102 tempStr = ['HELEEOSRuns-',datestr(now),'.mat'];
103 tempStr = strrep(tempStr,':','-');
104 save(tempStr,'AllOutputs','AllInputs');
105 tempStr = ['HELEEOSRunsAll-',datestr(now),'.mat'];
106 tempStr = strrep(tempStr,':','-');
107 save(tempStr);
108
109 %% -+-+-+-+-+-+-+-+-+-+-+-+-+
110 % Plotting Molec Abs:
111 %-+-+-+-+-+-+-+-+-+-+-+-+-+
112
113 %Close Exiting Figures:
114 close all;
115 %Make a Figure For Each Scenario:
116 figHands = [];
117 for(m = 1:numGeometries)
118     figHands(end+1) = figure('Name',[runInputsDesc{m},'-IntAbs']);
119     for(n = 1:numLasers)
120         for(mm = 1:numPressures)
121             %Collect Settings:
122             tempIn = AllInputs{m,n,(mm)};
123             tempOut = AllOutputs{m,n,(mm)};
124             %Plot Results:
125             varToPlot = 'tempOut.Atmosphere.molecAbs';
126             if(n==4)
127                 faceColorVal = [1 1 1];
128             else
129                 faceColorVal = [mm/numPressures 0 1-mm/numPressures];
130             end
131             tempStr = ['bar(n,sum(',varToPlot,'),''FaceColor'',faceColorVal);'];
132             tempH(mm) = eval(tempStr);
133             tempVal(mm) = eval(['sum(',varToPlot,');']);
134             tempF = get(tempH(mm),'Child');
135             set(tempF,'FaceAlpha',1);
136             hold on;
137         end
138         %Stack The Three Objects, Highest In Back:
139         [¬,tempIndMax] = max(tempVal);
140         [¬,tempIndMin] = min(tempVal);
141         uistack(tempH(tempIndMax),'bottom');
```

147

```matlab
142            uistack(tempH(tempIndMin),'top');
143        end
144        set(gca,'XTick',[1:numLasers]);
145        set(gca,'XTickLabel',numLasersLabels);
146        ylabel(varToPlot);
147        title(runInputsDesc{m});
148        %Make Figures Nice:
149
150    end
151
152
153    %% -+-+-+-+-+-+-+-+-+-+-+-+-+-+-+
154    % Plotting Strehl:
155    %-+-+-+-+-+-+-+-+-+-+-+-+-+-+-+
156
157    %Close Exiting Figures:
158    close all;
159    %Make a Figure For Each Scenario:
160    varToPlot = 'beamStrehl';
161    figHands = [];
162    for(m = 1:numGeometries)
163        figHands(end+1) = figure('Name',[runInputsDesc{m},'-','BeamStrehl']);
164        for(n = 1:numLasers)
165            for(mm = 1:numPressures)
166                %Collect Settings:
167                tempIn = AllInputs{m,n,(mm)};
168                tempOut = AllOutputs{m,n,(mm)};
169                %Plot Results:
170                irrDiff = tempOut.avg.irrDiffPeak;
171                irrDiffBQTurb = tempOut.avg.irrDiffBQTurbPeak;
172                irrDiffBQTurbTB = tempOut.avg.irrDiffBQTurbTBPeak;
173                irrAllEff = tempOut.avg.irrAllEffectsPeak;
174                beamStrehl = irrAllEff/irrDiff;
175                if(n==4)
176                    faceColorVal = [1 1 1];
177                else
178                    faceColorVal = [mm/numPressures 0 1-mm/numPressures];
179                end
180                tempStr = ['bar(n,sum(',varToPlot,'),''FaceColor'',faceColorVal);'];
181                tempH(mm) = eval(tempStr);
182                tempVal(mm) = eval(['sum(',varToPlot,');']);
183                tempF = get(tempH(mm),'Child');
184                set(tempF,'FaceAlpha',1);
185                hold on;
186            end
187            %Stack The Three Objects:
188            [¬,tempIndMax] = max(tempVal);
189            [¬,tempIndMin] = min(tempVal);
190            uistack(tempH(tempIndMax),'bottom');
191            uistack(tempH(tempIndMin),'top');
192            disp(num2str(tempVal));
193            tempValues(m,n) = (1-min(tempVal)/max(tempVal));
```

```matlab
194            disp(['LT = ',num2str(n),'% Diff = ',num2str(1-min(tempVal)/...
195                max(tempVal))]);
196        end
197        set(gca,'XTick',[1:numLasers]);
198        set(gca,'XTickLabel',numLasersLabels);
199        ylabel(varToPlot);
200        title(runInputsDesc{m});
201    end
202
203    %% -+-+-+-+-+-+-+-+-+-+-+-+-+-+
204    % Plotting Dwell Time:
205    %-+-+-+-+-+-+-+-+-+-+-+-+-+-+
206
207    %Close Exiting Figures:
208    close all;
209    %Make a Figure For Each Scenario:
210    varToPlot = 'tempOut.dwellTime';
211    figHands = [];
212    for(m = 1:numGeometries)
213        figHands(end+1) = figure('Name',[runInputsDesc{m},'-','DwellTime']);
214        for(n = 1:numLasers)
215            for(mm = 1:numPressures)
216                %Collect Settings:
217                tempIn = AllInputs{m,n,(mm)};
218                tempOut = AllOutputs{m,n,(mm)};
219                %Plot Results:
220                if(n==4)
221                    faceColorVal = [1 1 1];
222                else
223                    faceColorVal = [mm/numPressures 0 1-mm/numPressures];
224                end
225                tempStr = ['bar(n,sum(',varToPlot,'),''FaceColor'',faceColorVal);'];
226                tempH(mm) = eval(tempStr);
227                tempVal(mm) = eval(['sum(',varToPlot,');']);
228                tempF = get(tempH(mm),'Child');
229                set(tempF,'FaceAlpha',1);
230                hold on;
231            end
232            %Stack The Three Objects, Highest In Back:
233            [¬,tempIndMax] = max(tempVal);
234            [¬,tempIndMin] = min(tempVal);
235            uistack(tempH(tempIndMax),'bottom');
236            uistack(tempH(tempIndMin),'top');
237        end
238        set(gca,'XTick',[1:numLasers]);
239        set(gca,'XTickLabel',numLasersLabels);
240        ylabel(varToPlot);
241        title(runInputsDesc{m});
242        %Make Figures Nice:
243
244    end
```

Bibliography

1. "Airborne Laser Test Bed Successful in Lethal Intercept Experiment". URL `http://www.mda.mil/news/10news0002.html`.

2. "International Conference on Tunable Diode Laser Spectroscopy", June 2012. URL `http://tdls.conncoll.edu/`.

3. "Navy Laser Destroys Unmanned Aerial Vehicle in a Maritime Environment", July 2012. URL `http://www.navsea.navy.mil/nswc/dahlgren/NEWS/LAWS/LAWS.aspx`.

4. Anderson, Joel R., Michael R. Hawks, Kevin C. Gross, and Glen P. Perram. "Flight test of an imaging O_2 (X-b) monocular passive ranging instrument". volume 8020, 802005. SPIE, May 13, 2011 2011.

5. Anderson, M. D. "Tunable Optical Delay in Doppler-Broadened Cesium Vapor". *AFIT Dissertation*, 2010.

6. Arita, Y., R. Stevens, and P. Ewart. "Multi-mode absorption spectroscopy of oxygen for measurement of concentration, temperature and pressure". *Applied Physics B: Lasers and Optics*, 90(2):205–211, 2008.

7. Arita, Y., R. Stevens, and P. Ewart. "Multi-mode absorption spectroscopy of oxygen for measurement of concentration, temperature and pressure", 2008.

8. Babcock, H. D. and L. Herzberg. "Fine Structure of the Red System of Atmospheric Oxygen Bands." *The Astrophysical Journal*, 108:167, 1948.

9. Barbu, T. L., I. Vinogradov, G. Durry, O. Korablev, E. Chassefire, and J. L. Bertaux. "TDLAS a laser diode sensor for the in situ monitoring of H_2O, CO_2 and their isotopes in the Martian atmosphere". *Advances in Space Research*, 38(4):718–725, 2006.

10. Barbu, T. Le, B. Parvitte, V. Zninari, I. Vinogradov, O. Korablev, and G. Durry. "Diode laser spectroscopy of H_2O and CO_2 in the 1.877 μmregion for the in situ monitoring of the Martian atmosphere". *Applied Physics B: Lasers and Optics*, 82(1):133–140, 2006.

11. Barrass, S., Y. Grard, R.J. Holdsworth, and P.A. Martin. "Near-infrared tunable diode laser spectrometer for the remote sensing of vehicle emissions". *Spectrochimica Acta Part A: Molecular and Biomolecular Spectroscopy*, 60(14):3353–3360, 2004.

12. Belotti, Claudio, Fabrizio Cuccoli, Luca Facheris, and Orlando Vaselli. "Atmospheric CO_2 measurements over an active volcano site using an IR laser system". volume 4817, 233–240. SPIE, September 2002.

13. Bernath, P. F. *Spectra of atoms and molecules.* Oxford University Press, USA, 2005.

14. Bogachev, A.V., S. G. Garanin, A.M. Dudov, V.A. Eroshenko, S.M. Kulikov, G.T. Mikaelian, V.A. Panarin, V.O. Pautov, A.V. Rus, and S.A. Sukharev. "Diode-pumped caesium vapour laser with closed-cycle laser-active medium circulation". *Quantum Electronics*, 42(2):95–98, 2012.

15. Brown, M. S., S. Williams, C. D. Lindstrom, and D. L. Barone. *Progress in Applying Tunable Diode Laser Absorption Spectroscopy to Scramjet Isolators and Combustors*, 2010.

16. Burgard, D. A., G. A. Bishop, R. S. Stadtmuller, T. R. Dalton, and D. H. Stedman. "Spectroscopy applied to on-road mobile source emissions". *Applied Spectroscopy*, 60(5):135, 2006.

17. C. A. Rice, G. E. Lott and G. P. Perram. "Open-path atmospheric transmission for the diode pumped cesium laser", Submitted to Applied Optics, 2012.

18. Cheng, M. D., E. Corporan, M. J. DeWitt, C. W. Spicer, M. W. Holdren, K. A. Cowen, A. Laskin, D. B. Harris, R. C. Shores, and R. Kagann. "Probing Emissions of Military Cargo Aircraft: Description of a Joint Field Measurement Strategic Environmental Research and Development Program". *Journal of the Air and Waste Management Association*, 58(6):787–796, 2008.

19. Clough, S.A., M.W. Shephard, E.J. Mlawer, J.S. Delamere, M.J. Iacono, K. Cady-Pereira, S. Boukabara, and P.D. Brown. "Atmospheric radiative transfer modeling: A summary of the AER codes". *Journal of Quantitative Spectroscopy and Radiative Transfer*, 91(2):233–244, 2005.

20. Demtrder, W. *Laser spectroscopy: basic concepts and instrumentation.* Springer Verlag, 2003.

21. Diskin, G. S., J. R. Podolske, G. W. Sachse, and T. A. Slate. "Open-path airborne tunable diode laser hygrometer". *Proceedings of SPIE*, volume 4817, 196. 2002.

22. Duffy, Thomas. "Whats Next for Airborne Laser?", July 2010. URL `http://www.airforce-magazine.com/MagazineArchive/Pages/2010/April\%202010`.

23. Durry, G., T. Danguy, and I. Pouchet. "Open multipass absorption cell for in situ monitoring of stratospheric trace gas with telecommunication laser diodes". *Applied Optics*, 41(3):424–433, 2002.

24. Durry, G., A. Hauchecorne, J. Ovarlez, H. Ovarlez, I. Pouchet, V. Zeninari, and B. Parvitte. "In situ measurement of H_2O and CH_4 with telecommunication laser

diodes in the lower stratosphere: dehydration and indication of a tropical air intrusion at mid-latitudes". *Journal of Atmospheric Chemistry*, 43(3):175–194, 2002.

25. Durry, G., JS Li, I. Vinogradov, A. Titov, L. Joly, J. Cousin, T. Decarpenterie, N. Amarouche, X. Liu, and B. Parvitte. "Near infrared diode laser spectroscopy of C_2H_2, H_2O, CO_2 and their isotopologues and the application to TDLAS, a tunable diode laser spectrometer for the martian PHOBOS-GRUNT space mission". *Applied Physics B: Lasers and Optics*, 99(1):339–351, 2010.

26. Durry, G. and G. Megie. "Atmospheric CH_4 and H_2O Monitoring With Near-Infrared InGaAs Laser Diodes by the SDLA, a Balloonborne Spectrometer for Tropospheric and Stratospheric In Situ Measurements". *Applied Optics*, 38(36):7342–7354, 1999.

27. Durry, G. and G. Megie. "In Situ Measurements of H_2O From a Stratospheric Balloon by Diode Laser Direct-Differential Absorption Spectroscopy at 1.39 m". *Applied Optics*, 39(30):5601–5608, 2000.

28. Ehrenreich, T., B. Zhdanov, T. Takekoshi, S.P. Phiopps, and R. J. Knize. "Diode pumped cesium laser". *Bulletin of the American Physical Society*, 2005.

29. Fiorino, S.T., R.J. Bartell, G.P. Perram, D.W. Bunch, L.E. Gravley, C.A. Rice, Z.P. Manning, M.J. Krizo, J.R. Roadcap, and G.Y. Jumper. "The HELEEOS atmospheric effects package: A probabilistic method for evaluating uncertainty in low-altitude high energy laser effectiveness". *J.Dir.Energy*, 1(4):347–360, 2006.

30. Fried, A., G. Diskin, P. Weibring, D. Richter, JG Walega, G. Sachse, T. Slate, M. Rana, and J. Podolske. "Tunable infrared laser instruments for airborne atmospheric studies". *Applied Physics B: Lasers and Optics*, 92(3):409–417, 2008.

31. Fried, A., Y. N. Lee, G. Frost, B. Wert, B. Henry, J. R. Drummond, G. Hubler, and T. Jobson. "Airborne CH_2O measurements over the North Atlantic during the 1997 NARE campaign: Instrument comparisons and distributions". *J.Geophys.Res*, 107(10.1029), 2002.

32. Fried, A., S. Sewell, B. Henry, B. P. Wert, T. Gilpin, and J. R. Drummond. "Tunable diode laser absorption spectrometer for ground-based measurements of formaldehyde". *Journal of Geophysical Research*, 102:6253–6266, 1997.

33. Frish, M. B., R. T. Wainner, J. Stafford-Evans, B. D. Green, M. G. Allen, S. Chancey, J. Rutherford, G. Midgley, and P. Wehnert. "Standoff sensing of natural gas leaks: evolution of the remote methane leak detector (RMLD)". *Photonic Applications Systems Technologies Conference*. Optical Society of America, 2006.

34. Frish, M.B., R.T. Wainner, B.D. Green, J. Stafford-Evans, M.C. Laderer, and M.G. Allen. "Progress in reducing size and cost of trace gas analyzers based on Tunable Diode Laser Absorption Spectroscopy". *Proceedings of SPIE*, volume 5586, 76–82. 2004.

35. Frish, Michael B., Michael A. White, and Mark G. Allen. "Handheld laser-based sensor for remote detection of toxic and hazardous gases". volume 4199, 19–28. SPIE, February 14, 2001 2001.

36. Gourevitch, A., G. Venus, V. Smirnov, DA Hostutler, and L. Glebov. "Continuous wave, 30 W laser-diode bar with 10 GHz linewidth for Rb laser pumping". *Optics Letters*, 33(7):702–704, 2008.

37. Gurlit, W., R. Zimmermann, C. Giesemann, T. Fernholz, V. Ebert, J. Wolfrum, U. Platt, and J. P. Burrows. "Lightweight diode laser spectrometer CHILD (Compact High-altitude In-situ Laser Diode) for balloonborne measurements of water vapor and methane". *Applied Optics*, 44(1):91–102, 2005.

38. Hawks, M. R. and G. P. Perram. "Passive ranging of emissive targets using atmospheric oxygen absorption lines". *Proceedings of SPIE*, volume 5811, 112. 2005.

39. Hawks, Michael and Glen Perram. "Passive ranging of boost-phase missiles". volume 6569, 65690G. SPIE, April 27, 2007 2007.

40. Holloway, J. S., R. O. Jakoubek, D. D. Parrish, C. Gerbig, A. Volz-Thomas, S. Schmitgen, A. Fried, B. Wert, B. Henry, and J. R. Drummond. "Airborne intercomparison of vacuum ultraviolet fluorescence and tunable diode laser absorption measurements of tropospheric carbon monoxide". *Journal of geophysical research*, 105(D19):24,251–24,261, 2000.

41. Hoor, Peter M., Horst Fischer, Stephanie Wong, Andreas Engel, and Thomas Wetter. "Intercomparison of airborne N_2O measurements using tunable diode laser absorption spectroscopy and in-situ gas chromatography". volume 3758, 109–115. SPIE, October 1999.

42. Hunsmann, S., K. Wunderle, S. Wagner, U. Rascher, U. Schurr, and V. Ebert. "Absolute, high resolution water transpiration rate measurements on single plant leaves via tunable diode laser absorption spectroscopy (TDLAS) at 1.37 μm". *Applied Physics B: Lasers and Optics*, 92(3):393–401, 2008.

43. Kormann, Robert, Horst Fischer, and Frank G. Wienhold. "Compact multi-laser TDLAS for trace gas flux measurements based on a micrometeorological technique". volume 3758, 162–169. SPIE, October 1999.

44. Krupke, W. F. *U.S. Patent 6,643,311: Diode-pumped alkali laser*, 2003.

45. Krupke, W. F. "Diode pumped alkali lasers (DPALs) - an overview". *Proc. SPIE*, volume 7005, 700521. 2008.

46. Krupke, W. F., R. J. Beach, V. K. Kanz, and S. A. Payne. "Diode pumpable rubidium laser". *Advanced Solid-State Photonics*. Optical Society of America, 2003.

47. Krupke, W. F., R. J. Beach, V. K. Kanz, and S. A. Payne. "Resonance transition 795-nm rubidium laser". *Optics Letters*, 28(23):2336–2338, 2003.

48. Lavan, M. "High Energy Laser Systems for Short Range Defense". *Acta Physica Polonica-Series A General Physics*, 115(6), 2009.

49. Li, Y., J. J. Schwab, and K. L. Demerjian. "Measurements of ambient ammonia using a tunable diode laser absorption spectrometer: Characteristics of ambient ammonia emissions in an urban area of New York City". *Journal of geophysical research*, 111(D10):D10S02, 2006.

50. Li, Y.Q., K.L. Demerjian, M.S. Zahniser, D.D. Nelson, J.B. McManus, and S.C. Herndon. "Measurement of formaldehyde, nitrogen dioxide, and sulfur dioxide at Whiteface Mountain using a dual tunable diode laser system". *Journal of geophysical research*, 109(D16):D16S08, 2004.

51. Lins, B., P. Zinn, R. Engelbrecht, and B. Schmauss. "Simulation-based comparison of noise effects in wavelength modulation spectroscopy and direct absorption TDLAS". *Applied Physics B: Lasers and Optics*, 100(2):367–376, 2010.

52. Lott, G. E. "Cesium Absorption Spectrum Perturbed by Argon: Observation of Non-Lorentzian Wing Properties". *AFIT Thesis*, 2012.

53. Macdonald, Douglas J., Michael R. Hawks, and Kevin C. Gross. "Passive ranging using mid-wavelength infrared atmospheric attenuation". volume 7660, 766041. SPIE, April 23, 2010 2010.

54. Miller, W., C. Sulham, J. Holtgrave, and G. Perram. "Limitations of an optically pumped rubidium laser imposed by atom recycle rate". *Applied Physics B: Lasers and Optics*, 103(4):819–824, 2011.

55. Nelson, D.D., M.S. Zahniser, J.B. McManus, C.E. Kolb, and J.L. Jimenez. "A tunable diode laser system for the remote sensing of on-road vehicle emissions". *Applied Physics B: Lasers and Optics*, 67(4):433–441, 1998.

56. OMahony, A., M.E. Pemble, and I.M. Povey. "Infrared and near-infrared spectroscopic probing of atomic layer deposition processes". *Journal of Molecular Structure*, 976(1):324–327, 2010.

57. Perram, G. P., S. J. Cusumano, R. L. Hengehold, S. T. Fiorino, and Air Force Institute of Technology (US). *An introduction to laser weapon systems*. Directed Energy Professional Society, 2010.

58. Petty, G. W. *A first course in atmospheric radiation*. Sundog Pub, 2006.

59. Pitz, G. A., C. D. Fox, and G. P. Perram. "Pressure broadening and shift of the cesium D_2 transition by the noble gases and N_2, H_2, HD, D_2, CH_4, C_2H_6, CF_4, and ^{3}He with comparison to the D_1 transition". *Physical Review A*, 82(4):042502, 2010.

60. Pitz, G. A., C. D. Fox, and G. P. Perram. "Transfer between the cesium $6^2P_{1/2}$ and $6^2P_{3/2}$ levels induced by collisions with H_2, HD, D_2, CH_4, C_2H_6, CF_4, and C_2F_6". *Physical Review A*, 84(3):032708, 2011.

61. Pitz, G. A., D. Wertepny, and G. P. Perram. "Pressure broadening and shift of the cesium D_1 transition by the noble gases and N_2, H_2, HD, D_2, CH_4, C_2H_6, CF_4, and ^{3}He". *Physical Review A*, 80:062718, 2009.

62. Pope, Robert S., Paul J. Wolf, and Glen P. Perram. "A study of collision broadening in the O_2 A-band with the noble gases using Fourier transform spectroscopy". *Journal of Molecular Spectroscopy*, 223(2):205–213, 2 2004.

63. Readle, J. D., C. J. Wagner, J. T. Verdeyen, DA Carroll, and J. G. Eden. "Lasing in Cs at 894.3 nm pumped by the dissociation of CsAr excimers". *Electronics Letters*, 44(25):1466–1467, 2008.

64. Rice, C. A. and G. Perram. "A tunable diode laser absorption system for long path atmospheric transmission and high energy laser applications". *Proceedings of SPIE*, volume 7924, 79240K. 2011.

65. Rice, Christopher A. and G. P. Perram. "Investigation of atmospheric O_2 $X^3\Sigma_g^-$ to $b^1\Sigma_g^+$ using open-path tunable diode laser absorption spectroscopy", Submitted to Appl. Phys. B, 2012.

66. Rice, Christopher A. and Glen Perram. "A tunable diode laser absorption system for long path atmospheric transmission and high energy laser applications". volume 7924, 79240K. SPIE, February 10, 2011 2011.

67. Ritter, KJ and TD Wilkerson. "High-resolution spectroscopy of the oxygen A band". *Journal of Molecular Spectroscopy*, 121(1):1–19, 1987.

68. Ro, K. S., M. H. Johnson, R. M. Varma, R. A. Hashmonay, and P. Hunt. "Measurement of greenhouse gas emissions from agricultural sites using open-path optical remote sensing method". *Journal of Environmental Science and Health Part A*, 44(10):1011–1018, 2009.

69. Ro, Kyoung S., Melvin H. Johnson, Ravi M. Varma, Ram A. Hashmonay, and Patrick Hunt. "Measurement of greenhouse gas emissions from agricultural sites using open-path optical remote sensing method". *Journal of Environmental Science and Health, Part A*, 44(10):1011–1018, 08/03; 2012/05 2009.

70. Roth, B. D. "LADAR Performance Simulations with a High Spectral Resolution Atmospheric Transmittance and Radiance Model-LEEDR". 2012.

71. Roth, Benjamin D. and Steven T. Fiorino. "LADAR performance simulations with a high spectral resolution atmospheric transmittance and radiance model: LEEDR". 83790O–83790O, May 1 2012.

72. Rothman, L. S., I. E. Gordon, A. Barbe, D. Chris Benner, P. F. Bernath, M. Birk, V. Boudon, L. R. Brown, A. Campargue, J. P Champion, K. Chance, L. H. Coudert, V. Dana, V. M. Devi, S. Fally, J. M Flaud, R. R. Gamache, A. Goldman, D. Jacquemart, I. Kleiner, N. Lacome, W. J. Lafferty, J. Y Mandin, S. T. Massie, S. N. Mikhailenko, C. E. Miller, N. Moazzen-Ahmadi, O. V. Naumenko, A. V. Nikitin, J. Orphal, V. I. Perevalov, A. Perrin, A. Predoi-Cross, C. P. Rinsland, M. Rotger, M. imekov, M. A. H. Smith, K. Sung, S. A. Tashkun, J. Tennyson, R. A. Toth, A. C. Vandaele, and J. Vander Auwera. "The HITRAN 2008 molecular spectroscopic database". *Journal of Quantitative Spectroscopy and Radiative Transfer*, 110(910):533–572, 0 2009.

73. Rothman, L. S., I.E. Gordon, A. Barbe, D. C. Benner, P.F. Bernath, M. Birk, V. Boudon, L.R. Brown, A. Campargue, and J. P. Champion. "The HITRAN 2008 molecular spectroscopic database". *Journal of Quantitative Spectroscopy and Radiative Transfer*, 110(9-10):533–572, 2009.

74. Rothman, L. S., IE Gordon, A. Barbe, D. C. Benner, PF Bernath, M. Birk, V. Boudon, LR Brown, A. Campargue, and J. P. Champion. "The HITRAN 2008 molecular spectroscopic database". *Journal of Quantitative Spectroscopy and Radiative Transfer*, 110(9-10):533–572, 2009.

75. Somesfalean, G., J. Alnis, U. Gustafsson, H. Edner, and S. Svanberg. "Long-path monitoring of NO2 with a 635 nm diode laser using frequency-modulation spectroscopy". *Applied Optics*, 44(24):5148–5151, 2005.

76. Sonnenfroh, D.M., W.J. Kessler, J.C. Magill, B.L. Upschulte, M.G. Allen, and J.D.W. Barrick. "In-situ sensing of tropospheric water vapor using an airborne near-IR diode laser hygrometer". *Applied Physics B: Lasers and Optics*, 67(3):275–282, 1998.

77. Squires, M. F., B. A. Bietler, S. T. Fiorino, D. L. Parks, F. W. Youkhana, and H. D. Smith. "A method for creating regional and worldwide datasets of extreme and average values". *Institute of Environmental Sciences Proceedings 41st Annual Meeting*, 1995.

78. Steck, D. A. "Rubidium 87 D line data". *Los Alamos National Laboratory*, 2001.

79. Steck, D. A. "Cesium D line data". *Los Alamos National Laboratory*, 2003. URL `http://george.ph.utexas.edu/~dsteck/alkalidata/cesiumnumbers.pdf`.

80. Sulham, C. V., G. P. Perram, M. P. Wilkinson, and D. A. Hostutler. "A pulsed, optically-pumped rubidium laser at high pump intensity". *Optics Communications*, 283(21):4328–4332, 2010.

81. Thoma, E. D., R. C. Shores, E. L. Thompson, D. B. Harris, S. A. Thorneloe, R. M. Varma, R. A. Hashmonay, M. T. Modrak, D. F. Natschke, and H. A. Gamble. "Open-path tunable diode laser absorption spectroscopy for acquisition of fugitive emission flux data". *Journal of the Air and Waste Management Association*, 55(5):658–668, 2005.

82. Tiecke, TG. "Properties of Potassium". *University of Amsterdam, The Netherlands, Thesis*, 2010.

83. Tu, Xinhua, Fengzhong Dong, Feng Qi, Yujun Zhang, Wenqing Liu, and Jianguo Liu. "On-road remote sensing of CO and CO_2 of motor vehicle exhaust emissions in Beijing using a TDLAS system". volume 5832, 350–358. SPIE, May 12, 2005 2005.

84. Wang, Tiedong, Wenqing Liu, Yujun Zhang, Jianguo Liu, Fengzhong Dong, Min Wang, Xiaomei Wang, and Min Xu. "Remote sensing CO, CO_2 in vehicle emissions based on TDLAS". volume 6344, 634425. SPIE, June 9, 2006 2006.

85. Weibring, P., D. Richter, A. Fried, JG Walega, and C. Dyroff. "Ultra-high-precision mid-IR spectrometer II: system description and spectroscopic performance". *Applied Physics B: Lasers and Optics*, 85(2):207–218, 2006.

86. Werle, P. "A review of recent advances in semiconductor laser based gas monitors". *Spectrochimica Acta Part A: Molecular and Biomolecular Spectroscopy*, 54(2):197–236, 1998.

87. Werle, P.W., P. Mazzinghi, F. DAmato, M. De Rosa, K. Maurer, and F. Slemr. "Signal processing and calibration procedures for in situ diode-laser absorption spectroscopy". *Spectrochimica Acta Part A: Molecular and Biomolecular Spectroscopy*, 60(8):1685–1705, 2004.

88. Wert, B.P., A. Fried, B. Henry, and S. Cartier. "Evaluation of inlets used for the airborne measurement of formaldehyde". *J.Geophys.Res*, 107(4163):10.1029, 2002.

89. Wert, B.P., M. Trainer, A. Fried, TB Ryerson, B. Henry, W. Potter, W.M. Angevine, E. Atlas, S.G. Donnelly, and F.C. Fehsenfeld. "Signatures of terminal alkene oxidation in airborne formaldehyde measurements during TexAQS 2000". *J.Geophys.Res*, 108(D3):4104, 2003.

90. Wienhold, F.G., H. Fischer, P. Hoor, V. Wagner, R. Knigstedt, G.W. Harris, J. Anders, R. Grisar, M. Knothe, and W.J. Riedel. "TRISTARa tracer in situ TDLAS for atmospheric research". *Applied Physics B: Lasers and Optics*, 67(4):411–417, 1998.

91. Williams, D. *Methods of experimental physics*, volume 13. Academic Pr, 1976.

92. Wunderle, K., S. Wagner, I. Pasti, R. Pieruschka, U. Rascher, U. Schurr, and V. Ebert. "Distributed feedback diode laser spectrometer at 2.7 μmfor sensitive, spatially resolved H_2O vapor detection". *Applied Optics*, 48(4):B172–B182, 2009.

93. Zeller, W., L. Naehle, P. Fuchs, F. Gerschuetz, L. Hildebrandt, and J. Koeth. "DFB Lasers Between 760 nm and 16 μmfor Sensing Applications". *Sensors*, 10(4):2492–2510, 2010.

94. Zhdanov, B. and RJ Knize. "Diode-pumped 10 W continuous wave cesium laser". *Optics Letters*, 32(15):2167–2169, 2007.

95. Zhdanov, B., C. Maes, T. Ehrenreich, A. Havko, N. Koval, T. Meeker, B. Worker, B. Flusche, and RJ Knize. "Optically pumped potassium laser". *Optics Communications*, 270(2):353–355, 2007.

96. Zhdanov, BV, T. Ehrenreich, and RJ Knize. "Highly efficient optically pumped cesium vapor laser". *Optics Communications*, 260(2):696–698, 2006.

97. Zhdanov, B.V. and R.J. Knize. "Advanced diode-pumped alkali lasers". *Proceedings of SPIE*, volume 7022, 70220J. 2007.

98. Zhdanov, B.V., F. Kontur, S. Phipps, F. Hallada, P. Elsbernd, W. Miller, A. Peay, and R.J. Knize. "Tunable single frequency cesium laser". *Optics Communications*, 280(1):161–164, 2007.

99. Zhdanov, B.V., J. Sell, and R.J. Knize. "Multiple laser diode array pumped Cs laser with 48W output power". *Electronics Letters*, 44(9):582–583, 2008.

100. Zhdanov, B.V., M.K. Shaffer, and R.J. Knize. "Cs laser with unstable cavity transversely pumped by multiple diode lasers". *Optics Express*, 17(17):14767–14770, 2009.

101. Zhdanov, B.V., M.K. Shaffer, and R.J. Knize. "Cs laser with unstable cavity transversely pumped by multiple diode lasers". *Optics Express*, 17(17):14767–14770, 2009.

102. Zhdanov, B.V., M.K. Shaffer, J. Sell, and R.J. Knize. "Cesium vapor laser with transverse pumping by multiple laser diode arrays". *Optics Communications*, 281(23):5862–5863, 2008.

103. Zhdanov, B.V., A. Stooke, G. Boyadjian, A. Voci, and R.J. Knize. "Laser diode array pumped continuous wave Rubidium vapor laser". *Optics express*, 16(2):748–751, 2008.

104. Zninari, V., B. Parvitte, L. Joly, T. Le Barbu, N. Amarouche, and G. Durry. "Laboratory spectroscopic calibration of infrared tunable laser spectrometers for the in situ sensing of the Earth and Martian atmospheres". *Applied Physics B: Lasers and Optics*, 85(2):265–272, 2006.

105. Zweiback, J., G. Hager, and W. F. Krupke. "High efficiency hydrocarbon-free resonance transition potassium laser". *Optics Communications*, 282(9):1871–1873, 2009.

106. Zweiback, J. and W. F. Krupke. "28W average power hydrocarbon-free rubidium diode pumped alkali laser". *Optics Express*, 18(2):1444–1449, 2010.

107. Zweiback, J., W.F. Krupke, and A. Komashko. "Diode pumped alkali vapor lasers for high power applications". *Proceedings of the SPIE (San Jose, CA, USA*, volume 6874, 68740G–68740G. 2008.

Vita

Christopher A. Rice graduated from Southeastern High School in South Charleston, Ohio. He completed his undergraduate studies at Cedarville University in Cedarville, Ohio, earning a Bachelor of Science degree in Electrical Engineering in May of 2004. He was awarded full tuition under a DAGSI scholarship to the Air Force of Technology (AFIT) in Wright Patterson AFB, Ohio where he was accepted to the Graduate School of Engineering and Management for a Masters degree in electrical engineering in 2006. In August of 2006 he was awarded a DAGSI fellowship to pursue a PhD at AFIT in Optical Science and Engineering. Upon graduation he will pursue a post-doctoral position at AFIT.

REPORT DOCUMENTATION PAGE

Form Approved
OMB No. 0704–0188

1. REPORT DATE *(DD–MM–YYYY)*	2. REPORT TYPE	3. DATES COVERED *(From — To)*
15–09–2012	Doctoral Dissertation	Sep 2006 — Sep 2012

4. TITLE AND SUBTITLE

Investigation of diode pumped alkali laser atmospheric transmission using tunable diode laser absorption spectroscopy

5a. CONTRACT NUMBER

5b. GRANT NUMBER

5c. PROGRAM ELEMENT NUMBER

6. AUTHOR(S)

Christopher A. Rice, Civilian, USAF

5d. PROJECT NUMBER

5e. TASK NUMBER

5f. WORK UNIT NUMBER

7. PERFORMING ORGANIZATION NAME(S) AND ADDRESS(ES)

Air Force Institute of Technology
Graduate School of Engineering and Management (AFIT/EN)
2950 Hobson Way
WPAFB OH 45433-7765

8. PERFORMING ORGANIZATION REPORT NUMBER

AFIT-ENP-DS-12-D-07

9. SPONSORING / MONITORING AGENCY NAME(S) AND ADDRESS(ES)

Dr. Brian Hankla
High Energy Laser Joint Technology Office
801 University Blvd. SE, Suite 209
Albuquerque, NM 87106

10. SPONSOR/MONITOR'S ACRONYM(S)

HEL-JTO

11. SPONSOR/MONITOR'S REPORT NUMBER(S)

12. DISTRIBUTION / AVAILABILITY STATEMENT

APPROVED FOR PUBLIC RELEASE; DISTRIBUTION UNLIMITED.

13. SUPPLEMENTARY NOTES

14. ABSTRACT

A field deployable ruggedized tunable diode laser absorption spectroscopy (TDLAS) device fiber coupled to a pair of 12.5" Ritchey-Chrétien telescopes was used to study atmospheric propagation for open path lengths of 100 to 1,000 meters to estimate atmospheric transmission at key High Energy Laser (HEL) wavelengths. The potassium (K) version of the Diode Pumped Alkali Laser (DPAL) operates in between two of the sharp oxygen rotational features in the ^PP and the ^PQ branches. The device can be used to observe rotational temperature, concentrations, and atmospheric pressure. Molecular oxygen absorption lines near the potassium, and water vapor absorption lines near the rubidium and cesium DPALs at wavelengths near 770 nm, 795 nm, and 895 nm, respectively, were investigated using the Line-by-Line Radiative Transfer Model (LBLRTM) with the High Energy Laser End-to-End Simulation (HELEEOS). A tunable diode laser absorption spectroscopy (TDLAS) device was used to anchor simulations to actual outdoor atmospheric open-path collections. The implications of different laser gain cell configurations in DPAL systems are discussed, including spectral lineshape and atmospheric transmittance and are compared to existing high power laser systems.

15. SUBJECT TERMS

Diode-Pumped Alkali Laser (DPAL), TDLAS, Open-Path, Tunable Diode Laser, DPAL, Potassium, Molecular Oxygen, Laser Spectroscopy, Molecular Spectra, Optical absorption in atmosphere, Absorption Spectroscopy Instrumentation, Atmospheric transmittance, Laser beam transmission, Atomic gas lasers, Molecular spectroscopy.

16. SECURITY CLASSIFICATION OF:			17. LIMITATION OF ABSTRACT	18. NUMBER OF PAGES	19a. NAME OF RESPONSIBLE PERSON
a. REPORT	b. ABSTRACT	c. THIS PAGE			Dr. Glen P. Perram
U	U	U	UU	179	**19b. TELEPHONE NUMBER** *(include area code)* (937) 255-3636, x4504; glen.perram@afit.edu

Standard Form 298 (Rev. 8–98)
Prescribed by ANSI Std. Z39.18